Thesis for Degree of Doctor of Philosophy

Nanoelectromechanical Systems from Carbon Nanotubes and Graphene

Niklas Lindahl

UNIVERSITY OF GOTHENBURG

Department of physics
University of Gothenburg
Göteborg 2012

ISBN 978-91-628-8411-6

Typeset using LaTeX
Department of physics
University of Gothenburg
SE-412 96 Göteborg, Sweden
Phone: +46 (0)31 786 0000

Printed by Kompendiet
Göteborg, Sweden 2011

Nanoelectromechanical Systems from Carbon Nanotubes and Graphene

Niklas Lindahl

Department of physics
University of Gothenburg
SE-412 96 Göteborg, Sweden

Abstract

Carbon nanotubes and graphene have many interesting properties. To exploit the properties in applications their synthesis and incorporation in devices has to be understood and controlled. This thesis is based on experimental studies on synthesis of carbon nanotubes and fabrication of nanoelectromechanical systems from carbon nanotubes and graphene.

Vertically aligned nanotube arrays with heights over 800 μm have been grown using acetylene with iron as catalyst on alumina support using thermal chemical vapor deposition. By varying the partial pressure of acetylene it was found that the addition-rate of carbon was proportional to the coverage of acetylene molecules on the catalyst nanoparticle.

In certain conditions the macroscopic pattern of the catalyst areas influenced the microscopic properties of the carbon nanotubes. It was shown that the initial carbon-precursor flow conditions could determine the number of walls produced. The amount of carbon incorporated into nanotubes was constant but regions that experienced less carbon precursor gas flow due e.g. to depletion, produced longer but fewer-walled nanotubes.

Arrays of vertically aligned nanotubes were shown to deflect as a single unit under electrostatic actuation, making possible the fabrication of varactors. Measurements of deflection were used to determine an effective Young's modulus of 6 ± 4 MPa. The capacitance of such a device could be reproducibly changed by more than 20 %.

Devices based on the nanoelectromechanical properties of few-layer graphene were fabricated and characterized. Electrostatic actuation of buckled beams and membranes led to a "snap-through" switching at a critical applied voltage. By characterizing this behavior for different sizes and geometries of membranes, it was possible to extract the bending rigidity of bilayered graphene, yielding a value of 35^{+20}_{-15} eV.

CNTFETs with suspended graphene gates were fabricated. It was shown that a moveable graphene gate could control the conductance of the carbon nanotube and improve the switching characteristics. Inverse sub-threshold slope down to 53 mV per decade were measured at 100 K. The experimental data were compared with theoretical simulations and it was inferred that the subthreshold slope could be improved beyond the thermal limit by improving the design of the device.

Keywords: Carbon nanotubes, Synthesis, Chemical vapor deposition, Graphene, Bending Rigidity, Nanoelectromechanical systems

Research publications

This thesis is partly based on the work contained in the following papers, printed as appendices and referred to by capital roman numerals in the text:

I N. Olofsson and E.E.B. Campbell.
In situ studies of growth kinetics of vertically aligned carbon nanotube arrays
To be submitted to Carbon

II G.-H. Jeong, N. Olofsson, L.K.L. Falk and E.E.B. Campbell.
Effect of catalyst pattern geometry on the growth of vertically aligned carbon nanotube arrays
Carbon, ***47*** *696, 2009*

III N. Olofsson, J. Ek Weis, A. Eriksson, T. Idda and E. E. B. Campbell.
Determination of the effective Young's modulus of vertically aligned carbon nanotube arrays: a simple nanotube-based varactor
Nanotechnology, ***20*** *385710, 2009*

IV N. Lindahl, D. Midtvedt, J. Svensson, N. Lindvall, O. Nerushev, A. Isacsson and E. E. B. Campbell.
Determination of the Bending Rigidity of Graphene via Electrostatic Actuation of Buckled Membranes
Submitted to Nature Materials

V J. Svensson, N. Lindahl, H. Yun, M. Seo, D. Midtvedt, Y. Tarakanov, N. Lindvall, O. Nerushev, J. Kinaret, S. W. Lee and E. E. B. Campbell.
Carbon Nanotube Field Effect Transistors with Suspended Graphene Gates
Nano Letters, ***11*** *3569, 2011*

The contribution by the author, N. Lindahl (Olofsson before 2011), to these papers was the following:

I I was responsible for substrate fabrication, synthesis of carbon nanotubes and measurements used in the publication. I analyzed the data and wrote the first draft of the manuscript, then worked on it with EEBC.

II I was responsible for substrate fabrication. I took part in the synthesis of carbon nanotubes and made characterization by transmission electron microscopy. I performed the analysis of some of the data. GHJ wrote the first draft of the manuscript, and then we worked on it together with EEBC.

III I was responsible for substrate fabrication, synthesis of carbon nanotubes and measurements. JEW was responsible for electrical characterization and modelling. I wrote the first draft and then worked on it together with EEBC.

IV I was responsible for device fabrication and measurements used in the publication. DM was responsible for modelling and simulations. I took part in analysis of the data. I wrote the first draft of the manuscript, and then worked on it together with DM, AI and EEBC.

V I was responsible for device fabrication. JS was responsible for electrical characterization and studies in AFM. I took part in measurements and analysis of the data. JS wrote the first draft of the manuscript and then worked on it together with me, YT and EEBC.

Papers not included in the thesis:

A S. Dittmer, N. Olofsson, J. Ek Weis, O. A. Nerushev, A. V. Gromov and E. E. B. Campbell.
In situ raman studies of single-walled carbon nanotubes grown by local catalyst heating
*Chemical Physics Letters,**457**(1-3)206, 2008.*

B J. Ek Weis, A. Eriksson, T. Idda, N. Olofsson and E. E. B. Campbell.
Radio-frequency characterization of varactors based on carbon nanotube arrays
*Journal of Nanoengineering and Nanosystems,**222**(3)111, 2008.*

C T. Wang, K. Jeppson, N. Olofsson, E. E. B. Campbell and J. Liu.
Through silicon vias filled with planarized carbon nanotube bundles
*Nanotechnology,**20** 485203, 2009.*

D S. Bengtsson, P. Enoksson, F. Ghavanini, K. Engström, P. Lundgren, E. E. B. Campbell, J. Ek Weis, N. Olofsson and A. Eriksson.
Carbon-based nanoelectromechanical devices
*International Journal of High Speed Electronics and Systems,**20**(1)195, 2011.*

E Y. Fu, B. Carlberg, N. Lindahl, N. Lindvall, J. Bielecki, A. Matic, Y. Song, Z. Hu, Z. Lai, L. Ye, J. Sun, Y. Zhang and J. Liu.
Templated growth of covalently bonded three-dimensional carbon nanotube networks originated from graphene
Submitted to Advanced Materials

Preface

Inevitably generations come and go. The day we leave it is perhaps not our own experiences or knowledge that matter. Instead our accomplishment is the knowledge we have transferred to coming generations.

Knowledge is preferably transferred spending time with each other, learning which details are of importance and which are not. Unfortunately that is not always possible. Then writing a Ph.D. thesis might be the best option.

Graphene is a sheet of carbon atoms only one atomic layer in thickness. A carbon nanotube can be thought of as a tube rolled up from graphene. Advancements in nanoscience have enabled the discovery, followed by studies of properties and development of applications, of those new materials during the last two decades.

This thesis is based on my experimental work on carbon nanotubes and graphene at Gothenburg University. It began in 2006, when carbon nanotubes were expected to provide solutions to most problems in the world. Now, five years later, graphene bears the same expectations. Even though I don't expect a revolution based on nano-carbon, there is a great chance that products based on carbon nanotubes and graphene eventually will reach customers. If my work to some extent contributes, I will be very pleased.

My work has involved synthesis of carbon nanotubes and fabrication and characterization of nanoelectromechanical systems. I have learnt to expect that experiments do not work out as expected. Most of the time my work has resulted in failures in fabrication. When not, most of the time my work has resulted in failures in measurements. When not, most of the time my work has resulted in data not worth mentioning in this thesis or elsewhere.

But occasionally successful experiments work out as planned, resulting in knowledge possible to publish and spread all over the world. Even more occasionally successful experiments do not work out as planned, instead leading you in new directions towards unexpected discoveries. The chance to encounter the latter is a large part of the charm of being experimentalist.

The aim of this thesis is to transfer the selected parts of the knowledge I have obtained in this scientific field. The main results are described in the second and most important part, the appended scientific papers referred to as Paper I to V. The first part of the thesis is meant to introduce the subjects described in the papers.

The thesis is intended for readers interested in experimental nanophysics in general and nanoelectromechanical systems based on carbon nanotubes or graphene in particular. The level of details of the text is intended to be suitable for master students in physics, chemistry or electronics considering a Ph.D. The main concepts hopefully are understandable for an interested reader.

Chapters 1 to 3 are intended to provide the reader with an introduction to help understand the concepts presented in the scientific papers. All the subjects presented are not discussed in full detail, but the interested reader is encouraged to follow the references to other scientific papers. Also references to recommended review-articles are found at the beginning of each chapter.

In Chapter 1 the reader is introduced to the structure and the properties of carbon nanotubes and graphene. Emphasis is put on the electrical and mechanical properties, which enable the devices proposed in later chapters. Fabrication and characterization of devices from carbon nanotubes and graphene is described in Chapter 2. In Chapter 3 two devices, benefitting from the special properties of carbon nanotubes and graphene, are described. The two devices form the basis for Papers IV and V.

Chapters 4 to 7 selected results from the scientific papers are presented. An introduction and complementary results and discussions are also given. Chapter 4 describes the synthesis of carbon nanotubes, studied in Paper I and II. Based on Paper III, Chapter 5 presents electromechanical varactors based on carbon nanotubes and their use in determining mechanical properties.

Chapter 6 treats fabrication of buckled beams of graphene and how their actuation was used to determine the bending rigidity, also found in Paper IV. Based on Paper V, Chapter 7 presents nanoelectromechanical devices incorporating both carbon nanotubes and graphene.

If the reader find parts of this thesis to be interesting and rewarding its main objective is fulfilled. Hopefully a few readers can apply the methods or results described. In the best case the thesis will inspire the reader to start working on the subjects presented. I hope for the best.

Niklas Lindahl

Contents

Chapter 1

Material properties

The process of finding and exploiting new materials has always been a keystone in the development of humanity. From the large step into the stone-age, through the start of using metals and on until today's age of silicon and plastics, driven by need and curiosity people have discovered new materials and investigated their properties. Discoveries of new forms of carbon have attracted the interest of many material scientists.

In this chapter the structure and properties of those, graphene and carbon nanotubes, will be described. Complementary reviews on those subjects by Geim [1] and Avouris et al. [2] are recommended.

1.1 Carbon allotropes

Carbon is the building material of life and the basis of all organic chemistry. Thanks to the flexibility of its bonds carbon can exist in many forms with different properties. In carbon allotropes, crystalline structures made of only carbon atoms, depending on the arrangement of the bonds carbon can form diamond and graphite. Diamond is so hard due to the strong bonding between atoms. In graphite, where strong bonds are found along the planes but weaker bonds between planes, it is possible to peel off planes from each other.

In 1985 another structure made of carbon was discovered, namely the spherical fullerene, consisting of carbon atoms arranged in a lattice similar to the seams on a nanometer-sized soccer-ball [3], as seen in figure 1.1a. Nineteen years later it was found to be possible to peel off a single sheet of graphite, called graphene, consisting of carbon atoms in a two-dimensional hexagonal honeycomb lattice [4]. The one-dimensional carbon nanotube is a structural intermediate, which could be thought of as a rolled up two-dimensional graphene sheet with half a zero-dimensional fullerene at its ends as seen in figure 1.1b. They were also discovered at an intermediate point of time in 1991 [5].

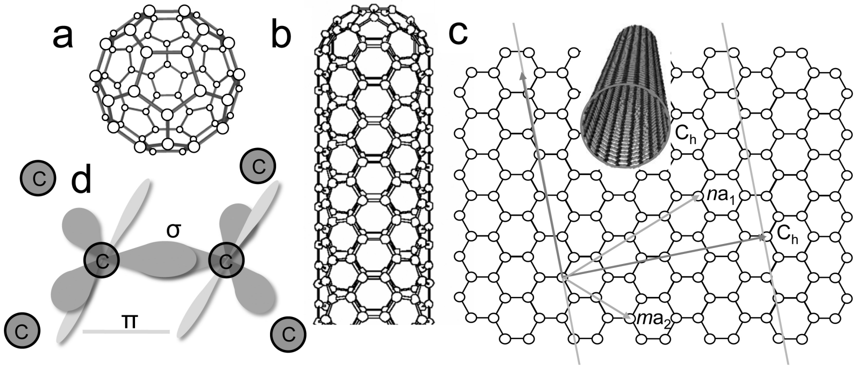

Figure 1.1: (a) Schematic structure of a fullerene. (b) Schematic structure of a carbon nanotube. (c) A carbon nanotube can be thought of being rolled up from a sheet of graphene. (d) Schematic image of the sp^2-hybridization. Each carbon atom has 3 sp^2-orbitals and 1 p_z-orbital. Overlapping sp^2-orbitals form σ bonds and p_z-orbitals form π bonds.

Graphene can be considered to be made of benzene rings joined together and stripped of their hydrogen atoms. Isolated carbon atoms have four valence electrons. In graphene three atomic orbitals are hybridized into a trigonal planar structure, forming the sp^2-hybridization with covalent σ bonds between the carbon atoms, see figure 1.1d. Those strong bonds are responsible for the robustness of graphene. The remaining fourth valence electrons form covalent π bonds with neighboring carbon atoms and those are responsible for the electronic properties [6].

A carbon nanotube (CNT) could be thought of as being rolled up either from a single sheet of graphene making the wall of the tube consist of a single layer of carbon atoms, thus called single-walled nanotube (SWNT), or many sheets of graphene, called multi-walled nanotube (MWNT). The latter can be compared to a Russian doll where the individual dolls of smaller and smaller sizes are SWNTs, which are stacked into each other to form a MWNT. In reality CNTs are not made by rolling up graphene, however the opposite process of unzipping CNTs into graphene has been realized experimentally [7].

Thinking of a SWNT to be rolled up from a graphene sheet, the tube can be specified by the chiral indices (n, m) defining the chiral vector $C_\mathrm{h} = n \cdot a_1 + m \cdot a_2$, where a_1 and a_2 are the unit vectors of the graphene lattice. The chiral vector then describes the circumference of the SWNT, as seen in figure 1.1c. From the chiral indices the diameter and chiral angle of a SWNT can be determined.

Experimentally, diameters of SWNT are found to be less than a few nm and in some cases as small as 4 Å for freestanding SWNT [8] and 3 Å for CNT inside MWNT [9]. Carbon nanotubes can have very large aspect ratios.

For SWNTs of 1 nm diameter, lengths close to 20 cm have been reported [10]. Since graphene is a single layer of atoms, the definition of thickness is ambiguous. A common value to use is the inter-plane distance of 3.35 Å in graphite [11]. Single crystals of mono-layered graphene with dimensions up to 1 mm^2 have been obtained [12].

1.2 Mechanical properties

It has been discussed that two-dimensional crystals can not exist due to thermally induced atomic vibrations resulting in melting at any finite temperature [13]. However the discovery of graphene, a single layer of atoms truly being a two-dimensional crystal, has shown that stability can be obtained for flat graphene by support from the substrate [14] and for suspended graphene by forming ripples in all three dimensions [15].

The strength of the sp^2-bonds between carbon atoms makes graphene very stable. It has been measured that, assuming a thickness of the inter-plane distance, graphene has an effective in-plane Young's modulus of 1.0 TPa, a tensile strength of 130 GPa and that elastic stretching up to 20 % is possible [16]. The value of the tensile strength for MWNTs is 63 GPa [17], the lower value being due to more defects. In comparison the tensile strength of standard steel is less than 1 GPa.

This in combination with their low density, which is six times lower than steel, make graphene and CNTs very promising materials for light-weight and high-strength applications, used e.g. in composites for sport materials, space-elevators and nanoelectromechanical systems. The latter are described in Chapter 3 and examples are found in Paper III and IV.

1.3 Electronic properties

Where the conduction- and the valence band in graphene meet, the energy dispersion is linear for low energies [6]. This gives the conical shape of the energy levels depicted in figure 1.2. Thus the density of states approaches zero at the Fermi point, making graphene a zero bandgap semiconductor. The linear dispersion also implies that electrons propagate with zero effective mass, resulting in quasi-particles described by a Dirac-like equation. In combination with samples of high quality where electrons can travel relatively long distances without scattering this leads to robust quantum effects surviving even at room temperature, hence turning graphene into a playground for fundamental physics [12].

It should be noted that the described electronic properties of graphene are valid for monolayered graphene. For a stack of two layers of graphene on top of each other, bilayered graphene, there is a small overlap between conduction- and valence band. For 3 layers the overlap increases drastically and for 10 layers or more it is less than 10 % different from bulk graphite [18]. Hence mono-, bi- and few-layered graphene should be distinguished as different types of graphene. In this thesis graphene is mono-layered unless stated differently.

The unusual electronic structure of graphene is the origin of the remarkable electrical properties of carbon nanotubes [2]. When folded into a nanotube, the imposed periodic boundary conditions quantize the allowed values of electron momenta around the circumference, k_y. Thus only a few slices of the conical energy levels become available, see figure 1.2. Which slices that are allowed depends on tube diameter and chirality. If the allowed slices include the Fermi point the CNT will have metallic properties. Otherwise it will be semiconducting, with a band-gap that is inversely proportional to diameter [19]. Thus the chiral indices of the tube determine its electronic properties.

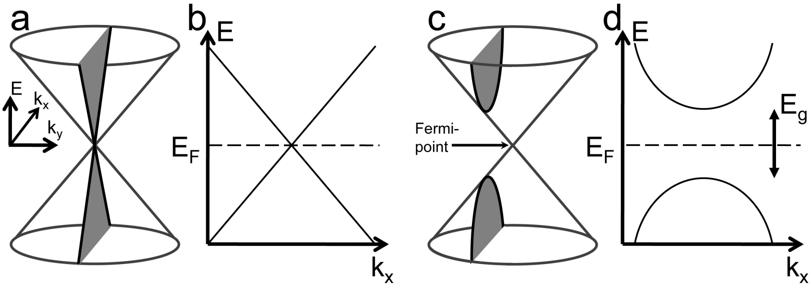

Figure 1.2: (a) Schematic band-structure of graphene, with a slice of allowed momenta, k_y, in metallic SWNTs. (b) Schematic band-diagram of a metallic SWNT. (c) Schematic band-structure of graphene, with a slice of allowed momenta, k_y, in semiconducting SWNTs. (d) Schematic band-diagram of a semi-conducting SWNT.

As a zero-gap semiconductor, graphene behaves similar to a metal at finite temperatures. A band gap is opened when narrow graphene nanoribbons are formed due to quantum confinement, similar to CNTs [20]. Also for graphene the energy spacing is inversely proportional to the width. However, the band gap is doubled in a CNT, compared to a graphene nanoribbon of the same width as the CNT circumference, due to different boundary conditions [2].

The excellent electrical properties in combination with the small physical dimensions makes graphene and carbon nanotubes very promising materials for electronic applications, as discussed more in Chapter 3 and used in Paper V. Improvements of microprocessors over the last decades have mainly been due to miniaturization of its most important component, the transistor. For various reasons this development cannot continue forever using silicon as building material. Instead graphene nanoribbons [1] and carbon nanotubes [2] have been envisioned as being the building-block of future transistors. In order to make that possible, better control of their synthesis and device fabrication has to be achieved.

Chapter 2

Experimental methods

New materials enable new technology. But they also require new technology. Development of methods for production and characterization often goes hand in hand with development in material science. After synthesis of a material, characterization of it has usually been desired. The gained knowledge has led to improved methods both for fabrication and investigation of materials.

In this chapter synthesis and characterization of graphene and carbon nanotubes will be introduced. Also methods for fabrication of devices thereof will be described. Synthesis of carbon nanotubes is described further in Chapter 4 and in a review by Nessim [21]. The review of characterization of CNTs by Belin and Epron [22] and the introduction to micro- and nanofabrication by Ziaie et al. [23] provide broader perspectives on the subjects.

2.1 Microfabrication

Advances in techniques for making small structures have been driven by the demand for faster, cheaper and more efficient computers. This has led to the development of microelectronics with increasing density of transistors in microprocessors and memory chips.

Fabrication of the small structures in microelectronics is done by removing or adding material on a surface, usually silicon. The building blocks, for example transistors and resistors, are sculptured down from existing bulk material, which could be a metal; semiconductor or insulator. The building blocks are then assembled on top of each other into the final structure, hence these methods are called top-down fabrication.

Examples of a typical scheme of top-down processes, used to fabricate suspended graphene beams e.g. in Paper IV, are shown in figure 2.1. Starting from an oxidized silicon substrate, graphene is deposited on the surface, as seen in figure 2.1a. Resist is patterned on top by electron-beam lithography

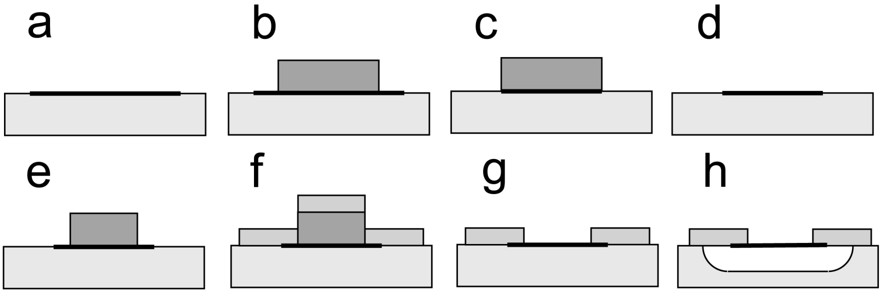

Figure 2.1: (a-h) Schematic cross-sections during the fabrication-steps of suspended beams from graphene. The schematic structures are seen from the side through a cross-section during the steps of processing. (a) Deposition of graphene. (b) Resist patterning. (c) Dry etching of graphene. (d) Removal of resist. (e) Patterning of new resist. (f) Metal deposition. (g) Lift-off. (h) Wet etching of substrate underlying graphene.

(EBL). In EBL parts of the resist are exposed by a focused electron-beam, thus modifying the properties of the exposed areas. Typically only exposed parts are selectively removed when put into a developer, figure 2.1b.

Patterning of resist can also be done by photolithography, where UV-light is used instead of the electron beam. Electron-beam lithography gives better resolution and the ability to tailor-make the pattern of exposure for each sample, making it suitable for patterning on carbon nanotubes and graphene where the desired pattern typically differs from sample to sample. Photolithography on the other hand enables mass-fabrication of patterns, making it the choice for lithography in the semiconductor industry.

The pattern of the resist is transferred to graphene by dry etching. During dry etching ions in a plasma are accelerated towards the substrate and remove the surface atoms either by physical sputtering, chemical reactions or both. Masks can be used to protect certain areas, such as in figure 2.1c where only parts not covered by the patterned resist are removed. After removal of the resist, patterned graphene beams remain on the substrate, figure 2.1d.

A new layer of resist is patterned, using EBL, in the shape of electrodes contacting the graphene beams in figure 2.1e. Metal is deposited by electron-beam evaporation. A metal-source is heated by an electron-beam until it evaporates. Kept in vacuum the evaporated atoms travel in straight lines towards the sample, landing on top of the resist or on top of the substrate where resist is missing, figure 2.1f. Removal of the resist with metal on top leaves electrodes on the substrates, figure 2.1g.

Wet etching of the substrate underneath is the final step to obtain suspended graphene beams, figure 2.1h. The etchant reacts chemically with the material to be removed. Material that does not react with the etchant is not removed. Hence, wet etching can be used to remove hundreds of nanometer thickness of silica while keeping an atomic layer of graphene unaffected.

Fabrication of advanced devices built up step by step is achievable using top-down methods. However the lithographic resolution has limits and it becomes increasingly hard to carve out structures with smaller and smaller dimensions. To continue to increase the performance of computers, it will eventually be necessary to combine the existing methods with other methods capable of producing structures with atomic perfection, which has been done in Paper III, IV and V.

2.2 Synthesis of carbon nanotubes

In bottom-up fabrication the starting material is individual atoms or molecules, which are put together to build up larger structures. Under certain conditions atoms of the chosen material self-assemble into the preferred structure, usually a particle or wire. Using bottom-up methods, structures with dimensions down to less than a nanometer can be formed spontaneously by the atoms themselves.

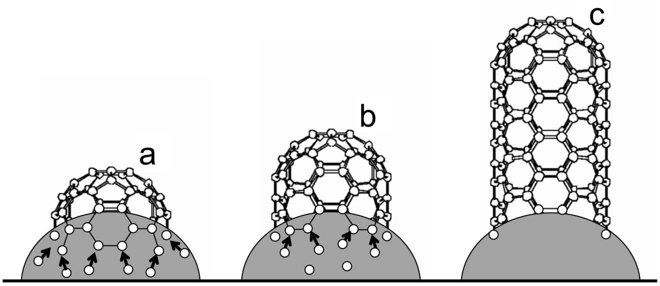

Figure 2.2: (a) Carbon atoms on a catalyst nanoparticle bond with each other into a cap. (b) Added carbon atoms bond to the edge of the cap. (c) Addition of carbon atoms to the edge increases the length of the carbon nanotube.

An example of bottom-up fabrication is growth of carbon nanotubes. Carbon atoms are added to a catalyst nanoparticle, where they start to bond with each other and form a half-sphere of atoms. As more atoms are added they are incorporated into the edge of the carbon nanotube, where they are guided by the existing atoms into their lattice position. The added atoms thus increase the length of the formed carbon nanotube, as seen in figure 2.2.

The small size and the excellent electronic properties of CNTs are features suggesting that they could be used as building blocks in future microchips. In order to make this possible, better control of their growth must be achieved, which was done in Paper I and II. In addition, the advantages of bottom-up methods must be combined with the advantages of top-down methods.

Control of carbon nanotube synthesis requires understanding of the processes involved. It has been seen that carbon nanotubes can be formed under a range of different conditions. The methods of arc discharge, laser ablation and chemical vapor deposition have been developed. The basic requirements to form SWNTs have been found to be an active catalyst, a source of carbon and sufficient energy.

In arc discharge synthesis a high-current power supply is used to produce an arc across an mm-sized gap between two graphite electrodes, as seen in figure 2.3a. Using an inert gas as reaction atmosphere MWNTs are formed on the cathode [5]. By adding metal catalyst to the anode, formation of SWNTs was possible [24]. The discovery of carbon nanotubes was made in material made by this method.

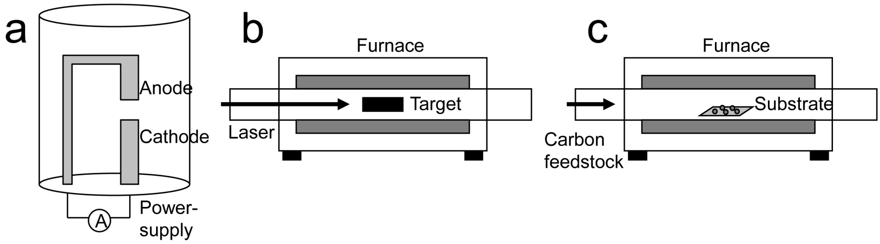

Figure 2.3: Schematic setup for synthesis of carbon nanotubes using arc-discharge (a), laser ablation (b) and chemical vapor deposition (c).

The first large-scale production of SWNTs was achieved using laser ablation synthesis [25]. A graphitic target with cobolt and nickel incorporated was placed in an inert atmosphere and heated to 1200 °C in a quartz-tube furnace, figure 2.3b. The target was vaporized using a high-power laser pulse, forming a plume of vaporized graphite and nanometer-sized metal particles. SWNTs were grown in the plume and collected when cooled.

In chemical vapor deposition (CVD) a catalyst nanoparticle, typically made of iron; cobolt or nickel, breaks down a gas containing carbon. The catalyst is heated to typically between 700 and 900 °C, figure 2.3c. The carbon feedstock, e.g. acetylene; ethylene or methane, is added to the reaction atmosphere and when its molecules are dissociated on the catalysts their carbon atoms go into growth of CNTs.

Decomposition of the carbon feedstock can be done either by thermal energy, used in thermal chemical vapor deposition (TCVD), or be assisted by plasma creating reactive species facilitating growth at low temperatures, used in plasma-enhanced chemical vapor deposition (PECVD). CVD-synthesis enables synthesis of CNTs from individual SWNTs to industrial-scale bulk production of MWNTs.

An advantage of CVD, compared to other methods for synthesis, is that CNTs can be grown directly on a substrate. This enables control of the position of CNTs by lithographically patterning areas with thin films of catalyst material, as in figure 2.4a. The use of standard microfabrication on the substrate both before and after synthesis of CNTs enables device fabrication on the same substrate where they are grown.

Chemical vapor deposition can also be used for synthesis of graphene. Similar to growth of nanotubes a carbon feedstock is used on a metallic film, but its thickness is different. For nanotubes it is important that the film is very thin, typically 1 nm, in order to form nanoparticles of the size needed for growth of nanotubes. For two-dimensional graphene instead a continuous metal film, e.g. Ni [26] or Cu [27], is used [26]. A drawback of graphene flakes grown with CVD on metal film, is that they have to be transferred to another substrate to enable electrical measurements.

An alternative method to obtain layers of graphene is to peel them from graphite. When pressed onto a substrate flakes of different thickness are exfoliated. The flakes with the desired number of layers can be selected for device fabrication and characterization. This method, known as the scotch-tape method, was used when isolated monolayers of graphene were discovered [4] and still gives the best quality of flakes.

Graphene flakes of high quality with sizes large enough for most scientific studies are produced this way. However, the position where graphene is exfoliated cannot be controlled, although transferring it onto pre-defined locations is possible afterwards [28]. Thus the scotch-tape method cannot be scaled up for mass production. Other methods for fabrication of graphene, in addition to CVD, are epitaxial growth on silicon carbide [29] and exfoliation by sonication of graphite in liquid [30].

2.3 Characterization

After fabrication, characterization of the obtained graphene or carbon nanotubes is often desired. The nanometer dimensions makes full characterization on an atomic level challenging. Still there are many possibilities and the method of choice depends on which property is to be studied.

Optical microscopy has proved to be an excellent tool for selection of graphene flakes after exfoliation on a substrate. Despite being only a single layer of atoms thick, when put on oxidized silicon of carefully chosen thickness, interference-like contrast makes graphene visible [31]. Hence finding flakes and determining their shape and location for further processing is possible with an optical microscope, facilitating the work in Paper IV and V.

Vertically aligned nanotube arrays, as shown in figure 2.4a, can be studied in an optical microscope to measure height and position, which was utilized in Paper III. Using scanning electron-microscopy (SEM) it is possible to observe smaller details in the sample, i.e. the individual CNTs in the array. Also individual SWNTs on a substrate are visible in SEM, as seen in figure 3.3a, so that their position and length can be determined with a resolution of a few nanometers.

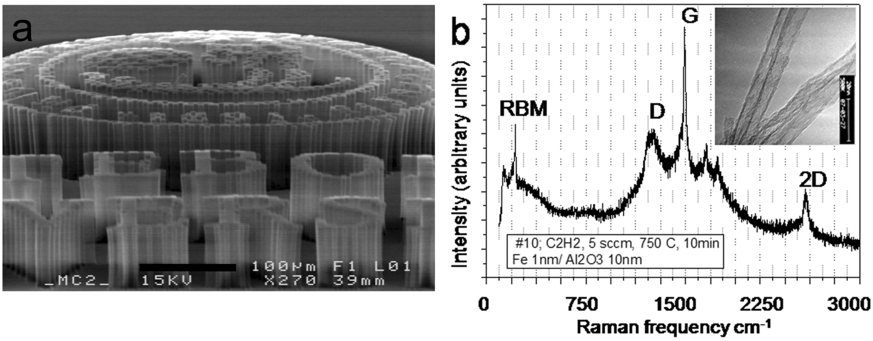

Figure 2.4: (a) SEM-image of vertically aligned nanotube arrays. Scale-bar is 100 μm. (b) Raman spectrum of CNTs. Inset shows a TEM-image of CNTs grown at similar conditions. Scale-bar is 20 nm.

Transmission electron-microscopy (TEM) can be used to image the atomic structure, such as defects and ripples in graphene [15] and diameter and number of walls in CNTs [5], as seen in the inset to figure 2.4b. Determination of the microstructure in TEM of the carbon nanotubes after synthesis was crucial for understanding the results in Paper I and II.

Since the carbon bonds are sensitive to electron irradiation, acceleration voltage and electron dose should be kept as low as possible to avoid defects created from knock-on effect [32]. By comparing images of CNTs obtained by TEM with simulations it has been possible to determine chiral indices of nanotubes with diameters down to 0.4 nm [33].

Imaging of the topography of a surface can be done using atomic force microscopy (AFM), which is a form of scanning probe microscopy (SPM), where a sharp tip attached on a cantilever is put in close proximity to the surface. By measuring the forces between the surface and the tip, the cantilever can image surface topography when scanned across the substrate. Vertical resolution of less than a nanometer can be obtained whereas lateral resolution is limited by the sharpness of the tip, typically on the order of 10 nanometers.

Imaging in AFM is time-consuming, due to the limits in speed of scanning, and mostly requires the structure to be imaged and located in an optical microscope or SEM first. However an AFM can be used not only to image but also to measure properties of the surface. Examples are the possibility to do force-deflection measurements to obtain the mechanical properties of the imaged structures [16].

Optical spectroscopy can be used as a complement to imaging of nanotubes. In resonant Raman spectroscopy an electron is excited, by absorbing a photon, from the valence band to the conduction band. The excited electron might lose energy to lattice vibrations and is then relaxed back to the valence band. The shift in energy, between absorbed and emitted photon, is measured and used to probe the vibrational modes.

A Raman-spectrum, seen in figure 2.4b, shows the intensity of photons for different shifts in energy. The intensity-peaks correspond to vibrations in the carbon structure. The G band is due to vibrations along the hexagonal carbon lattice and the the D band is due to presence of disorder [34]. Thus Raman spectroscopy can be used to determine quality by comparing the area of the D and G band.

Part of the spectrum obtained from a SWNT resonant with photons from the excitation laser contains a peak from the radial breathing mode (RBM), whose frequency depends on the diameter of the nanotube [35]. The 2D peak, the second order of the D peak, can be used to determine the number of layers [36] and to measure strain [37].

Chapter 3

Applications

New materials enable new applications. Development of applications has always been a driving force for material science and continues to be so when entering the age of carbon.

Graphene and carbon nanotubes can be envisioned in many applications [12] [38]. The high conductivity together with transparency enable transparent electrodes for touchscreens [39] and solar cells [40]. The conductivity together with large surface area could find use in electric batteries [41]. Applications in optoelectronics have also been proposed [42].

This thesis focuses on the exceptional electronic and mechanical properties of graphene and carbon nanotubes. In combination with their small dimensions and low mass density this makes them interesting materials for fast transistors and high-frequency nanoelectromechanical resonators, the two applications described in this chapter and later in the thesis.

Transistors are interesting both to learn more of the electronic characteristics of the materials and as potential successors to silicon in future microprocessors, and are used in Paper V. Resonators can be used both for fundamental studies of nanomechanics and for applications such as mass sensing [43]. Similar devices are studied in Paper III, IV and V.

3.1 Transistors

The transistor is the foundation of modern information technology. Faster and cheaper electronics has changed the world by making computers and cell phones available to the large masses. This development has been achieved through improvements of silicon-based transistor designs, made possible by improved methods for microfabrication. In the future however, further miniaturization of silicon transistors will not improve their performance anymore and the possibility to use other materials has to be investigated [44].

The field effect transistor (FET) is a three terminal device where the current between two of the terminals, the source- and drain-electrodes, is controlled by the voltage on the third, the gate-electrode. In conventional transistors the channel between source and drain is made of doped, semiconducting silicon and is separated from the gate by a thin insulating oxide. The gate-voltage turns the drain-current on and off by controlling the position of the Fermi level with respect to the band gap, hence the number of charge carriers in the channel and its conductivity.

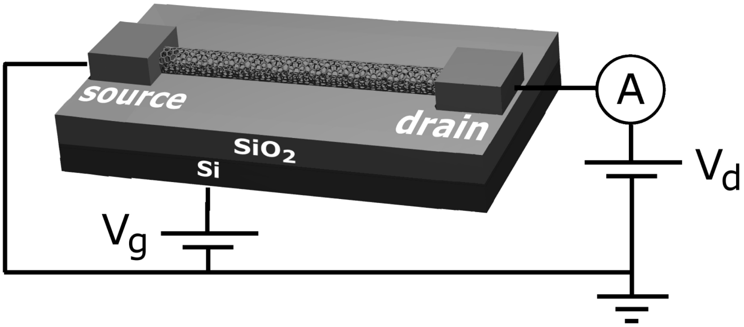

Figure 3.1: Schematic image of a carbon nanotube field effect transistor.

The material of the channel can be replaced with graphene or carbon nanotubes. In both cases often metal is used for source- and drain-electrodes. Typically the substrate is doped silicon with oxide on top to act as back gate and gate-oxide, respectively. A carbon-based field effect transistor is schematically shown in figure 3.1.

The performance of a transistor can be obtained by measuring its transfer characteristics, which is done by measuring the drain current, I_d, at a constant source-drain-voltage, V_d, while sweeping the gate-voltage, V_g. Transfer characteristics using graphene or carbon nanotubes as channel material are presented in figure 3.2.

For a transistor to be used in logic computation it should have a sufficiently large difference between on and off states, measured as the ratio between I_on and I_off. Another requirement is that a sufficiently small change in gate-voltage is needed to switch the state from on to off, which is measured from the slope in the transfer characteristics when going from on to off state and called the inverse subthreshold slope, S.

Graphene, being a zero band-gap semiconductor, conducts well for all gate-voltages as seen in figure 3.2a. Around the point of minimum conductance, the Dirac point, the current can be slightly changed by the voltage on the gate. This is due to a change in the number of charge carriers with applied potential. The low on-off-ratio in graphene make it unusable in logic applications. Still

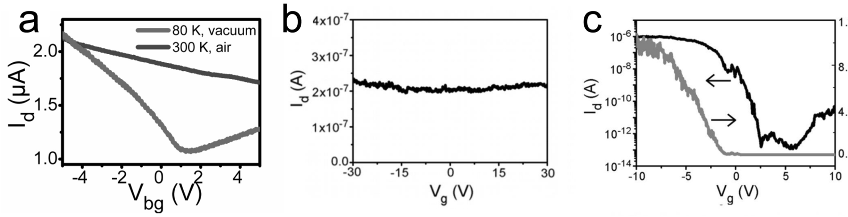

Figure 3.2: Transfer characteristics of a graphene beam (a), a metallic SWNT (b) and a semiconducting SWNT (c).

the high mobility of the charge carriers and low contact-resistance enable high-frequency applications [1].

A band-gap can be opened up in graphene, e.g. by spatial confinement. The band-gap of graphene nanoribbons can be engineered by controlling their width [20]. To make logic operations possible at room-temperature widths below 10 nm are needed, a length-scale presently impractical for mass-fabrication.

The transfer characteristics of a metallic SWNT, figure 3.2b, show a constant I_d for all V_g. A semiconducting SWNT, figure 3.2c, typically has a maximum I_d for negative V_g, a low I_d for intermediate V_g and a slightly higher I_d for positive V_g. This makes metallic CNTs useful for metallic interconnects [45] while semiconducting CNTs have potential for logic circuits.

In a carbon nanotube field effect transistor (CNTFET) the transport characteristics are typically not dominated by the channel but by the potential barriers between CNT and metal contacts. These barriers, called Schottky barriers, are due to the mismatch in work-functions and are problematic since they reduce I_on and switching speed [46].

The work-function of the contacts, hence their material, determines the carriers of current. If negative electrons dominate the conductance the transistor is said to be of n-type. If instead positive holes dominate conductance it is of p-type. If palladium is used as contact metal, the work functions match and the barriers can be removed for holes [47].

Properties that make carbon nanotubes suitable for use in transistors are their long mean free path and high mobility [48]. Advantageous are also their small dimensions and simple integration with suitable gate dielectrics [49], which improves their electrostatic control and switching speed.

The use of graphene and carbon nanotubes in mass-produced transistors is not possible today. The main obstacles are not the intrinsic electronic properties of the materials themselves but the requirement for control in material synthesis and device fabrication on the atomic level to fully control the transistor characteristics. Although this may not be impossible to control in the future, probably other electronic devices will find the use of these materials before we have carbon-based transistors in our computers.

3.2 Nanomechanical resonators

Nanoelectromechanical systems (NEMS) are promising to use for a number of scientific and technological applications. Resonators, suspended beams vibrating similar to a guitar string, have been proposed for use in sensitive mass detection [50] and for exploring quantum phenomena [51].

Suspended graphene has been obtained using exfoliation on top of predefined trenches [52], by etching the substrate under exfoliated graphene [53] or grown by chemical vapor deposition [54]. Similar to the first method, carbon nanotubes can be grown first and suspended by removing the substrate or grown directly across a trench, as seen in figure 3.3a. The latter methods are similar to what is shown in figure 2.1, a resulting beam is shown in figure 3.3b.

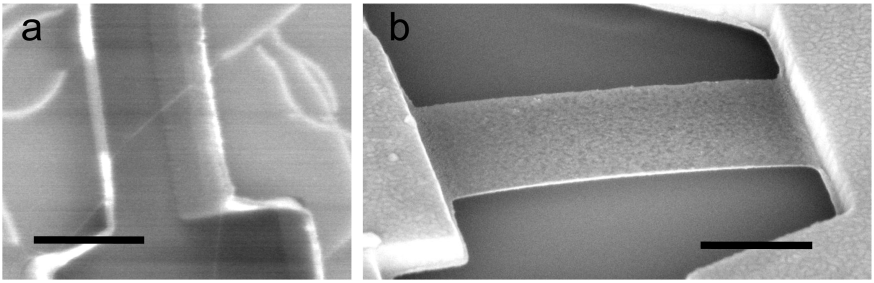

Figure 3.3: (a) Image from SEM of a suspended carbon nanotube. (b) Image from SEM of a suspended beam of bi-layered graphene. Scale-bars are 1 μm.

Both graphene and carbon nanotubes can be electrostatically actuated, deflected, due to their conductive nature. A gate-voltage applied to the substrate, thus acting as a back-gate, induces additional charge, q, on the beam. The attraction between this charge and its mirror charge on the gate gives rise to an electrostatic force

$$F_{\mathrm{el}} = \frac{1}{2}\frac{dC_{\mathrm{g}}}{dz}{V_{\mathrm{g}}}^{2}, \tag{3.1}$$

where $\frac{dC_{\mathrm{g}}}{dz}$ is the derivative of the capacitance with respect to the distance between beam and gate. Thus by applying an alternating V_{g} at a frequency close to resonance the beam will vibrate.

The motion gives rise to a change in conductance proportional to the change in added charge on the beam described by [55]

$$\delta q = \delta(C_{\mathrm{g}}V_{\mathrm{g}}) = C_{\mathrm{g}}\delta V_{\mathrm{g}} + V_{\mathrm{g}}\delta C_{\mathrm{g}}, \tag{3.2}$$

where the first term is the standard transistor gating effect and the second term is non-zero due to the movement of the beam.

The conductance of graphene and semiconductor SWNTs varies with the added charge, i.e. with changed V_g as shown in figure 3.2 or by motion of the beam as described in equation 3.2. The change in source-drain-current can then be used to electrically read-out the movement of the beam. By measuring the conductance at different driving frequencies the frequency of resonance can be found [55].

Static deflection can be imaged using scanning electron microscopy [56] or atomic force microscopy for carbon nanotubes [57] and graphene [58]. Vibrating motion of both systems can be monitored using scanning probe microscopy [59] [60]. For motion of graphene, detection can also be made optically by interferometry [52].

Despite their atomic nature the motion of both CNT [61] and graphene [62] resonators can be well described by classical continuum mechanics. Then the frequency of resonance for the first mode, ω_res, is given by [50]

$$\omega_\mathrm{res} \sim \frac{1}{L^2}\sqrt{\frac{E}{\rho}}, \tag{3.3}$$

where L is the length of the beam, E is the Young's modulus and ρ is the mass density of the beam. Both graphene and carbon nanotubes are promising for high-frequency applications due to their small lateral size, high Young's modulus and low mass density. NEMS resonators with resonance-frequencies of hundreds of megahertz have been obtained using carbon nanotubes [55] and graphene [43].

Carbon-based resonators are promising for direct studies of quantum mechanics, which require cooling into the quantum regime where $k_bT < \hbar\omega_\mathrm{res}$ [63]. Hence a high ω_res puts lower demands on cooling, making the quantum limit within reach experimentally. Also detection is facilitated since the amplitude of the zero-point fluctuations is given by $\Delta x_0 = \sqrt{\hbar/(2m\omega_\mathrm{res})}$ [63], thus the small masses of beams of CNTs and graphene are advantageous.

Carbon-based resonators not only operate at high frequencies, but due to their small bending rigidity tension is important for the vibrations [64]. The tension can be controlled, by applying a static electrostatic force on the beam. Including tension adds a term to equation 3.3, hence ω_res can be tuned and due to their large elasticity increases of 200 % have been observed both for SWNTs [55] and graphene [43]. Combined with high fundamental resonance frequency this tunability enables applications in tunable RF-resonators.

The quality factor, Q, is a measure of the damping in the resonator. To obtain high quality factors it is important to have very clean beams. Since lithography easily leaves resist residues on the substrate this has been obtained for nanotubes by having synthesis as the last step in fabrication [65] and for graphene by using lithography-free processing [66]. The quality factor has also been shown to improve by reducing the amplitude of the driving voltage [67] and by lowering the temperature [68].

An application for resonators is mass sensing. The addition of extra mass, for example adsorption of molecules, to the beam shifts its resonance frequency. Thus the addition of a small extra mass, δM, can be detected by measuring the change in vibration amplitude or resonance-frequency. The smallest measurable shift in mass follows the expression [50]

$$\delta M \sim \frac{M}{\sqrt{Q}\omega_{\mathrm{res}}}, \tag{3.4}$$

where M is the mass of the beam. For a mass sensing resonator to have a low detection-limit the mass of the beam should be low while the quality factor and resonance frequency should be high.

With its high Young's modulus and low density, giving a high ω_{res} according to equation 3.3, together with atomic thickness giving low mass, carbon nanotubes [69] and graphene [70] are very promising materials for mass sensing with detection limits of single atoms. In order to realize these applications with suspended beams of graphene or carbon nanotubes, optimization of fabrication and measurement techniques is needed to improve resonance frequencies and quality factors.

Chapter 4

Synthesis of carbon nanotubes

The growth mechanisms of carbon nanotubes are not clearly understood due to the complexity and interplay between the processes. It is still considered as an art to select the right materials and process parameters to grow a specific type of carbon nanotubes [21].

This chapter describe how the kinetics of synthesis is related to the microscopic processes involved in growth of carbon nanotubes. The results are used to obtain a deeper understanding of the mechanisms controlling synthesis of carbon nanotubes.

4.1 CVD-synthesis

The basic requirements for growth of carbon nanotubes are a catalyst nanoparticle, a source of carbon and excess energy. In thermal chemical vapor deposition the catalyst can be located on a substrate, the sources of carbon are the carbon-containing gas-molecules fed into the process atmosphere and the excess energy comes from heating the catalysts and the process atmosphere.

The carbon feedstock is decomposed on the catalyst nanoparticle, thus adding carbon atoms to the catalyst, while the rest-products from the feedstock are transported away in the gas-phase. The carbon atoms diffuse on the catalyst and start to connect to each other into carbon chains and rings forming a network bonded to the catalyst nanoparticle. When enough carbon atoms are dissolved the catalyst nanoparticle becomes saturated.

Continued carbon addition to the catalyst makes it supersaturated and due to the curvature of the nanoparticle it becomes energetically favorable for the carbon network to be lifted from the surface, forming a cap on the catalyst. The cap is at one end of the carbon nanotube and the other is at the edge between nanotube and catalyst, which is kept open due to the binding strength between catalyst and carbon atoms at the edge [71]. When more carbon atoms are added they diffuse through the particle to the edge of the

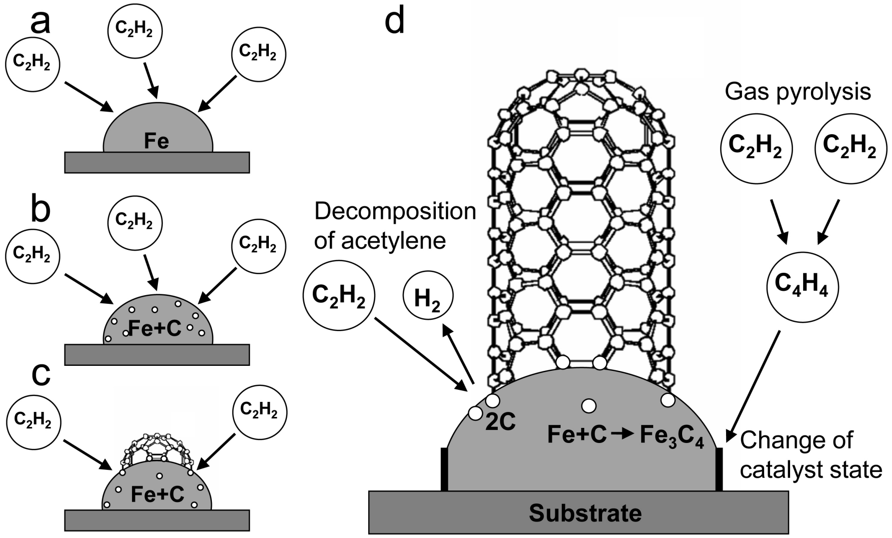

Figure 4.1: Schematic images of the initial stages of CNT-growth. (a) Molecules of carbon feedstock impinge on the catalyst nanoparticle. (b) The feedstock is decomposed and carbon atoms are dissolved into the nanoparticle. (c) Carbon atoms aggregate and bond into a cap, that is lifted of the nanoparticle. (d) Continued addition of carbon atoms increases the length of the nanotube. The growth-rate depends on the rate of feedstock decomposition. The poisoning-rate depends on the rates of gas pyrolysis and change of catalyst state.

carbon nanotube, where they are incorporated and thus increase the length of the carbon nanotube.

The growth model described above and shown in figure 4.1 is called the vapor-liquid-solid model, since atoms come from gas phase and via a disordered state form a solid structure, and was originally developed to explain the formation of silicon wires [72] and later extended to apply to CNT formation [73]. The model was thought to require molten catalyst to allow for bulk diffusion of carbon atoms, but low-temperature growth of CNTs has shown that surface diffusion could be sufficient [74].

4.1.1 Kinetics of carbon nanotube growth

A carbon nanotube will continue to grow until the supply of carbon is stopped. The addition of carbon to the nanotube involves many processes, for example decomposition of the carbon feedstock, diffusion of carbon atoms in the nanoparticle and incorporation of carbon into the nanotube. The slowest process involved will limit the growth-rate of the carbon nanotubes, ρ.

Termination of growth could be due to either stopped addition of carbon feedstock to the process atmosphere or poisoning of the catalyst nanoparticle. In the last case, supply of carbon feedstock is prevented by a carbon-coating formed on the nanoparticle or by carbide formation in the catalyst giving much slower carbon diffusion, the processes are shown in figure 4.1d. It has also been proposed that termination of growth is caused by restructuring of the catalyst by Ostwald ripening [75].

The time of growth, τ, is determined by the rate of the processes causing poisoning. From catalyst poisoning of individual nanoparticles it is expected that the growth-rate declines exponentially. For some conditions this has also been observed [76]. Using acetylene to grow vertically aligned nanotube arrays (VANTAs) it has been found that growth is well described by equation 4.1 with constant rate of growth until sudden termination [77][78][79].

The termination length, λ, can then be approximated by assuming that the nanotubes have a constant growth-rate during the time of growth and then suddenly stop growing. The length of the nanotubes grown will therefore be given by

$$\lambda = \rho \cdot \tau, \tag{4.1}$$

where λ and τ are known and ρ can be calculated or λ and ρ are known and τ can be determined.

Studies of the kinetics, i.e. the rates, of nanotubes growth and poisoning can not only be used to describe the macroscopic properties of the synthesis. Since the growth- and poisoning-rates depend on atomic processes the kinetics forms a link between macroscopic properties and microscopic processes. This makes it possible to determine rate-limiting processes, not possible to observe directly, through the study of kinetics.

4.1.2 Catalyst

The first requirement for growth of carbon nanotubes is an active catalyst made of a material with sufficient binding-strength to carbon to prevent the opposite end of the CNT to close itself [80]. Traditionally the materials considered have been the transition metals iron, cobolt and nickel. It has been shown that also gold, silver and copper can be used as catalyst material, although then conditions of growth are more limited [81]. For the cap to spontaneously lift-off the catalyst nanoparticle has to have a curvature corresponding to a diameter of roughly 10 nm or less to form SWNTs.

It has been found that CNT diameter is related to catalyst diameter [82]. The most energetically favorable cap formed is the largest possible, i.e. with the same diameter as the nanoparticle, since then the largest number of the strong carbon-catalyst bonds and lowest strain energy is achieved. During cap formation it is not always the structure giving globally lowest energy that is formed, instead lifting of a smaller cap at an earlier stage could form a local minimum in energy. Due to the fast addition of more carbon atoms prolonging the tube the cap has usually not found the optimal structure [33]. Thus the relation between CNT and catalyst nanoparticle diameters is not as simple as them being equal but instead it is dependent on the thermodynamics of the growth conditions used.

A layer of catalyst material can be deposited using thin-film evaporation forming a thin and uniform layer. When heated up before growth the atoms start to diffuse on the surface into larger agglomerates forming the catalyst nanoparticles. In this process the nanoparticles have a broad distribution of sizes [83].

The catalyst material on substrates can be patterned using lithography. Catalyst areas are formed by patterning a layer of resist before catalyst deposition and then removing the resist. Growth of CNTs will then occur only in the areas of the substrate patterned with catalyst [84], as shown in figure 4.2. Patterning of catalyst enables control of which areas CNTs are grown from thus forming a step towards large-scale production of nanotube-based devices.

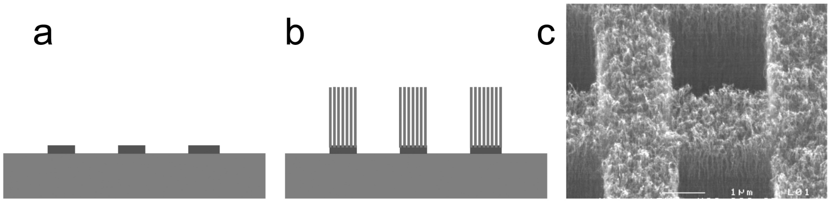

Figure 4.2: (a-b) Schematic images of synthesis from patterned catalyst areas. (a) Catalyst material is patterned. (b) During synthesis carbon nanotubes are only grown in areas with catalyst. (c) SEM-image of carbon nanotubes grown from patterned catalyst areas. Scale-bar is 1 μm.

Instead of depositing the catalyst directly on the substrate a support layer can be used. The role of the support could be to increase the surface area and thus the yield of CNT for small samples [85]. The support can also be used to control catalyst size distribution by reducing diffusion length when nanoparticles are formed [86]. A supporting layer can also enable growth on otherwise incompatible substrates such as silicon, where the catalyst material forms silicide without a supporting layer acting as diffusion barrier [87].

Depending on the adhesion between catalyst and substrate base- or tip-growth could occur. If interaction with the underlying substrate is strong the catalyst will remain stuck to the substrate and the grown CNT extends out from it, which is known as base-growth and shown in figure 4.1. In tip-growth the catalyst nanoparticles are instead on top of the nanotubes while the other ends are stuck to the substrate. Thus the material of substrate and catalyst decide which growth-mechanism will occur. In some cases also the growth conditions used can influence the growth mechanism, for example fast-heating has been seen to promote tip-growth of longer SWNTs while slower heating gives base-growth of shorter SWNTs [88].

It can be noted that the catalyst during CNT synthesis often is transformed into carbide, which is one of the mechanisms believed to stop growth. This is in conflict with the standard definition of a catalyst, since then it should facilitate a reaction without being consumed. It is also uncertain whether the main role of the catalyst nanoparticle is to facilitate the cracking of carbon feedstock or carbon incorporation into CNT. Instead, it could be to provide a growth site for the CNT in the initial stage and enable continued growth.

4.1.3 Synthesis atmosphere

Carbon is added to the catalyst nanoparticles in the furnace through the process atmosphere during synthesis of carbon nanotubes using chemical vapor deposition. In order to achieve controlled conditions during growth, enabling reproducible results, care has to be taken of which gases are used during heating of the furnace, synthesis and cooling of the furnace, respectively. The pre-treatment stage should restructure the catalyst film into nanoparticles in an active state. The growth stage should add carbon to the catalysts making possible formation of CNTs with desired properties. During the last step of cooling after synthesis the quality of the carbon nanotubes should be kept unaffected or even improved.

In the pre-treatment step the atoms in the thin film of catalyst material start diffusing due to the increasing thermal energy during heating. During diffusion the atoms will assemble into nanoparticles to minimize surface energy of the catalyst and substrate material. Larger nanoparticles will have a smaller fraction of surface atoms, thus lower surface energy per atom. On the other hand this leads to more of the substrate being exposed, increasing the surface energy of the substrate. Thus the restructuring of the catalyst should minimize surface energy of the whole system.

The diffusion of the catalyst atoms into clusters of a few atoms is fast since individual atoms diffuse easily. Diffusion of clusters is slower and becomes even slower as cluster size increases. The pre-treatment only lasts for a limited amount of time so the diffusion into larger particles might not be given enough time to reach equilibrium. In that case the size-distribution and density of catalyst particles depends on time of pre-treatment [89].

The size-distribution of catalyst nanoparticles also depends on the process atmosphere. Different gases give different surface energies of catalyst and substrate, changing the structure that minimizes the energy. Also gas molecules can absorb on the surfaces and change diffusion-rates. Hydrogen and ammonia are common gases used during pre-treatment giving different structure of catalyst [90]. Both gases are reducing in order to remove the native oxide formed on the catalyst material.

When the catalyst has reached the desired structure the carbon feedstock is added to the process gases. The molecules of the inserted carbon source should be broken down at the catalyst to provide carbon material for growth of CNTs, shown schematically in left-hand side of figure 4.1d. Common examples of carbon precursors are the hydrocarbons acetylene, ethylene and methane. When broken down these form molecular hydrogen as the byproduct, which re-enters the process atmosphere and is transported away.

Acetylene (C_2H_2) is a very reactive molecule which is easily broken down and thus enables growth of carbon nanotubes at relatively low temperatures. The high reactivity of the acetylene molecule also makes it suitable for fast and dense growth of CNTs. When CNTs grow with a certain density and an initial speed they will support each other and start growing in a vertically aligned nanotube array where the CNTs grow vertically out from the substrate, as shown in figure 4.2. Those nanotube structures can be grown by using for example carbon-rich acetylene [91] or ethylene [92].

Methane (CH_4) is less reactive and thus requires higher process temperature to grow carbon nanotubes. It has theoretically been predicted that the number of walls a carbon nanotube gets during synthesis depends on the rate of carbon addition to the catalyst compared to the diffusion-rate into the CNT-structure [93], which means that a higher rate of added carbon gives more CNT-walls. That could be used to understand why synthesis using less-reactive methane usually gives SWNTs [94] whereas more-reactive acetylene gives MWNTs [91].

It has been shown that acetylene is much more efficient than other small-molecule precursors and can be regarded as a direct building block for CNT formation [95]. However it should be remembered that due to the high temperature the carbon-containing gas molecules will not only react at the catalyst but also in the gas-phase. Pyrolysis of the carbon precursors while they are transported toward the catalyst could change the composition of gases from the inserted gases to a mixture between many reactive species, shown schematically in right-hand side of figure 4.1d.

Some species formed in pyrolysis could be essential for growth of carbon nanotubes. Other might instead be responsible for the termination of CNT growth. The latter could be the result of larger molecules, formed by pyrolysis, creating an amourphous carbon overcoating on the catalyst nanoparticle [91]. The overcoating reduces the available area of the active catalyst and eventually covers it completely, thus terminating addition of carbon to the CNT.

An oxidizing gas can be added to the reaction to increase the time before poisoning of catalyst. Since amorphous carbon that forms the overcoating is more reactive than graphitic carbon that forms the carbon nanotubes, a small amount of oxidizer might clean the catalysts without damaging the nanotubes [96]. It has also been proposed that addition of oxidizing water reduces Ostwald ripening of the catalysts [75]. Both effects prolong the time of growth.

4.2 Experimental setup

In the TCVD-system used at the University of Gothenburg, shown in image 4.3, heating is done by a furnace. The substrate, with catalyst material, is positioned in the middle of the furnace inside a quartz-tube. The quartz-tube is sealed from the ambient atmosphere and filled with gases that form the process atmosphere. During processing, the furnace heats the substrate with catalysts and the process atmosphere. Since the temperature of the furnace is highest in the center and lower close to the edges it is important to put the substrate at the same position to be able to compare results of synthesis from run to run.

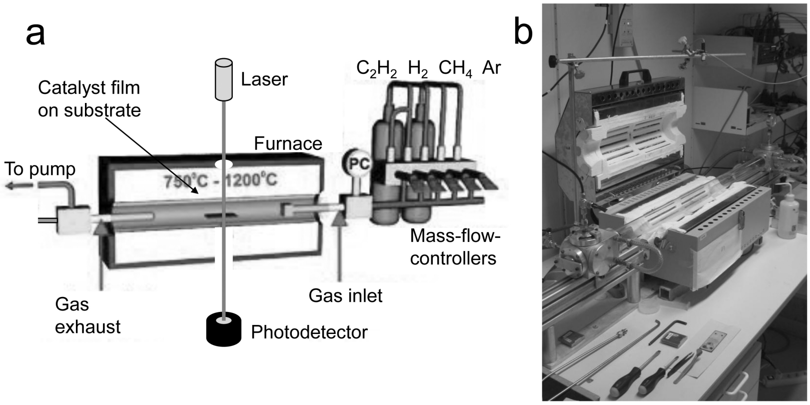

Figure 4.3: (a) Schematic image of the furnace TCVD-system (b) Photograph of the furnace TCVD-system.

Mass-flow-controllers (MFCs) are used to be able to control the proportions of the gases in the process atmosphere. Each gas, for example argon, hydrogen and methane, is fed into the tube from its gas line via an MFC set to control the flow-rate of that gas to a certain value. Although synthesis always takes place at atmospheric pressure in this setup the total flow-rate of the gases and thus their partial-pressure can be controlled using the MFCs.

Even if the gas composition fed into the quartz-tube can be controlled it will be changed when reaching the zone heated by the furnace. The thermal energy given to the gas-molecules will initiate pyrolysis, transforming them into different species. The resulting species will depend on initial gas-composition, process-temperature and -time. Thus the composition of process gases will vary along the furnace, which is yet another reason to put the samples at the same position to be able to compare different runs.

4.2.1 Laser absorption measurements

To be able to study the synthesis of CNTs *in situ* a 670 nm laser-diode illuminates the sample during growth and the intensity of the transmitted light is measured by a photodetector, as shown in figure 4.3a and 4.4a. If a transparent substrate, such as quartz or fused silica, is used synthesis of CNTs on it can be monitored by measuring the intensity of the light transmitted through it.

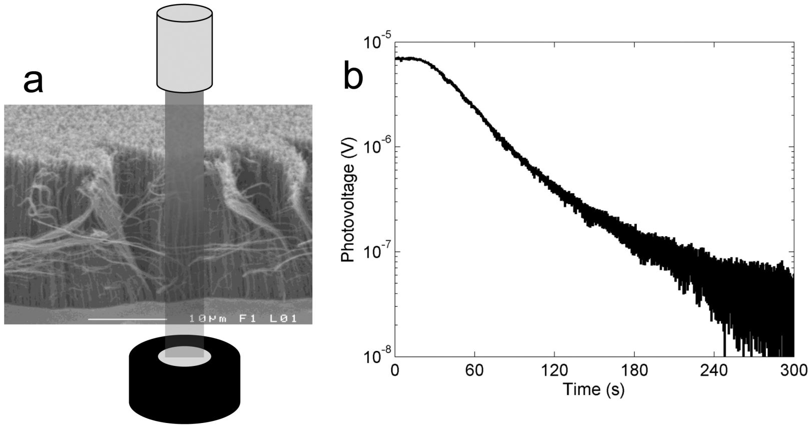

Figure 4.4: (a) Schematic image of laser absorption by CNTs. (b) Measurements during synthesis of the photovoltage, which is proportional to the intensity of the transmitted light.

When vertically aligned nanotube arrays are grown on a substrate light shining upon the array is absorbed. The longer the tubes are the more will light be absorbed according to

$$I = I_0 \cdot e^{-\alpha \cdot h}, \tag{4.2}$$

where I and I_0 are the intensity of light transmitted through the substrate after and before growth of the VANTA, α is the absorption coefficient in the VANTA and h is the height of the grown VANTA. Thus the height of the VANTA can be measured during synthesis by measuring the transmitted intensity of light [97].

The absorption coefficient depends on the density of nanotubes and their effective extinction cross-section has been used to probe *in situ* the density of nanotubes [98]. Its value is obtained by stopping growth of VANTAs and calculating α from the measured absorption and height.

Since carbon nanotubes absorb light very well, even better than any other object yet found [99], the simple setup used in our system can only be used to study the growth of VANTAs during initial synthesis when a sufficient amount of light is transmitted. In our setup, when CNTs grow above heights of 40 μm the laser absorption measurements are limited by the sensitivity of the photodetector. Still they give important information on the initial growth-rates of VANTAs.

4.2.2 Synthesis conditions

In a typical run of synthesis of carbon nanotubes in the TCVD-system at University of Gothenburg, described step by step in appendix A, between 1 and 8 pieces of cm-sized samples are loaded into the quartz-tube in the center of the furnace. The sample used for laser absorption measurements is checked to be positioned in the beam-line and the intensity of the transmitted light is measured. After sealing of the quartz-tube the ambient atmosphere is pumped out and argon and hydrogen is inserted during heating of the furnace.

When the process temperature is reached the catalyst thin film has already started to diffuse into clusters which in turn diffuse into larger particles. Usually iron is used as catalyst material and when stored in ambient atmosphere native oxide is formed. The hydrogen-gas fed into the process chamber reduces the iron back into its elemental state. Hydrogen is also adsorbed on the surface of the iron particles and reduces the diffusion-rate, thus increasing the time needed to form particles of a certain size [89]. The pre-treatment step typically lasts for 10 minutes after reaching the process temperature.

When the carbon feedstock is introduced to the process gases it still has to be transported through half of the quartz-tube before reaching the substrate. This can be seen in the laser absorption measurements by the time between introduction, when measurements start, and the time carbon nanotubes start reducing the transmitted light of the laser, see figure 4.4b.

To avoid back-flow of process gases the gas-lines are at over-pressure. Opening of the gas-line thus results in a burst of carbon feedstock. The burst lasts for a period of time, until the MFC has responded and closed its valve enough to set the flow to the desired value. If the burst is introduced to the process chamber the sample will experience a substantially higher partial pressure initially before it reaches the nominal value.

An optional method of gas-introduction is to let the initial gas-burst bypass the process chamber and be led directly into the exhaust and let the process gases into the chamber only after the set flow-rates are reached. The latter method will henceforth be referred to as flow synthesis whereas the former will be called burst synthesis.

For growth of VANTAs the density and growth-rate of carbon nanotubes should be large enough to enable them to support each other to grow vertically. Thus carbon-rich and easily cracked acetylene is added to the process gases as carbon feedstock, usually at a process temperature of 700 °C, while the decrease of intensity of transmitted light is measured. The flow-rate of acetylene is typically less than 1 % of the total gas-flow.

For growth of SWNTs, the less carbon-rich feedstock of methane is used. Methane also requires higher energy to be decomposed, thus the process temperature of 900 °C is higher than in acetylene-synthesis. When starting SWNT-synthesis the gas composition is changed from argon and hydrogen to methane and hydrogen with 90 % of the total gas-flow being methane.

Synthesis is stopped when the supply of carbon feedstock is stopped. While the furnace is cooling down gases are changed to be similar to the pre-treatment step. During cooling the role of hydrogen is to react with amorphous carbon to make the surface of CNTs and substrates cleaner. As in previous steps argon is used as a dilution gas to reduce the partial pressure of the other gases in the composition. When the temperature is reduced enough to allow for sealing of the tube to be broken, the samples with CNTs grown on top can be taken out and are ready for *ex situ* characterization.

4.3 Vertically aligned nanotube arrays

Vertically aligned nanotube arrays are made up of carbon nanotubes aligned vertically from the substrate during synthesis. Individual CNTs usually can not stand vertically, due to their high aspect-ratio. However CNTs can support each other to collectively grow vertically, when their density and growth-rate is sufficiently high.

A sample, fully covered by a VANTA after synthesis, appears totally black as seen from the top with the naked eye. To be able to study the detailed structure, electron microscopy has to be used. In the images below an as-grown VANTA is studied from the side by SEM and a CNT from a VANTA is studied in TEM.

In figure 4.5a a VANTA is seen from the side over its entire height. Between the bottom and top, marked by black lines in the left of the image, vertical bright and dark lines can be seen. These lines are the vertically grown carbon nanotubes. It can be noted that the wall of the VANTA appears flat without any CNTs growing out from it. Also the top of the VANTA seems flat and no individual CNTs are sticking up, thus the VANTA naturally forms a well-defined box with CNTs inside but not outside.

When looking closer on the wall of the VANTA, as in figure 4.5b, it can be seen that the vertically aligned nanotubes are not perfectly aligned. Instead the CNTs wiggle to the sides back and forth along their length, altogether giving a net vertical alignment. The CNTs seems to cross each other and form a network where the nanotubes are connected to their neighboring CNTs at different parts.

During growth of a VANTA the CNTs are constricted by the other nanotubes. The tubes will bend until they come into contact with a neighbouring tube and adhere to it via Van der Waals interactions. Continued growth of

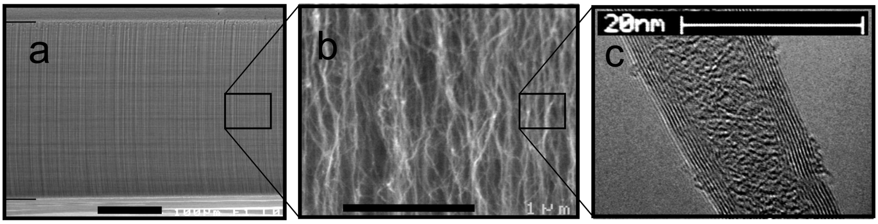

Figure 4.5: (a) SEM-image of a vertically aligned nanotube array. Scale-bar is 100 μm. (b) SEM-image at higher magnification of a vertically aligned nanotube array. Scale-bar is 1 μm. (c) TEM-image of the microstructure of a multi-walled carbon nanotube. Scale-bar is 20 nm.

the CNTs will bend them in other directions and give them their wiggling shape. A consequence of the non-ideal vertical alignment is that the lengths of individual nanotubes are longer than the height of the VANTA [100].

The height of the VANTA is increased by the collective pushing of the top from the growing CNTs until growth is terminated. However it is not necessary for all nanotubes to have the same growth-rate, since faster growing tubes will get a more wiggling shape than those with a slower growth rate in the same VANTA [101].

Since the nanoparticles formed from a thin film have a distribution of sizes [89] it can be expected that there is a distribution also in growth-rate and -time for the nanotubes forming the VANTA. However it is not fully known if the collective growth-rate of the VANTA is limited by the slowest growing nanotubes or determined by the mean growth-rate, nor how the growth-time of the individual nanotubes is influenced by the other nanotubes in the collective [78].

The microstructure of individual carbon nanotubes is studied using TEM. The images can be thought of as showing a cross-section of the nanotubes, making it possible to measure the diameter and number of walls. The microstructure depends on the conditions used during synthesis. In our studies of VANTAs grown using acetylene usually the diameter varies from 5 to 10 nm and the number of walls from 2 to 10.

Figure 4.5c is an image from transmission electron microscopy showing a nanotube from a VANTA. The walls of the multi-walled nanotube are seen as black fringes, which can be counted to be nine in this image. The distance between the walls in a MWNT is 0.335 nm [93], giving a hint of the resolution obtainable using TEM. However the CNTs in a VANTA have a distribution of microstructures, raising the need for many images to study a single sample.

When growing from a patterned catalyst film, the VANTAs will preserve the shape of the pattern. CNTs will grow only from areas with catalyst material, thus the initial network forming the top of the VANTAs will be created only in those areas. The nanotubes pushing the top network will continue to grow from catalyst areas. Hence a square-shaped catalyst pattern will give a square-shaped pillar of vertically aligned nanotubes, which are kept together by Van der Waals-forces.

An interesting aspect of pillars of vertically aligned nanotubes is that they, to some extent, show properties similar to individual nanotubes. In resemblance to how a nanotube bends during growth a pillar of nanotubes also bends when the mechanical stability can not maintain vertical alignment. Pillars of nanotubes can support each other during synthesis to improve vertical alignment, just as nanotubes during synthesis of the VANTAs forming the pillars.

For pillars growing close to each other, the pillar spacing has an effect on alignment. In figure 4.6 pillars with 4 μm width are grown in a quadratic pattern with different distances between the pillars. Individual pillars of 4 μm diameter have poor vertical alignment, but when grown in arrays the pillars support each other. As their separation decreases the vertical alignment increases and when it is 2 μm the pattern looking down on the top of the pillars resembles the catalyst pattern, indicating excellent vertical alignment, as seen in figure 4.6c.

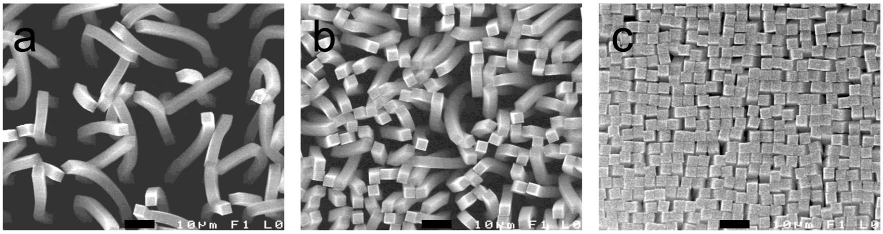

Figure 4.6: SEM-images of arrays of VANTAs. Pillars are 4 μm wide and are separated by 10 μm (a), 5 μm (b) respectively 2 μm (c). Scale-bars are 10 μm.

There seems to be a close resemblance between vertical alignment of nanotubes and pillars of nanotubes during synthesis. The bending of pillars can be reduced by decreasing the spacing between pillars. Thus the wiggling of nanotubes in a VANTA may be reduced if the density of catalyst nanoparticles nucleating the growth of CNTs can be increased.

4.4 Kinetics of synthesis of VANTAs

A VANTA appears to be a black box on top of the substrate. The kinetics of the synthesis of a VANTA, i.e. the rate at which the nanotubes grow, is a consequence of the rate of the fundamental reactions that eventually produce the final product. Important information can be obtained by determining the dependence of the growth rate on process parameters such as temperature and pressure. Thus studies of the kinetics provide a tool to link the microscopic world of reacting molecules to the macroscopic world of synthesis conditions. Hence a VANTA can be used as the black box of synthesis, which provides information about how it proceeded and why it stopped.

4.4.1 Temperature of growth

The incorporation of carbon atoms into a carbon nanotube involves the processes of molecules of the carbon feedstock being adsorbed and cracked on the catalyst nanoparticle. The carbon atoms are transported by diffusion to the edge between nanoparticle and nanotube, where they are incorporated into and increase the length of the CNT.

The completion of each event of the reaction requires an energy barrier to be surmounted, which has a probability that depends on the thermal energy available in the process. How often a carbon atom is added also depends on how often carbon atoms attempt to be incorporated, for example the rate of molecules impinging on the catalyst. The number of carbon atoms per unit length of the CNT, varying with diameter and number of walls, relates the addition-rate of carbon atoms to the growth-rate of the carbon nanotube.

Mathematically this can be described by an Arrhenius expression. The growth rate, ρ, can be described by the expression

$$\rho = C_{\mathrm{a}} \cdot A \cdot e^{-\frac{E_{\mathrm{a}}}{k_{\mathrm{b}} T}}, \tag{4.3}$$

where C_a is the increase in length per added carbon atom, A is the attempt frequency of surmounting the energy barrier, E_{a}, to add a carbon atom and $k_{\mathrm{b}}T$ is the thermal energy available.

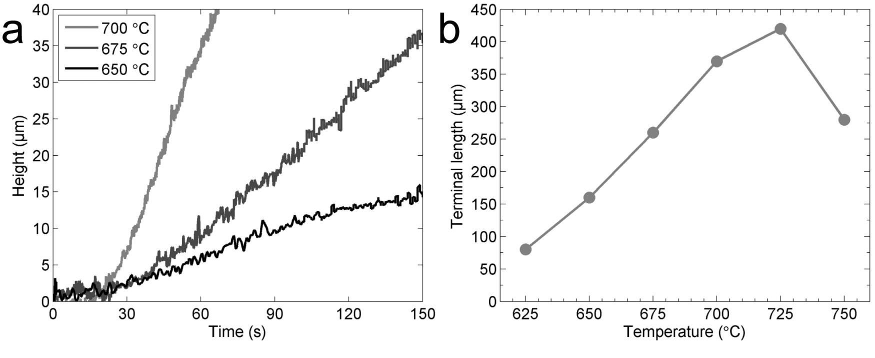

Figure 4.7: (a) Laser absorption measurements at different temperatures in flow-synthesis. (b) Measurements of the terminal length of CNTs at different temperatures in burst-synthesis.

Measurements of the initial stage of growth using laser absorption, shown in figure 4.7a, qualitatively support equation 4.3. For the different synthesis conditions, an increase of growth-temperature gives an increase in growth-rate. Thus it is possible to anticipate that there exists a certain temperature needed to enable growth of VANTAs, which require a certain growth-rate to form.

Even though the growth-rate of CNTs increases with increasing temperature that is not always the case for their terminal length since then also the time of growth decreases due to increased rate of catalyst poisining. In figure 4.7b the terminal lengths of VANTAs grown at different temperatures are shown. There exists an optimal temperature for growth of VANTAs, where the ratio between growth-rate and rate of poisoning is maximized.

4.4.2 Acetylene flow-rate

The temperature during synthesis has been shown to have a great impact on the resulting carbon nanotubes. In the rate equations the dependence on process temperature is well defined, although that is not always the case with the activation energies [102]. The variation of the flow-rate of the carbon precursor, in this case acetylene, is another possibility to experimentally adjust conditions of synthesis.

The partial pressure of acetylene has an influence on the growth-rate of CNTs. The pre-factor A in equation 4.3 increases with increasing partial pressure, since there are more molecules of acetylene impinging on the catalyst nanoparticle.

It has been suggested that by varying the flow-rate of the carbon precursor the addition rate of carbon can be varied, and this can, in turn, influence the number of walls in the formed CNTs [93]. In CVD using gas pulses it has been shown that higher acetylene partial pressures shift the distribution of SWNTs to larger diameters [103].

Studies of kinetics of synthesis at different partial pressure of acetylene could provide further insight into the processes involved in the synthesis of carbon nanotubes. Such a study is made in Paper I. A description of the methods and results follow below, for a more thorough discussion the reader is referred to Paper I.

Experimental methods

Catalyst areas of 1 nm iron on 10 nm alumina were patterned, in the shape of 70 μm squares separated by 30 μm in an array of 5 mm width, on oxidized silicon. Catalyst material fully covering the substrate with the same thicknesses was also deposited simultaneously on transparent fused silica. Carbon nanotubes were grown at different flow-rates of acetylene, from 0.5 sccm to 60 sccm, in standard flow-synthesis. Details of the synthesis are found in appendix A.

Different flow-rates of the carbon precursor give different partial pressure of acetylene during synthesis. The process atmosphere consists of argon and hydrogen, with a flow-rate of 500 sccm each, and acetylene. During synthesis at atmospheric pressure, i.e. slightly above 1000 mBar, a flow-rate of 10 sccm gives a partial pressure of roughly 10 mBar acetylene.

Samples were grown for 30 minutes for all conditions. For flow-rates lower than 6 sccm it was found necessary to increase the time of synthesis to 60 minutes in order to reach the height of self-termination.

The growth-rates were studied *in situ* using laser absorption measurements on the fused silica-substrates. The heights of the VANTAs were measured by optical microscope and SEM on the silicon-substrates. The microstructures of the CNTs were studied in TEM by transferring CNTs from the silicon-substrates onto standard TEM-grids.

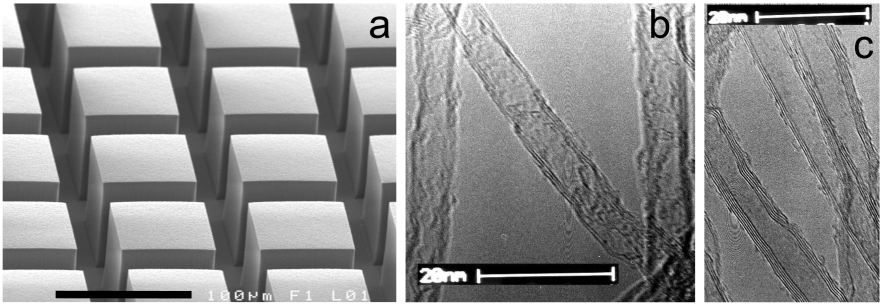

Figure 4.8: (a) SEM-image of VANTAs grown at 60 sccm in flow-synthesis. Scale-bar is 100 μm. (b and c) TEM-images of CNTs grown at 0.5 sccm (b) and 60 sccm (c) in flow synthesis. Scale-bars are 20 nm.

Results and Discussion

Vertically aligned pillars were grown at all conditions of synthesis, an example seen in figure 4.8a. The pillars consisted of multi-walled carbon nanotubes, as can be seen in figure 4.8b and c. Laser absorption measurements have been carried out during synthesis of VANTAs at different flow-rates of acetylene. The results are shown in figure 4.9a. The growth-rate increases with increasing flow-rate.

The curves in figure 4.9a were numerically derivated with respect to time to determine the initial growth-rates, shown as circles in figure 4.9b. It can be seen that the growth-rate increases with the flow-rate of acetylene. At high flow-rates the growth-rates keep increasing, but seem to approach a saturation value.

The terminal lengths of VANTAs are measured using an optical microscope, results shown as diamonds in figure 4.9b. Although the growth-rates of the

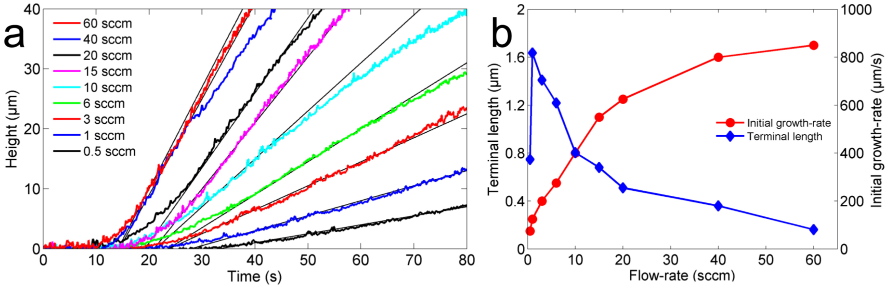

Figure 4.9: (a) Laser absorption measurements at different flow-rates. (b) Terminal lengths (diamonds) and initial growth-rates (circles) at different flow-rates of acetylene in flow-synthesis.

CNTs increase with flow-rate, their terminal lengths decrease. The only exception is for the very lowest flow-rate used in this experiment, 0.5 sccm.

Pyrolysis of the carbon feedstock is partly responsible for poisoning of the catalyst by forming a coating of amorphous carbon. Thus the time of growth is shortened for increasing partial pressure of acetylene. Thirty minutes of synthesis was sufficient for VANTAs to reach their terminal length at flow-rates of 6 sccm or more whereas sixty minutes of synthesis was necessary for flow-rates below 6 sccm.

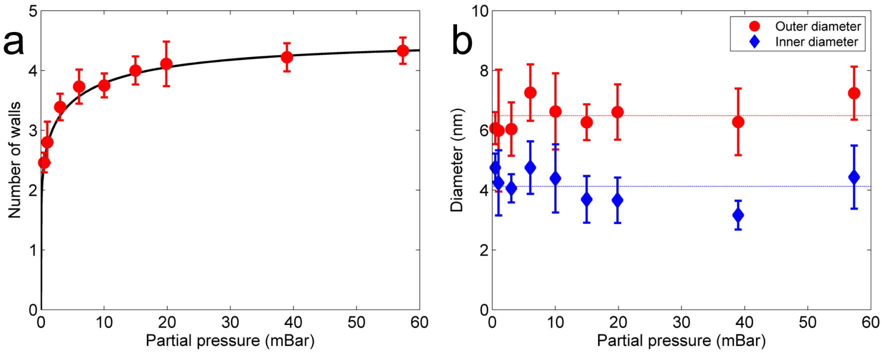

Figure 4.10: (a) The average number of walls of the CNTs grown at different flow-rates of acetylene. Circles represent measurements from TEM-images and solid line represents modelled data. (b) Average inner (diamonds) and outer (circles) diameter of the CNTs grown at different flow-rates. The mean inner and outer diameter are marked by striped lines.

The microstructure of the CNTs grown was studied using transmission electron microscopy, examples seen in figure 4.8b and c. The number of walls and diameters were measured, with results shown in figure 4.10. With increasing flow-rates of acetylene the number of walls in the formed carbon nanotubes increases. The diameter of the CNTs is on the other hand relatively constant in the interval of flow-rates used in this experiment.

The addition-rate of carbon atoms to the CNTs has been calculated from measurements by using the growth-rate, the number of walls and the number of carbon atoms per μm-length of a single wall of the CNT, given by

$$N_{\mathrm{C,SW}} = \frac{\pi \cdot d}{\sqrt{3/2} \cdot d_{\mathrm{C-C}} \cdot (3/2) \cdot d_{\mathrm{C-C}}} = 6.5 \cdot 10^5 \text{ atoms}/\mu\text{m}, \tag{4.4}$$

where d is the average diameter of 5.3 nm and $d_{\mathrm{C-C}}$ is the length of the bonds between the carbon atoms of 0.14 nm. The addition-rate of carbon-atoms, $N_{\mathrm{C,CNT}}$, is given by

$$N_{\mathrm{C,CNT}} = \rho \cdot N_{\mathrm{W}} \cdot N_{\mathrm{C,SW}}, \tag{4.5}$$

where $N_{\mathrm{C,CNT}}$ is the addition-rate of carbon atoms into the CNT, ρ is the growth-rate of CNTs and N_{W} is the number of walls. The results are represented by circles in figure 4.11.

The number of carbon atoms added to the catalyst nanoparticle via adsorption and dissolution of acetylene molecules can also be calculated. When the partial pressure of acetylene is increased more molecules impinge on the surface of the catalyst nanoparticle. However the sites on the nanoparticle where acetylene molecules can be absorbed are limited, and at higher partial pressure more of them will be occupied. This is described by the Langmuir adsorption isotherm

$$\Theta = \frac{K \cdot p}{1 + K \cdot p} \tag{4.6}$$

where Θ is the fraction of occupied adsorption sites, K is the equilibrium constant between adsorption and desorption and p is the partial pressure of acetylene. Obviously the fraction of occupied sites is between zero and one. At high partial pressures the fraction of available sites is low and an increase in flow-rate of acetylene only gives a low increase in adsorbed acetylene molecules. The inverse of the equilibrium constant gives the partial pressure where half of the adsorption sites are occupied.

Since the coverage describes the availability of carbon feedstock on the surface of the nanoparticle the rate of carbon atoms dissolving into the catalyst nanoparticle, $N_{\mathrm{C,NP}}$, is thus related to the coverage of acetylene molecules and is given by

$$N_{\mathrm{C,NP}} = F \cdot \Theta = F \cdot \frac{K \cdot p}{1 + K \cdot p} \tag{4.7}$$

where F is proportional to the number of reaction sites at zero coverage and the dissolution-rate. $N_{\mathrm{C,NP}}$ is plotted in figure 4.11 as a solid line, assuming $F = 7.7 \cdot 10^6$ s^{-1} and $K = 0.05$ mBar^{-1}. Synthesis of CNTs can be considered to be a steady-state process, i.e. at conditions giving a constant growth-rate,

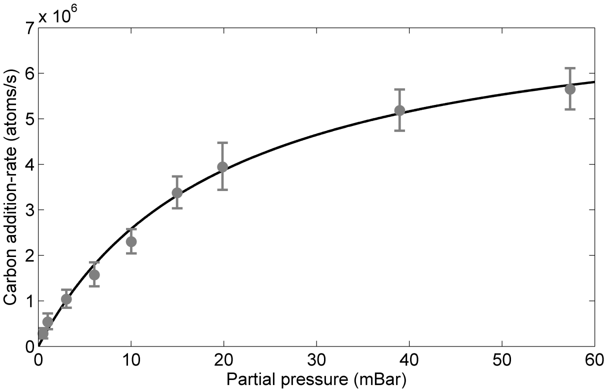

Figure 4.11: The addition-rate of carbon to the CNTs grown at different flow-rates of acetylene. Circles represent calculated data from measurements of ρ and N_{W} while solid line represents modelled data.

the rate of carbon atoms added to the catalyst nanoparticle equals the rate of carbon atoms added to the CNT. From figure 4.11 it can be seen that $N_{\mathrm{C,NP}}$ can be fitted well to the value of $N_{\mathrm{C,CNT}}$ from measurements.

Based on this it seems that $N_{\mathrm{C,NP}}$ is the limiting factor for the carbon addition-rate to the nanotube. Hence the addition-rate of carbon to the nanotubes is not limited by diffusion through the nanoparticle, at least not at the conditions of synthesis used in this experiment, but instead by carbon dissolution into the catalyst nanoparticle from the carbon feedstock.

Previously it has been observed that the growth-rate of CNTs increased linearly with acetylene partial pressure both in atmospheric CVD [104] and in low pressure CVD up to 6 mBar [105]. It was noted that the rate-limiting reaction seemed to depend linearly on partial pressure of acetylene [104]. This is similar to our findings for the same range of partial pressures.

It has been proposed that the number of walls, N_{W}, depends linearly on $N_{C,CNT}$ [93]. This trend is supported by our experimental data in figure 4.10a where N_{W} increases with increasing flow-rate of acetylene, thus increasing carbon addition-rate. However the relation does not seem to be linear.

In figure 4.10a the solid line represents a model with the number of walls being proportional to $\sqrt[6]{N_{\mathrm{C,NP}}}$. However the physical understanding behind that model is not complete, but could possibly be related to the molten layer on the surface of the catalyst suggested to control the number of walls [91]. When the concentration of carbon in iron increases the melting temperature decreases [106], thus the thickness of the layer of molten surface atoms increases.

Even though there is no complete understanding behind the results presented in figure 4.10a they can still be used to control the average number of walls of the grown nanotubes by controlling the partial pressure of acetylene. This can be useful for applications since for example the electrical and mechanical properties of CNTs vary with the number of walls [107].

4.4.3 Area of catalyst

Laser absorption measurements during flow synthesis, shown in figure 4.12a, reveal that initially the growth-rate gradually increases relatively slowly. Due to fluid dynamics and diffusion the gas front is smeared out and the partial pressure of acetylene will gradually increase to the nominal value, which causes the gradual increase in growth-rate. Within 60 seconds the height of the VANTA increases at a constant rate and is expected to continue at that rate until growth ceases.

In burst synthesis the growth-rate increases faster to a higher rate due to the initial burst of acetylene. The higher growth-rate is explained by the higher partial pressure experienced by the substrate while the burst lasts. Although the MFC reacts to the burst and adjusts the flow to the set value in less than 10 seconds the period of faster growth-rate lasts for more than 30 seconds, probably due to fluid dynamics and diffusion smearing out the burst.

Eventually the partial pressure will be reduced to the nominal value, which can be seen as the growth-rate being reduced. Since the process conditions remain constant during the continued synthesis it is expected that growth continues at the reduced rate until it is terminated by catalyst poisoning.

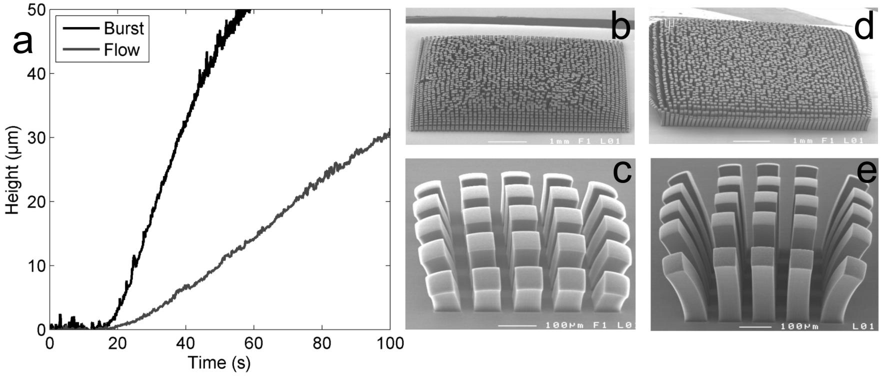

Figure 4.12: Flow- respectively burst-synthesis at 700 °C and set flow-rates of 6 sccm acetylene. (a) Laser absorption measurements of initial kinetics. (b-e) SEM images of VANTAs grown using burst-synthesis (b and c) respectively flow-synthesis (d and e). The patterns of the catalyst are 5.0 mm arrays with scale-bars 1 mm (b and d) and 0.5 mm arrays with scale-bars 100 μm (c and e).

In images of VANTAs formed in burst- respectively flow synthesis, shown in figure 4.12b-d, the differences are seen. In burst synthesis the terminal lengths of the pillars depend on where in the pattern the pillar is situated.

At the edge the length of the CNTs is shorter than in the middle, as seen in figure 4.12b and c. VANTAs formed by flow synthesis have a relatively equal height of pillars across the sample, figure 4.12d and e.

In burst synthesis for samples with small areas of catalyst, the height of a pillar in the middle is shorter than for samples with large areas of catalyst, since they are closer to the edge. In flow synthesis only the outermost pillars reveal an edge effect, causing bending of the pillars due to shorter CNTs closest to the edge, while the height of a pillar is similar for patterns of different size.

Burst synthesis of carbon nanotubes shows a dependence between length of the nanotubes and the area of patterned catalyst. Systematic experiments on different areas have been carried out in Paper II. The observations that catalyst areas on the millimeter-scale affect the structure of nanotubes on the nanometer-scale was explained and a model to describing the process was discussed.

Experimental methods

Catalyst areas of 1 nm iron on 10 nm alumina were patterned on oxidized silicon. The catalyst pattern consisted of 70 μm wide squares separated by 30 μm which were repeated for different number of times. 5 repetitions in each direction gave an array of squares with a 0.5 mm array side-length, 10 repetitions gave an array with 1.0 mm side-length and so on. Arrays with 5.0 respectively 0.5 mm side-length are shown in figure 4.12b and c.

Vertically aligned nanotubes were grown simultaneously, i.e. in the same growth-run, on the substrates. Burst synthesis was executed at different temperatures at a set flow-rate of 3 sccm acetylene for a growth-time of 15 minutes, details can be found in appendix A.

The heights of the vertically aligned nanotube arrays were measured by SEM on the silicon-substrates. The nanotubes were transferred to standard TEM-grids to study the microstructure of the CNTs by transmission electron microscopy.

Results and Discussion

The lengths of the CNTs in pillars situated close to the center of the pattern at different temperatures and for different pattern side-lengths were measured and plotted in figure 4.13a. The temperature dependencies of the CNT lengths show an optimal temperature of 725 °C. The optimal temperature was, within the experimental resolution, the same for the different catalyst areas.

At the same temperature, the length of the CNTs increased with increasing area of catalyst pattern. This was seen for all temperatures, although VANTAs were not grown on substrates with smaller area of catalyst in some cases. For 3.0 mm array side-length or longer, VANTAs were grown at temperatures down to 625 °C. As the side-length decreases the interval of temperatures

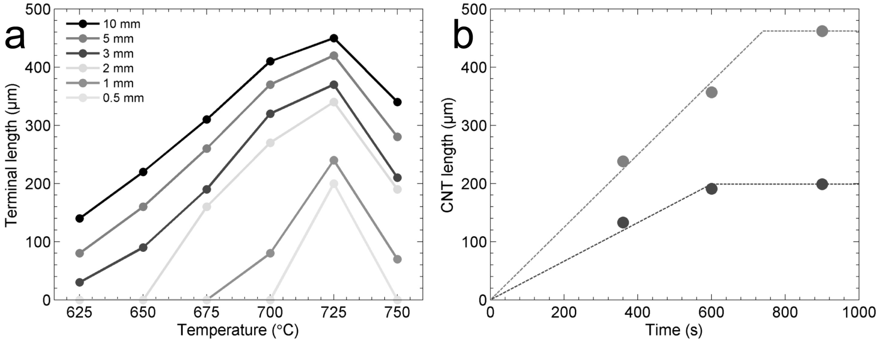

Figure 4.13: (a) Terminal length of CNTs grown in burst-synthesis at different temperatures and on substrates with arrays of catalyst with different width. (b) Height of VANTAs grown at 725 °C as a function of growth-time for samples with catalyst pattern of 5.0 (gray) and 1.0 mm (dark-gray) width respectively.

where VANTAs can be formed was reduced.

Kinetics of the synthesis was studied by stopping the synthesis-step, by closing the gas valve, at different times. The heights of VANTAs formed are plotted in figure 4.13b together with solid lines fitted to measurements according to the assumption that growth occurs at a constant rate until it is terminated by poisoning. The actual time of growth is lower than the time of the synthesis-step, thus the lengths presented in figure 4.13a can be considered to be the terminal length of the CNTs.

By comparing kinetics it can first be noted again that the terminal length is smaller for smaller areas of catalyst. It is also seen that the growth-rate is slower, approximately 0.3 μm/s for a 1.0 mm array side-length compared to 0.6 μm/s for 5.0 mm.

The microstructures of the CNTs grown under different conditions were examined using TEM. Micrographs, examples shown in figure 4.14a and b, revealed that the average number of walls varied with area of catalyst. It was found that the number of walls in the carbon nanotubes increased with decreasing area of catalyst. The temperature dependence was weak, showing a slightly decrease in the number of walls with increasing temperature. The latter is in contrast with results previously presented where the number of walls had a stronger dependence on temperature of synthesis [91].
At the same temperature the terminal length increases and number of walls decreases as the side-length of the catalyst array increases, which is shown for samples grown at 725 °C in figure 4.14c. However the average amount of carbon atoms deposited in the carbon nanotubes, proportional to the length multiplied by the number of walls, is within the experimental error-bars the same at each temperature. The amount of carbon deposited is different at

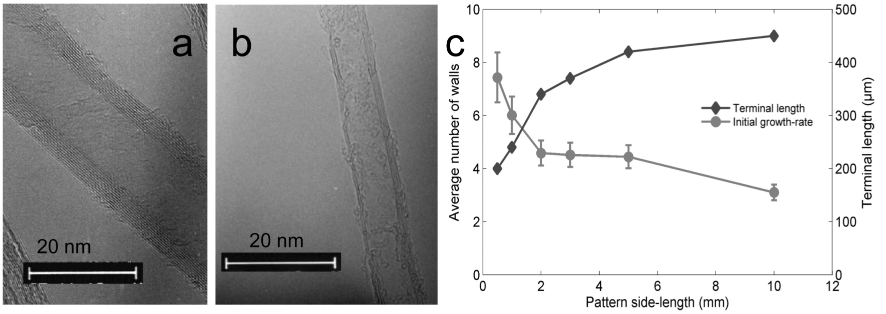

Figure 4.14: (a and b) TEM-images of CNTs grown on substrates with arrays of catalyst with 0.5 mm width (a) respectively 5 mm width (b). (c) Measurements of average number of walls (circles) and terminal lengths (diamonds) for catalyst patterns with different width. Samples were grown at 725 °C

different temperatures of synthesis though.

The main difference in process conditions between burst synthesis and flow synthesis is that, in the former, initially the partial pressure of acetylene has a peak. In flow synthesis, where no peak in partial pressure is observed, the terminal length is not strongly dependent on patterned area of catalyst. Thus the key to understand the dependence on catalyst pattern might be found in the initial burst of acetylene.

During etching of a material by gaseous species the etching-rate might vary with the pattern of the material to be etched. This is called micro-loading and is due to the transport of the reacting species to and from the reaction site being limited by diffusion. In the semiconductor industry micro-loading during dry etching is well known [108]. Similar effects have also been seen earlier in synthesis of carbon nanotubes [92].

In the process of carbon nanotube growth, acetylene molecules are consumed at the catalysts, leading to lower partial pressure locally in a volume close to catalyst areas. Acetylene molecules will then diffuse from nearby volumes with higher partial pressure to the depleted volume. Depletion continues at a steady rate, due to acetylene being decomposed into CNTs. Thus the local partial pressure will be lower than, and determined by, the rate of diffusion from neighboring, non-depleted volumes, as schematically shown in figure 4.15a.

The rate of diffusion depends on the area between the depleted volume and nearby non-depleted regions. Consider the two-dimensional model, shown in figure 4.15b, where a 5 by 5 array of regions has a 3 by 3 array of regions with catalyst in the middle. There are 3 types of regions with catalyst. Region A is situated in the middle of the array, region B on the edge and region C on the corner. During synthesis acetylene is equally depleted in all regions

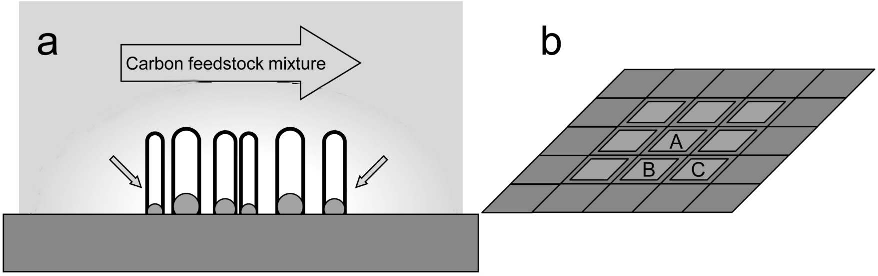

Figure 4.15: (a) Schematic image on acetylene depletion at areas of catalyst and diffusion from neighboring areas. (b) Model of a substrate with 5 by 5 areas, of which the middle 3 by 3 array are areas of catalyst.

with catalyst, which leads to diffusion of acetylene from nearby non-depleted regions.

When comparing the different regions the numbers of nearby non-depleted regions, and thus the rate of acetylene diffusion, are different. Region C has 5 non-depleted neighboring regions without catalyst, region B has 3 and region A has none. This leads to region A having a lower partial pressure of acetylene than region B, which has a lower partial pressure than region C.

This model can be used to understand the effects of patterned catalyst area on grown carbon nanotubes. For substrates with smaller area of catalyst the non-depleted regions are closer to the middle of the pattern, thus the local partial pressure of acetylene is higher. For substrates with larger area of catalyst the non-depleted regions are more distant to the middle of the pattern, thus the local partial pressure of acetylene is lower.

The reason for observing this in burst synthesis but not in flow synthesis must be that the length-scale, where diffusion is the dominating mechanism for acetylene transport to the catalyst, is increased. This is due to the diffusion-rate being proportional to differences in concentrations, which are very large during the burst since the high partial pressure gives a high rate of depletion. Possibly pattern dependence could be obtained also in flow synthesis if partial pressures as high as during the burst were used.

From the results of synthesis at different flow-rates of acetylene it was known that higher partial pressure gave carbon nanotubes growing at a faster rate but for a shorter time and with more walls, compared to a lower partial pressure. Hence this could be expected also for substrates with smaller catalyst area, compared to larger.

However the burst of acetylene, giving the pattern dependence on local partial pressure, only lasted for a few seconds and then process conditions became similar to flow synthesis. Still those initial conditions influenced the structure of the carbon nanotubes formed during the continued synthesis.

The number of walls of the carbon nanotubes formed in the initial burst was expected to be larger for smaller catalyst area, due to the higher local partial pressure. This was also seen experimentally in figure 4.14c. The experimental values though were obtained at random positions along the CNTs, i.e. not only at the part of CNTs formed during initial burst. Thus the initially formed microstructure of CNTs was kept during the continued synthesis although the process conditions changed.

After the nominal partial pressure of flow synthesis has been reached, after the initial peak, the addition-rate of carbon to the CNTs was the same regardless of pattern size. However the growth-rate varied since carbon nanotubes with larger number of walls required more carbon atoms per μm of CNT, thus had a slower growth-rate at the same rate of carbon addition as seen in figure 4.13b.

Still the total amount of deposited carbon was found to be similar for different patterns at the same temperature which could also be expected since both carbon addition-rate and poisoning-rate were similar during the main part of the synthesis. Thus all observed trends can be explained by the initial difference in local partial pressure followed by conditions of flow synthesis.

An interesting implication of the observation that the initial microstructure of carbon nanotubes is kept during continued growth is that the synthesis-step could be divided into two parts. In the first part conditions are chosen to obtain the desired number of walls. During the second part, conditions are chosen to give the optimal length of the carbon nanotubes. Thus the microstructure and length of carbon nanotubes could be independently selected.

4.5 Conclusions

It has been described how the kinetics of synthesis is related to the microscopic processes involved in growth of carbon nanotubes. The results can be used to obtain a deeper understanding of the processes involved in synthesis of carbon nanotubes.

The partial pressure of acetylene has an effect on the synthesis of carbon nanotubes. In flow-synthesis it has been shown that the coverage of acetylene on the nanoparticle, and thus the rate of carbon dissolution, follows a Langmuir adsorption isotherm. It has also been shown that the average number of walls increases and that the time of growth decreases with increasing partial pressure of acetylene.

In burst-synthesis the macroscopic pattern of the catalyst areas influenced the microscopic properties of the carbon nanotubes. Carbon nanotubes grown on substrates with larger areas of catalyst have a larger terminal length, but with a similar amount of carbon atoms since they had fewer number of walls. The differences have been explained by depletion of the carbon feedstock during the initial burst.

Chapter 5

Varactors based on CNTs

An important motivation for studies on synthesis is the possibility to use the results in applications. The mechanical properties of graphene and carbon nanotubes have been suggested to have applications in high-strength and light-weight materials [109]. The electrical properties are useful in electronic circuits, where the tunable range of electrical properties enable many different applications [110].

In nano electro-mechanical systems (NEMS) both the mechanical and the electrical properties are used [111]. The high stiffness and low density combined with high electrical conductivity, makes carbon nanotubes and graphene promising materials e.g. for tunable radio-frequency resonators [112].

5.1 Introduction

Another example of a NEMS is a varactor based on carbon nanotubes. A varactor is a capacitor with a variable value of its capacitance. The value of the capacitance can be varied either mechanically or electrically. Varactors can be found in LC-circuits, where they are used to tune the resonance frequency of the circuit. An example of where varactors are found is in radio receivers, which can be tuned in to radio-stations broadcasting at different frequencies.

Previously a varactor based on electrostatic deflection of carbon nanotubes was proposed [113]. The idea was to use two free-standing vertically aligned metallic carbon nanotubes positioned next to each other, as shown in figure 5.1a. Since the nanotubes are conducting, a difference in voltage will lead to accumulation of positive respectively negative charges in the tubes.

The charges of different sign will attract each other, giving rise to an electrostatic force that deflect the carbon nanotubes, as seen in figure 5.1b. The amount of deflection will depend on the strength of the electrostatic force and the mechanical stability of the nanotubes.

The capacitance between the nanotubes depends on the distance between

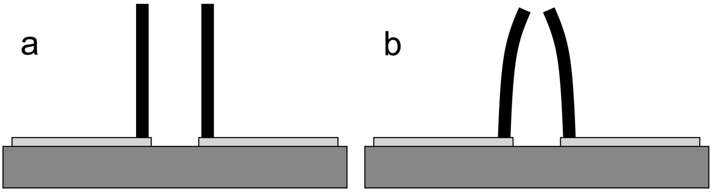

Figure 5.1: (a) Vertically aligned nanotubes on two electrodes on a substrate with no voltage difference applied between the electrodes. (b) Deflected nanotubes due to the applied voltage difference giving rise to electrostatical forces.

them. The capacitance between two parallel plates is given by

$$C = \varepsilon \cdot \frac{A}{d}, \tag{5.1}$$

where ε is the dielectric constant of the medium between the plates, A is the area of the plates and d is the distance between the plates. Thus, deflection of the nanotubes towards each other will increase the capacitance. The value of the capacitance between the CNTs can therefore be changed by varying their deflection, which is controlled by the difference in applied voltage.

Theoretical and experimental studies of electrostatic deflection have been carried out on similar structures [114]. The results show that the deflection not only increases with increasing voltage difference, but also the change in deflection per change in voltage increases with increasing voltage difference. The nanotubes can be deflected to $\frac{2}{3}$ of the initial distance before they suddenly collapse into each other at the pull-in voltage.

This collapse has been used to form electromechanical switches from individual vertically-aligned carbon nanofibers [115]. By coating the nanofibers with an insulating material, similar devices have been shown to act as a memory cell [116]. In order to have reversible switching nanotubes have to be short [115], making it difficult to characterize the electrical properties of the individual devices due to their low value of capacitance.

Single carbon nanotubes can be actuate, i.e. deflected, by applying electrostatic forces [117]. For vertically aligned nanotube arrays the situation is more complicated since the electrostatic forces act not on a uniform object but on a wall of nanotubes held together by Van der Waals-forces. It is not obvious if the electrostatic forces will lead to deflection of the nanotube arrays as a whole or if individual nanotubes will be pulled out of the arrays.

Here we suggest that the two individual nanotubes, discussed above, are replaced by two walls of vertically aligned nanotubes arrays. The same principles for changing the capacitance between the arrays of CNTs would still apply. The advantages of the proposed device are that optical and electric characterization is facilitated and that the absolute value of the capacitance

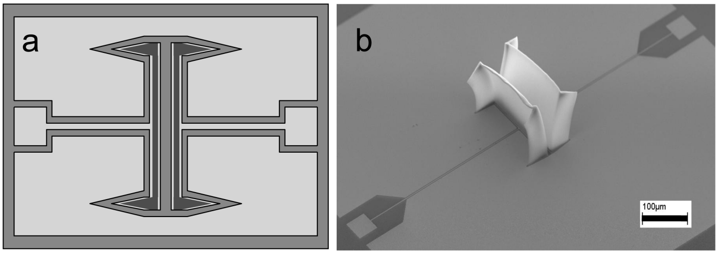

Figure 5.2: (a) Schematic layout of the two T-shaped electrodes surrounded by shield electrodes (light-gray), with catalyst material (black), on the substrate (dark-gray). (b) SEM-image of the fabricated device. Scale-bar is 100 μm.

can be made larger. A potential drawback is that the size of the device becomes larger. For a more thorough description the reader is referred to Paper III.

5.2 Experimental methods

The fabrication of a varactor based on VANTAs requires patterning of conducting electrodes, patterning of catalyst area on top on the electrodes and synthesis of vertically aligned nanotubes from the areas of catalyst. In fabrication, where many processing-steps are needed, it is important to have steps that are compatible with each other.

Sputtered molybdenum was chosen as the electrode material. Molybdenum is a refractory metal with a melting temperature above 2600 °C, making it compatible with conditions of synthesis. The compatibility with synthesis is important both for the possibility to grow carbon nanotubes on the electrodes and for having low-resistivity electrodes that can endure the harsh conditions of synthesis. The latter led to the choice of sputtered molybdenum, measured to have 8 times lower resistivity than evaporated molybdenum after the nanotube synthesis step.

The electrodes were T-shaped and surrounded by shield electrodes, as seen in figure 5.2a, to improve electrical measurements. The width of the array of nanotubes should be wide enough to give a detectable value of capacitance that is larger than the parasitic capacitances. To reduce the latter a high-resistivity substrate material was selected. In addition, the T-electrodes were made relatively long and thin before ending at the contact pads to reduce parasitic capacitances.

The pattern of catalyst material, 5 nm alumina and 1 nm iron, was aligned to the electrodes. Thin nanotube walls are desired to ensure low actuation voltages. However, as seen in Paper II, the stability can be too low for the VANTAs to support themselves. Hence the catalyst pattern was given a U-shape to increase mechanical stability. Flow synthesis was done at 700 °C having a flow-rate of 5 sccm acetylene for 150 seconds, i.e. the synthesis was stopped before the catalyst was poisoned.

5.3 Results and discussion

The vertically aligned nanotubes, grown in this study, had a height of 135 μm ± 5 μm. In general, the two walls of nanotubes leant away from each other, which can be seen in figure 5.2b. The reason for arrays not being perfectly vertical could be that the process conditions varied slightly across the area of catalyst during synthesis, as discussed in Paper II. However, nanotubes leaning away from each other are more preferable than nanotubes leaning towards each other and thus short-circuiting the device.

5.3.1 Electrostatical actuation

Experiments performed in an optical microscope show *in situ* that the walls of vertically aligned nanotube arrays are deflected as a whole during electrostatic actuation. When an actuation voltage is applied the distance between the walls decreases, as shown in figure 5.3. Apparently the Van der Waals-forces holding the nanotubes together in the array are stronger than the electrostatic forces acting on the individual carbon nanotubes.

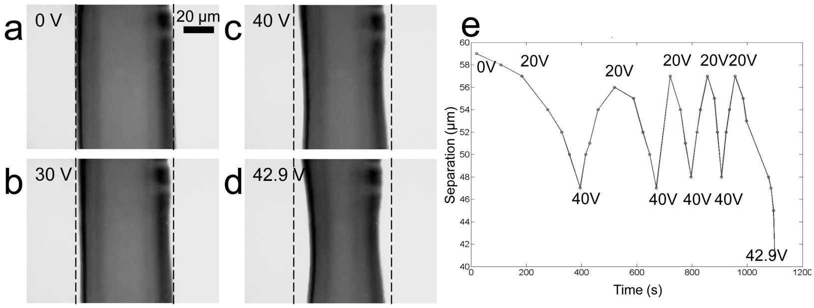

Figure 5.3: (a-d) Images from optical microscope of CNT-walls at an applied actuation voltage of 0 V, 30 V, 40 V and 42.9 V. Scale-bar is 20 μm and striped lines are added to aid the eye. (e) Separation of the top of the CNT-walls at different actuation voltages at different times.

The amount of deflection depended on the applied actuation voltage, since higher voltage differences give larger electrostatical forces. The distance between the walls of nanotubes could be controlled reproducibly when cycling the actuation voltage back and forth, as seen in figure 5.3e. Reproducibility is an important requirement to enable applications.

In situ actuation of walls of nanotubes was performed in a scanning electron microscope to study the process with better resolution and depth of focus. The series of images in figure 5.4a-d show the decrease in separation between the walls with increasing actuation voltage. It can also be noted that the brightness of the walls changes with applied voltage. The lower wall, to which a positive voltage was applied, becomes darker since it is harder for the negative secondary electrons studied in SEM to escape from the nanotubes at a positive potential [118].

The separation between the walls shows a similar dependence on actuation voltage for devices studied in the optical microscope and in the SEM, as seen in figure 5.4e. The change in deflection increases faster per voltage increase at higher actuation voltages. When the separation is reduced by roughly 30 % of the initial value the pull-in voltage is reached and the walls collapse into each other, similar to results from individual nanotubes [114].

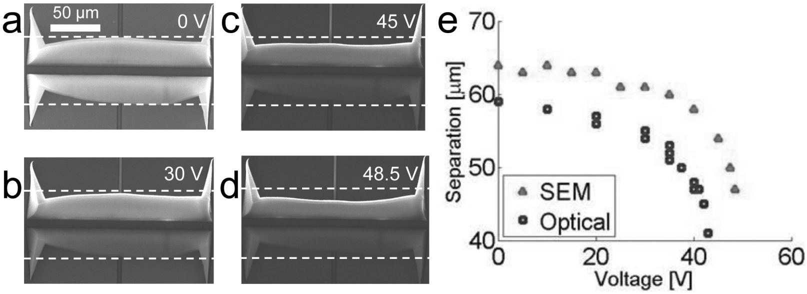

Figure 5.4: (a-d) SEM-images of CNT-walls at an applied actuation voltage of 0 V (a), 30 V (b), 45 (V) and 48.5 V (d). (e) Separation between CNT-walls versus applied actuation voltages for devices studied in optical microscope and SEM.

The device characterized in SEM required a higher actuation voltage to decrease the separation. This observation is explained by the larger initial separation, requiring a larger voltage difference to give the same electrostatic force acting on the walls. However the relative change in separation is similar just before reaching the pull-in voltage.

The walls of carbon nanotubes are very porous. An areal density of 10^{10} nanotubes per cm^2 was determined by weighing a substrate covered with VANTAs grown under similar conditions before and after removal of the nanotubes. This corresponds to a density of 10 kg per m^{-3} and a porosity of >95 %. Even for such high porosities, each wall moves as a single cohesive unit.

The effective Young's modulus of the VANTAs was found to be 6 ± 4 MPa by comparing the observed deflection with simulations based on conducting walls with the same geometry. The uncertainty comes from the difficulty of accurately defining the initial geometry due to the outwards bending of the walls. For a comparison, that is ten times lower than the typical Young's modulus for rubber.

Although individual MWNTs have been found to have tensile strengths of 900 GPa [119] the obtained effective Young's modulus is in the same range as what has been measured for compression of VANTAs [120]. It therefore seems reasonable that the collective bending observed here is not due to stretching along the length of the tubes but compression of the wiggly tubes, similar to spring-coils.

5.3.2 Electrical measurements

The ability to control the distance between two walls of vertically aligned nanotubes by the actuation voltage makes for experimental realization of a varactor based on carbon nanotubes. To measure the capacitance between the walls, a parameter analyzer coupled to a probe-station enabling electrical characterization at radio frequencies was used.

During electrical measurements the shield-electrodes were grounded, actuation was done by applying a DC-bias voltage and a small AC-signal was used to measure the scatter parameters of the device. A model of an equivalent circuit was set up to obtain the capacitance between the nanotube walls. The measured values were compared to simulated values at different frequencies, see figure 5.5a. The value of the capacitance between the walls of carbon nanotubes was 22 fF, for the device in figure 5.5b, at zero actuation voltage.

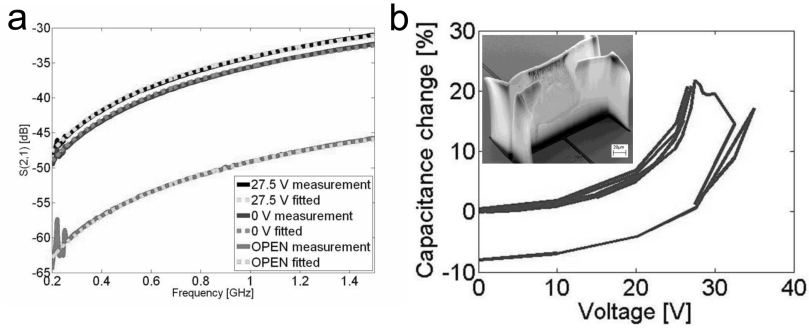

Figure 5.5: (a) Values of S12-parameter at different frequencies. Measured and simulated values for two different actuation voltages are shown. (b) The change in capacitance from its initial value when the actuation voltage vas cycled back and forth. The inset show a SEM-image of the device after measurements. Scale-bar is 20 μm.

The actuation voltage could be used to control the value of capacitance between CNT-walls. Increasing the actuation voltage decreased the distance between the walls and thus increased C_{CNT}. As expected from the deflection seen in optical characterization, the value of C_{CNT} could be reproducibly controlled when the actuation voltage was cycled back and forth, as seen in figure 5.5b. The change in capacitance was more than 20 %.

From equation 5.1 it could be expected that a change of 30 % in wall separation, as detected in the microscope, would give a change of 50 % in capacitance. However the deflection is measured at the middle point of the top of the wall, which is deflected most. The capacitance on the other hand is measured for the complete structure, which explains a value lower than obtained by directly using the change in deflection in the equation.

The change in capacitance was only reproducible as long as the actuation voltage was kept below a certain limit, in this case 27.5 V. When the limit was surpassed, the capacitance decreased and when the actuation voltage was reduced back to 0 V the capacitance between the walls was lower than its initial value.

This observation can be understood after studying the device in an SEM. The carbon nanotubes at the top of the middle region of one of the walls were missing after measurements, as seen in the inset of figure 5.5. It is expected that when the actuation voltage reaches the pull-in voltage, slightly above 27.5 V, the walls come into contact. Most of the MWNTs are highly conducting and thus the voltage difference will give rise to a large current, which will burn off the nanotubes that come into contact with the other wall.

5.4 Conclusions

A varactor based on vertically aligned nanotubes was proposed, fabricated and characterized. It was shown that VANTAs could be deflected as a whole by electrostatic forces. Devices characterized *in situ* by optical microscopy and SEM, have shown that the separation between CNT-walls could be reduced by more than 30 %. Comparison with simulations was used to determine an effective Young's modulus of 6 ± 4 MPa. Electrical characterization has shown that the capacitance of the device could be reproducibly changed by more than 20 %.

Improvements of this type of device have since been made by another group by refining the geometry of the walls and modifying synthesis to form walls with better vertical alignment [121]. In their studies, the current flow was limited to a low enough value to avoid burning of CNTs upon pull-in. It can be expected that further improvements in design will lead to varactors with lower actuation voltages and increased reproducibility from device to device.

By coating the VANTAs with an insulating material, similar to what has been done for the individual nanofiber devices [116], it should be possible to avoid burning upon pull-in and also increase the effective Young's modulus. This could also be achieved by filling the VANTAs with polymer after synthesis. Then insulating polymer could be used for varactors and conducting polymers could be used for switches.

Chapter 6

Bending rigidity of graphene

Being only a single layer of atoms thick, graphene seems to behave very differently from objects we are used to. However, continuum mechanics has been shown to describe its motion well [62]. This implies that the same models that describe deformations in e.g. plates of steel can also be used for graphene, but also requires the material parameters such as the Young's modulus and the bending rigidity, to be known.

6.1 Introduction

As described earlier in this thesis, the discovery of graphene seems to defy previous theories about the instability of two-dimensional crystals. However, graphene was shown to be stabilized by the support from the substrate or by forming ripples when suspended. Experimentally, corrugation lengths on the order of 10 nm and heights on the order of 1 nm at room temperature have been found [15].

The possibility to form ripples is due to fluctuations in electron density in graphene [122]. In the ground state all bonds are conjugated, then the preferred topography of graphene is flat. However at finite temperatures there is a large probability of having asymmetric distribution of electron density, which leads to longer and shorter bonds, creating ripples.

Changes of bond length with temperature are also the reason for the negative thermal expansion coefficient (TEC) in graphene [122]. Experimentally graphene has been found to have a negative thermal expansion coefficient, α_{gra}, in a broad range of temperatures [123][124].

The length-scale of ripples depends on the temperature and the value of the bending rigidity, κ, since formation of corrugation requires thermal energy to overcome the energy cost to add curvature to the graphene [122]. However, reliable experimental measurements of the bending rigidity of graphene are lacking.

The classical expression for a homogenous and isotropic thin plate gives the relationship $\kappa \sim Eh^3$, where E is the Young's modulus and h is the thickness of the plate. The linear dependance with E comes from the Kirchhoff hypothesis that assumes linear variation in strain and stress along the thickness of the plate. Nano-indentation in AFM has been used to show that this relation is valid for flakes of graphene with 8 or more layers [125].

For a single atomic plane of graphene it is not reasonable to define thickness, and even less to assume the Kirchhoff hypothesis to be valid. Instead, the proposed origin of the bending rigidity in graphene is due to the effects on bond angles and dihedral angles, i.e. the angles between second respectively third nearest neighbor atoms, upon bending [126]. Calculations then give a bending rigidity of 1.4 eV, which is close to $\kappa = 1.5$ eV obtained from *ab initio* calculations [127] and $\kappa = 1.2$ eV derived from the phonon spectrum of graphite [128].

The bending rigidity of bilayered graphene, κ_{bi}, depends on the interaction between the layers. Assuming that the layers are completely free to slide against each other, then $\kappa_{\mathrm{bi}} = 2\kappa \approx 3$ eV [129]. Instead, assuming that the layers can not slip on each other at all, i.e. using Kirchhoff's hypothesis, calculations give $\kappa_{\mathrm{bi}} = 180$ eV [130]. The large spread in values motivates the need for experimental determination of the bending rigidity in bilayered graphene.

During thermal cycling it has been observed that the mismatch in TECs between graphene and the substrate can lead to buckling in suspended graphene [123] and compressive strain in graphene supported on oxidized silicon [131]. Graphene with compressive strain has been observed to form buckled resonators when suspended, which was thought to change their mechanical properties [132].

Since the formed strain is due to a forced change in atomic positions from equilibrium it will influence the crystal vibrations. Hence Raman spectroscopy can be used to measure strain in graphene. Strain has been shown to shift the position of the G- and 2D-peaks [37].

In Paper IV the formation of compressive strain in graphene on silicon oxide after thermal cycling, as measured by Raman spectroscopy, is reported. The formed strain was used control the buckling of suspended beams. It was predicted that buckled beams should experience snap-through under electrostatic pressure.

Atomic force microscopy was performed during electrostatic actuation to study the deflection of suspended graphene. Curved beams were found to experience buckling instability during actuation. Measurements of the critical actuation voltage were carried out to determine the bending rigidity of bilayered graphene to 35^{+20}_{-15} eV.

6.2 Experimental methods

The steps involved in the fabrication of the suspended samples are described in figure 6.1a-h. Figure 6.1i shows an image from atomic force microscopy of two suspended beams while figure 6.1j shows a scanning electron microscopy image of a double-clamped beam. In short these devices were made by first patterning the graphene beams, followed by deposition of electrodes and etching of the substrate [43].

Graphene was deposited on silicon substrates with 300 nm oxide using mechanical exfoliation, the scotch-tape method. The thickness of the oxide was chosen to optimize the contrast of few-layered graphene in an optical microscope, which was used for finding the location of flakes with respect to pre-fabricated alignment marks, figure 6.1a.

The substrates were annealed at 300 °C in argon and hydrogen before exfoliation to remove possible contamination. Flakes with suitable shapes and number of layers were selected for further processing. The number of layers was determined by the optical contrast using a LabView-program for image-processing and confirmed by Raman spectroscopy on selected samples.

Mono- and bilayered graphene flakes were shaped into beams using electron-beam lithography. Positive resist PMMA was used. After spin-coating, the resist was baked at 160 °C to remove solvents. To obtain beams of graphene covered by resist mask every part of a 100 μm square was exposed, with the exception of the area where beams were to be patterned, figure 6.1b.

An oxygen-plasma, nominally removing 10 nm of resist, was used to etch non-masked graphene, figure 6.1c. The resist mask was removed in acetone leaving the patterned beams of graphene on top of the substrate, figure 6.1d.

A bilayer resist composed of bottom-layer copolymer MMA-MAA and top-layer PMMA was used to pattern the electrodes used to contact the graphene beams, figure 6.1e. Development of both layers of resist was done in MIBK:IPA. Bi-layer resist was used to ensure under-cut, facilitating lift-off after evaporation.

Deposition of 3 nm Cr and 150 nm Au was done using e-gun evaporation, figure 6.1f. Cr was used as adhesion layer since it withstands HF-etching. The relatively thick layer of Au was used to give mechanical stability in order to avoid deflection of the suspended part of the electrodes during electrostatic actuation. Lift-off was done with ultra-sonic agitation in hot acetone, removing deposited metal on top of the resist, figure 6.1g.

The silicon oxide was wet-etched using HF-based buffered oxide etchant (BOE) to suspend the graphene beams. During etching the electrodes act as an etch-mask. The etchant penetrates freely under the graphene beam, making it suspended by a constant distance to the substrate (225 nm) under the entire beam, also under the electrodes [53]. Rinsing was done in milli-Q and IPA. Critical point drying was used after etching to avoid surface tensions during drying, figure 6.1h.

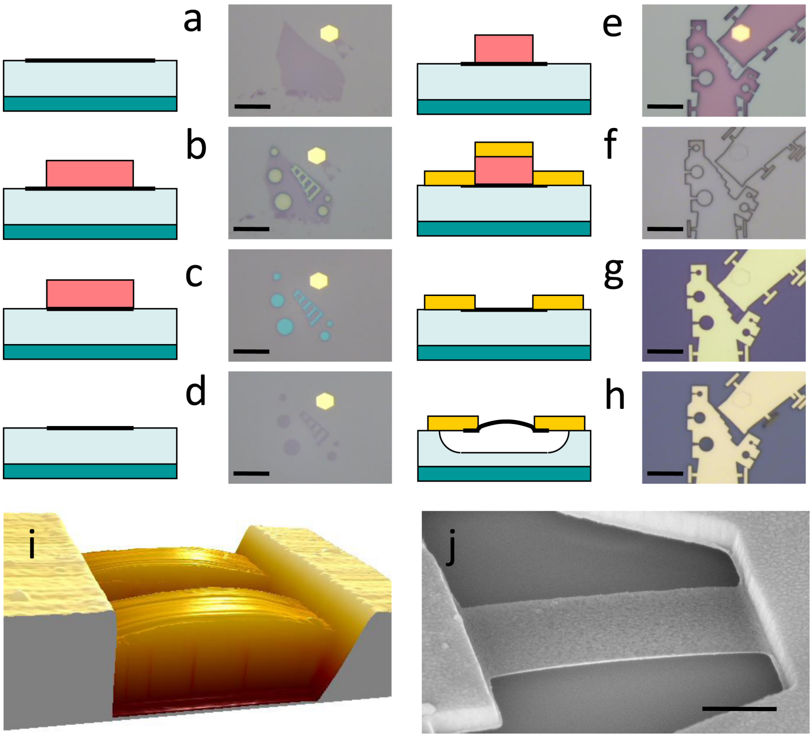

Figure 6.1: (a-h) Schematic images and images from optical microscope (scale-bars are 10 μm) of fabrication of suspended beams from graphene. (a) Deposition of graphene. (b) Resist patterning. (c) Dry etching of graphene. (d) Removal of resist. (e) Patterning of new resist. (f) Metal deposition. (g) Lift-off. (h) Wet etching of substrate underlying graphene. (i) Image from AFM of suspended bilayered graphene beams. (j) SEM-image of bilayered double-clamped beam. Scale-bar is 1 μm.

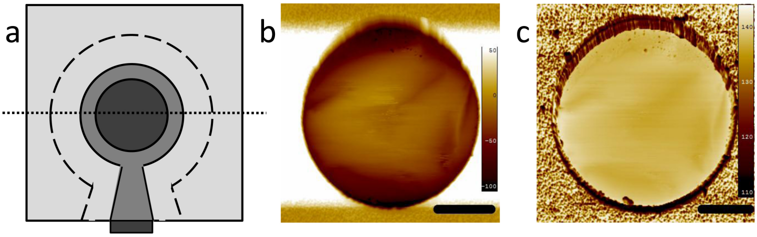

Figure 6.2: (a) Schematic image of a fully-clamped beam. (b) and (c) Height- respectively and phase-image from AFM of a suspended, bilayered fully-clamped membrane. Scale-bars are 1 μm.

To avoid excessive under-etching of electrodes, causing electrostatic actuation of them, graphene beams are formed first and the electrodes overlap with a controlled distance. For samples where electrodes were patterned first and graphene beams later the undercut of the electrode was as large as the graphene flake, leading to sagging of the electrode.

The fast under-etching of graphene was used to fabricate fully clamped membranes. The flake was patterned into beams with the shape of a frying pan. A square electrode with hole in the middle is patterned on top on the graphene, light-grey in figure 6.2a. The graphene is clamped by the electrode in the grey areas and left exposed in the dark-grey areas.

When the substrate is etched the bottom-side of the handle of the frying pan will be exposed to the etchant outside the electrode. The etchant will be able to freely penetrate under the graphene all the way underneath it and continue to under-etch the electrode, thus suspending the whole area inside striped lines in figure 6.2a. A cross-section along the dotted line looks similar to the cross-section in figure 6.1h. AFM-images of a fully clamped membrane after etching is shown in figure 6.2b and c.

Raman spectra are obtained using a Renishaw micro-Raman spectrometer with a 514 nm excitation laser and spectral resolution better than 1 cm^{-1}. Spectra are measured *in-situ* on the same position of an unsuspended graphene flake during heating from room-temperature to 200 °C followed by cooling to room-temperature.

Electrostatic actuation of the suspended graphene was done by applying a voltage, V_{bg}, to the silicon back-gate while keeping the graphene grounded. The depth of etching was chosen to have some remaining insulating $\mathrm{SiO_2}$ to avoid short-circuiting between graphene and electrodes even if one or more of the graphene beams come into physical contacting with the underlying substrate.

Similar to previous studies of multi-walled carbon nanotubes [57] and multi-layered graphene [133], electrostatic deflection was imaged in-situ using AFM. The AFM was setup in non-contact mode and measurements were done in ambient atmosphere at 22 °C. Both the graphene and AFM cantilever were grounded to reduce interaction between them.

6.3 Results and discussion

6.3.1 Strained graphene

Raman spectra of the 2D peak during thermal cycling from room-temperature to 200 °C and back are shown in figure 6.3a. The shape of the 2D peak can be fitted well by a single Lorentzian, which shows that it is monolayered graphene [134], confirming the optical contrast determination.

The position of the 2D peak is monitored during thermal cycling in figure 6.3b. During heating the peak is red-shifted and during cooling it is blue-

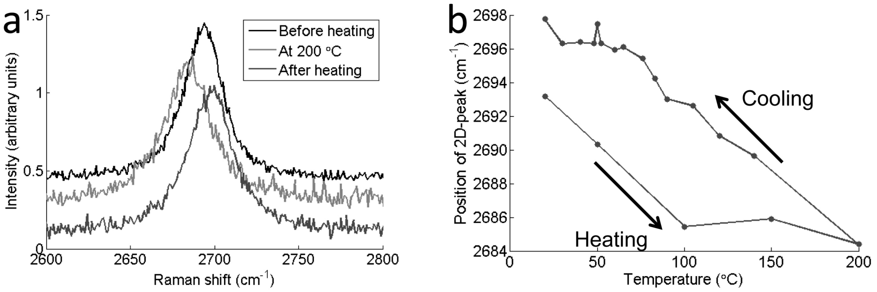

Figure 6.3: (a) Raman-spectra around the 2D-peak at different stages of thermal cycling. (b) Position of 2D-peak during thermal cycling.

shifted. The shift in frequency when cooled is 14 cm^{-1}. It can be noted that there is an initial compressive strain in the flake, probably formed during exfoliation, which is reduced when the sample is heated.

The blue-shift in frequency of the 2D peak, $\Delta\omega$, can be attributed to a formation of compressive biaxial strain, ε, of the graphene given by [37]

$$\varepsilon = \frac{\Delta\omega}{2\omega\lambda}, \tag{6.1}$$

where ω is the peak-position with no stress and λ is the Grüneisen parameter, with values of 2684 cm^{-1} and 2.7 respectively [135]. Thus the shift in the position of the 2D-line corresponds to ε=0.10 %.

The formation of compressive strain in graphene after thermal cycling can be understood using a simple model [123]. When heated, the substrate will expand due to the positive thermal expansion coefficient of silicon, α_{Si}, while the graphene with its negative α_{gra} will contract. Thus tensile strain will be created in graphene.

If the energy required for stretching the graphene, by stretching its carbon bonds, is larger than the pinning energy to the substrate graphene will slide on the substrate to reduce strain. This is why the 2D peak of graphene is not red-shifted further after reaching $T \approx 100$ °C during heating.

When cooled, the substrate contracts while graphene expands. Then compressive strain will be created in graphene, if the pinning energy is larger than the energy required for contracting graphene by reducing its bond-length. This is causing the blue-shift during cooling.

If it is assumed that there is no strain in the graphene at the maximum temperature and that the TEC of the substrate is equal to α_{Si} then the compressive strain after cooling is given by

$$\varepsilon = \Delta T \Delta\alpha = \Delta T(\alpha_{\mathrm{Si}} - \alpha_{\mathrm{gra}}), \tag{6.2}$$

where ΔT is the difference in temperature. In this interval of temperature $\alpha_{\mathrm{Si}} = 3 \cdot 10^{-6}$ K^{-1} [136] and $\alpha_{\mathrm{gra}} = -6 \cdot 10^{-6}$ K^{-1} [124], thus $\Delta T = 180$ K giving a compressive strain of $\varepsilon = 0.16$ %.

The formed strain observed in Raman measurements is slightly lower than the value calculated from the mismatch in thermal expansion coefficients. During cooling it was observed, figure 6.3b, that the 2D peak was blue-shifted at a constant rate down to 60 °C.

When further cooled the rate of blue-shift is lower. The reason could be that at large enough strain the pinning energy might be lower than the energy required for contracting the graphene, and then small ripples might be formed locally during contraction instead of increasing compressive strain [137].

6.3.2 Buckled beams

To study the effect of thermal cycling during fabrication on buckling, sample A was prepared as described above, including baking of resist at 160 °C to remove solvents. Sample B was made using conditions where the temperature of the sample was kept as close as possible to room-temperature during fabrication.

In the latter case solvents in the resist are evaporated by keeping the sample in low pressure (200 mBar) for 12 hours instead of baking at elevated temperatures. During metal-evaporation the sample is mounted on a water-cooled chuck using thermally conducting tape to improve cooling and the rate of evaporation was kept low (1 Å/s).

Before etching of the substrate the beams of graphene are imaged using AFM. In both sample A and B graphene is lying in close proximity to the flat substrate with a height of approximately 2 nm. For sample A small ripples could also be noticed before etching, possibly formed at high compressive strain. The ripples were clearly seen as bright lines in the phase-image, figure 6.4b, and found to correspond to heights on the order of one nm in the height-image, figure 6.4a. The flakes that the beams were made of were determined by optical contrast to be bi-layer graphene. This is in agreement with the measured height, although resist residues could influence step-heights obtained by AFM.

After etching, the suspended beams of graphene were imaged by AFM, figure 6.5a and c. The graphene was suspended between the electrodes above the substrate. Profiles along the beams show that in sample A they are predominantly curved away from the substrate, figure 6.5b, while in sample B they are parallel to it, figure 6.5d.

We believe that the buckling is caused by the compressive strain in the graphene. When suspended from the substrate the strain is released, leading to expansion of the graphene beam. The expansion of the beam with fixed position of the clamped edges causes it to curve. This leads to buckling in two orthogonal directions not only for fully clamped membranes but also for

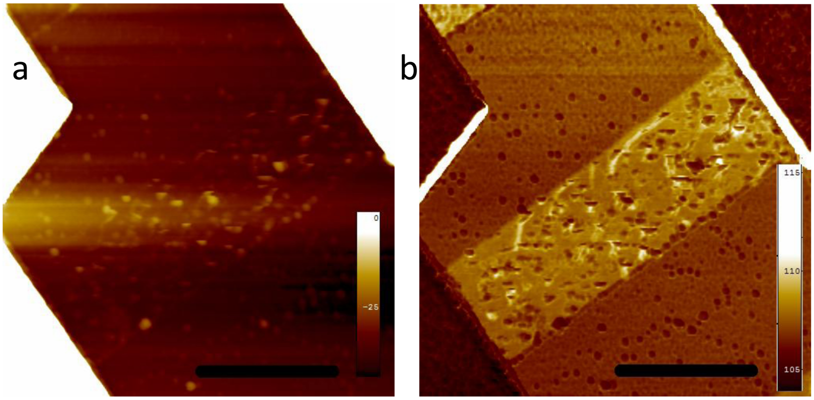

Figure 6.4: (a) and (b) Height- respectively and phase-image from AFM of a bilayered double-clamped beam before etching of silicon oxide. Scale-bars are 1 μm.

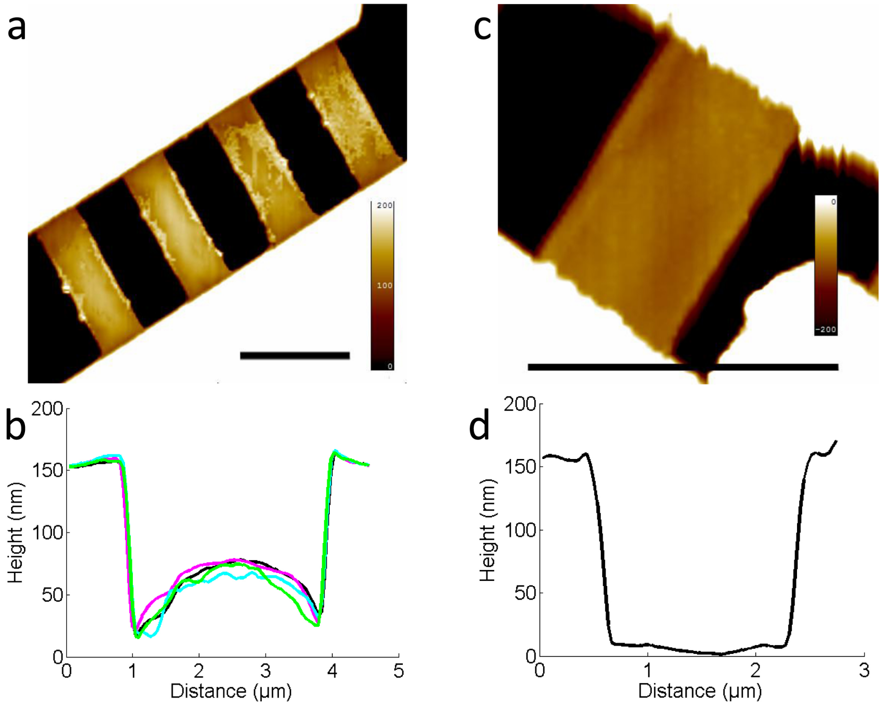

Figure 6.5: (a) and (b) AFM-image of suspended bilayered graphene beams in sample A and their profiles. Scale-bar is 2 μm. (c) and (d) AFM-image of suspended bilayered graphene beam in sample A and its profile. Scale-bar is 2 μm.

doubly-clamped beams. In the latter case, buckling perpendicular to the beam is obtained since the clamped part of the graphene can not expand [138].

The adhesion to the clamping points causes the preference of the samples to curve away from the substrate. The adhesion is however not strong enough to completely suppress the buckling. This is similar to what has been observed for graphene on top of trenches [16].

It was obtained from the profiles that the length along the beam in sample A is on average 0.12 % longer than its horizontal end-to-end-distance while for sample B it is 0.01 % longer. For sample A this is corresponds to a ΔT of 133 K according to equation 6.2, in agreement with the baking temperature of 160 °C. For sample B the elongation could be due to strain formed during exfoliation or due to a calculated ΔT of 12 K, which might have been reached on the substrate during plasma-etching of the graphene or evaporation of the electrodes.

Although the calculated compressive strain from mismatch in thermal expansion was larger than measured in Raman, possibly due to formation of ripples, it fits well with the extended length of the curved beams. This also can be understood from formation of ripples, which reduce the increase in compressive strain but still contribute to an increase in length when the beam is suspended.

During fabrication of devices contamination can be formed on the graphene. The use of polymer-based resists for patterning leave residues if not removed properly. Contamination from resist has been shown to influence the performance of devices from carbon nanotubes [65] and graphene [43].

Residues from PMMA-resist typically appear as particles tens of nanometers in diameter on the surface of the substrate [139]. Despite removal of resist in hot acetone, particles are left on top of graphene and silicon oxide before etching. The contamination is clearly visible in the phase-image, figure 6.4b, as dark spots. The spots have their counterpart in the height-image, figure 6.4a, although the topography of the sample makes the height-image less suitable for monitoring resist residues.

After etching of the silicon oxide no dark spots are seen in phase-images of doubly-clamped beams. In fully clamped membranes bands of residues can be seen close to the edge, figure 6.2c. We believe that similar to the way the etchant penetrates between graphene and silicon oxide, it also penetrates between graphene and residue-particles, making it possible to rinse away the latter. Due to the geometry, rinsing is less efficient for fully-clamped membranes than for doubly-clamped beams.

Removal of contamination on fully-clamped membranes after etching was possible by annealing in argon and hydrogen at 300 °C, showing that the observed structure is indeed due to resist residue. However, the annealing not only removed contamination but also changed the buckling of the beams, due to thermal mismatch at the elevated temperature. Hence annealing was not used for the samples presented here. But their snap-through deflection was measured and the results were consistent, within experimental error, with the values determined from the non-annealed membranes.

The curvature of the graphene beams and their deflection is suitable for studying in AFM, owing to its vertical resolution. However, the forces between tip and surface can be large enough to influence the geometry of a suspended single layer of atoms such as graphene, even in semi-contact mode [140].

The typical resonance frequencies for graphene beams are on the order of MHz [52], while the resonance frequency of the cantilever is on the order of hundred KHz. The graphene beam will thus have time to move back to minimum energy geometry before the cantilever returns during the next period of oscillation. Hence the graphene beam will always be in a stable position when the tip comes close to contact with it, and that is the position seen in AFM-images.

6.3.3 Electrostatical actuation

By applying a voltage, V_{bg}, to the back-gate while keeping the graphene grounded, an electrostatic pressure was applied to the beams. *In-situ* AFM studies during electrostatic actuation were done on initially curved devices fabricated under similar conditions to sample A.

Imaging of the beams was done at different V_{bg} and profiles along the beams were obtained from such images. Also measurements of deflection of the beams were obtained by placing the tip on a fixed position in the center of the beam and sweeping V_{bg} while measuring the deflection from initial position.

In figure 6.6 measurements from one particular bilayer device are shown. From the profiles it can be seen that during electrostatic actuation the initial upwards buckling of the graphene beam was changed to downwards buckling for V_{bg} higher than 3 V.

The deflection curve shows that for V_{bg} lower than V_{c} the beam is hardly deflected at all. At the critical voltage there is a sharp snap-through from upwards to downwards buckling where the beam deflects a large distance for a small change in V_{bg}. For this device, a deflection of 89 nm between V_{bg}=2.5 V and V_{bg}=2.7 V was observed. Similar snap-through buckling is observed for several beams and membranes.

To investigate hysteresis, imaging was done of the bilayered beams of figure 6.6 when the applied voltage on the back-gate was first increased beyond the critical snap-through voltage, V_{c} and then decreased again. The images are shown in figure 6.7. It was observed that the beams returned to the initial structure of upwards buckling when the applied voltage was removed, showing the reversibility of the switching-process. At V_{bg} =3 V, close to snap-through, the structure of the beams was similar irrespective of being approached from lower or higher V_{bg}.

As these results show, no or only very low hysteresis was observed. This is also confirmed in deflection measurements where no large shift in V_{c} is found

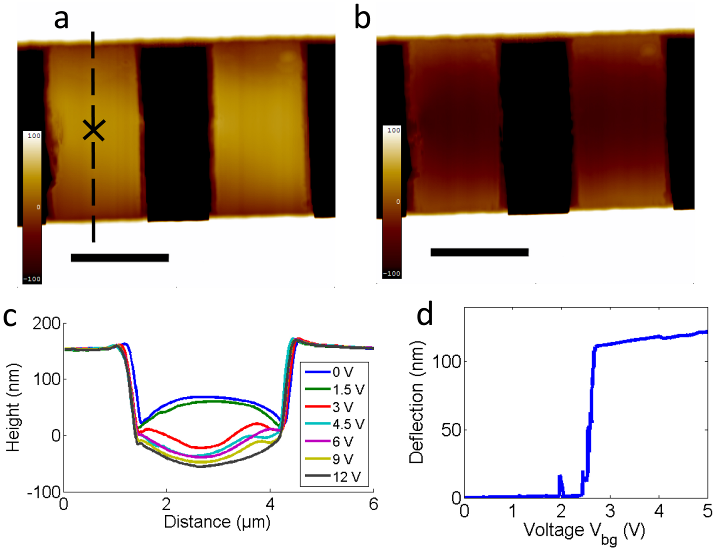

Figure 6.6: AFM-image of eleactrostatic actuation of suspended bilayered graphene beams at V_{bg}=0 V (a) and at V_{bg}=12 V. Scale-bars are 1 μm. (c) Profiles along the striped line in (a) at different V_{bg}. (d) Measurement of deflection at the position of the cross in (a).

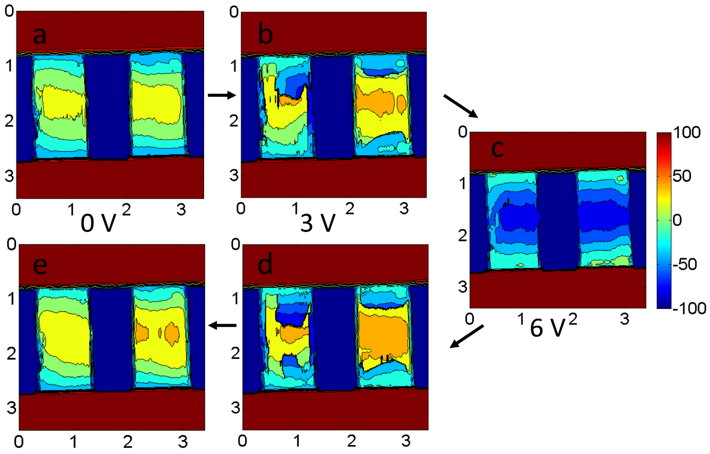

Figure 6.7: AFM-images of eleactrostatic actuation of suspended bilayered graphene beams. Lateral scales are in μm and vertical scales are in nm. Starting at V_{bg}=0 V (a) the voltage on the back-gate is increased in steps to 3 V (b) and 6 V (c) before being decreased to 3 V (d) and 0 V (e).

when the direction of sweep in V_{bg} was changed.

It can be noted that hysteresis would be expected from the bistable system of a buckled beam due to the energy barrier between local minimum and global minimum. Probably this barrier is overcome by the adhesion to the AFM-tip to the graphene. When the tip comes close to the graphene there might be an adhesive force strong enough to pull the beam from a metastable state. Thus the tip could be able to lift the beam from downwards to upwards buckling when the former is a local minimum and the latter is a global minimum.

6.3.4 Bending rigidity

Despite the atomic nature of graphene it has been shown that continuum mechanics can be used to accurately describe its motion [62]. Since the graphene membranes described here are buckled in two orthogonal directions they are expected to have similar properties of deformation as convex shells. Convex shells display buckling instability under external pressure, which is observed as snap-through from locally convex to concave buckling [141].

Then it is found that under moderate external pressure, the shell will remain unaffected. This is because the energy cost of initiating a deformation is larger than the work done by the external pressure upon such a deformation.

When the external pressure is increased beyond the critical value an inwards bulge is formed at the structurally weakest point. It is assumed that the bulge forms a mirror reflection of the original surface in a plane perpendicular to the symmetry axis [141]. This means that inside the bulge the free energy remains unchanged since the curvature is identical but concave instead of convex.

As a consequence, the major part of the change in free energy will occur in a narrow region around the edge of the bulge. By minimizing the free energy in this narrow region, one finds that at a critical pressure, p_{c}, the edge of the bulge will propagate outward [141]. This will continue until further propagation is hindered by the clamping edges or defects in the sample, at which point the shell is said to have snapped through.

Using this model the critical pressure can be found to be [141]

$$p_{\text{c}} = \frac{4\sqrt{\kappa n(\lambda + 2\mu)}}{R_1 R_2} \tag{6.3}$$

where R_1 and R_2 are the principal radii of curvature at the point where the instability starts and n is the number of graphene layers. The Lamé coefficients, λ and μ, are related to the mechanical properties of graphene.

Since deflection is measured in the center of the beams contamination at the edges will not influence the value of p_{c}. The curvature of the beam was obtained from AFM height-images at the position where the instability starts, i.e. at the point of lowest curvature which typically is found in the center of the beam.

It can be noted that not all designs of beams were found to have the simple structure of the first bending mode repeatedly found in μm-long beams of bilayered graphene. More complex geometries were also observed, especially for monolayered graphene beams of longer length.

Possibly this could be due to wrinkles formed around defects in or on graphene, having higher probability to occur on larger beams and more impact on monolayered graphene with its low bending rigidity. For monolayered graphene 2 out of 11 fabricated suspended beams and membranes have shown snapthrough. For bilayered graphene that number is 17 out of 28.

The electrostatic pressure applied in our experiments can be calculated from the parallel plate model. From equation 6.3, the bending rigidity is given by

$$\kappa = \left(\frac{R_1 R_2}{d^2}\right)^2 \frac{{\varepsilon_0}^2 {V_c}^4}{64n(\lambda + 2\mu)} \tag{6.4}$$

where d is the effective distance to the gate, ε_0 is the vacuum permittivity.

Results for fully clamped beams of bilayered graphene are plotted on a log-log scale in figure 6.8. According to the model the points should fall along a straight line with unit slope. The bending rigidity can then be determined from the value of the y-axis intercept.

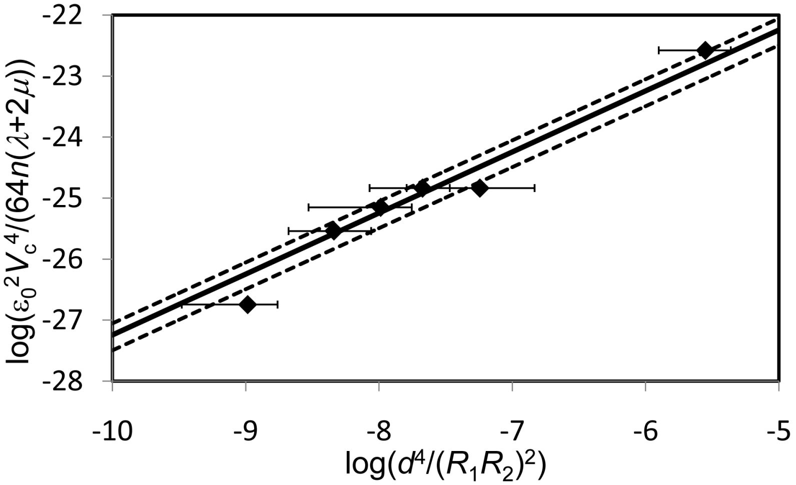

Figure 6.8: Log-log plot of measured values on critical voltage and curvature for fully-clamped bilayered beams. The full line is the modelled values according to equation 6.4 for $\kappa = 35.5$ eV. Striped lines are modeled values for κ according to upper and lower error-bar.

The measurements follow a straight line with unit slope for the whole range of curvatures. Thus the snap-through buckling in fully-clamped membranes of bilayered graphene is well described by our model, if a correct value of the bending rigidity is used. From our measurements we find $\kappa_{\text{bi}} = 35^{+20}_{-15}$ eV.

The obtained value of κ_{bi} is an order of magnitude larger than calculated assuming free sliding and 5 times smaller than calculated assuming no sliding at all between the two layers. This indicates that the assumptions on interaction between the sheets of graphene should be refined in the models for calculating κ_{bi}.

Modeling using measurements from doubly-clamped beam was also done. It was found that $\kappa \sim R^3 \cdot V_{\text{c}}^4$, where R is the radius of curvature along the beam. Assuming κ_{bi} to be 35 eV, it was estimated for monolayered graphene that $\kappa = 7^{+4}_{-3}$ eV and for trilayered graphene that $\kappa_{\text{tri}} = 126^{+71}_{-53}$ eV.

Measurements of κ_{bi} were done on μm-sized samples at room temperature. At finite temperatures ripples of tens of nanometers length are formed and stabilize graphene. Hence the measured value is the effective bending rigidity at room temperature on length-scales larger than the corrugation length, which is the value to be used in simulations of deformation for devices operating in the same range of temperatures.

6.4 Conclusions

Fabrication of buckled beams of graphene has been described. The mechanism causing buckling is the compressive strain formed during thermal cycling. During electrostatic actuation the beams have shown snap-through buckling. The snap-through of buckled beams has been possible to model using continuum mechanics. The bending rigidity of bilayered graphene has been found to be 35^{+20}_{-15} eV.

The experimentally obtained value of κ_{bi} can be used as a guideline when developing better models of the mechanical interaction between the layers in few-layered graphene. Also a more precise value of the bending rigidity enables more precise simulations of the mechanical properties of devices from bilayered graphene.

The buckled beams themselves also have interesting properties for use in devices. Compared to initially straight beams curved beams have been shown to have larger displacement [142], greater tunability of resonance-frequency [143] and could be used for memory applications [144].

Chapter 7

CNTFETs with moveable gates

Carbon nanotubes have been described to have excellent electrical properties with their high on/off ratio and mobility. Graphene has outstanding mechanical properties with high strength, low mass and tunable frequency of resonance. Each of those properties on their own have many possible applications and combining them enables completely novel nanoelectromechanical systems.

7.1 Introduction

For a field-effect transistor (FET) an important figure of merit is the inverse subthreshold slope, S, which is the change in gate-voltage, V_{g}, needed to change the current through the channel, I_{d}, by one order of magnitude. A low S is desirable since it allow the use of low supply voltage, hence low power dissipation, while keeping a high ratio between I_{on} and I_{off}.

The inverse subthreshold slope is determined by the electrostatic coupling to the gate and given by

$$S = \frac{\partial V_{\mathrm{g}}}{\partial \log_{10} I_{\mathrm{d}}} = \ln(10)\frac{k_{\mathrm{b}}T}{q}\frac{C_{\mathrm{tot}}}{C_{\mathrm{g}}}, \tag{7.1}$$

where C_{tot} is is the sum of all capacitances to the channel. For an ideal FET, where the total capacitance is dominated by C_{g}, S is restricted by the thermal limit of 2.3 $k_{\mathrm{b}}T/q$ equal to 60 mV/decade at room temperature.

However the thermal limit on S can be overcome by using a moveable gate. Then the coupling between gate and channel can be made more effective by reducing their interdistance. If C_{g} is allowed to change, i.e. by varying the separation to the gate, equation 7.1 is modified to

$$S = \ln(10)\frac{k_{\mathrm{b}}T}{q}\frac{C_{\mathrm{tot}}}{C_{\mathrm{g}} + \Delta V_{\mathrm{g}}\partial C_{\mathrm{g}}/\partial V_{\mathrm{g}}}, \tag{7.2}$$

implying that S will always be smaller for a non-static gate since both electrostatic and mechanical gating is combined.

An FET made of silicon with moveable gate has been shown to have an S lower than the thermal limit [145]. However the device relied on physical contact between the gate electrode and the gate dielectric, leading to a large hysteresis. Also relatively high voltages were required to move the gate electrode due to its thickness, which is difficult to decrease when using top-down-fabrication.

7.2 Carbon nanotube gate

Thin gate electrodes can be made of low-dimensional conducting structures. For example a metallic CNT can be suspended between electrodes above a semiconducting CNT, as shown in figure 7.1. When a voltage is applied to the suspended gate-CNT it will be actuated towards the semiconducting CNT-channel, thus electrostatic and mechanical gating are combined. Simulations of such device have shown that S lower than the thermal limit can be obtained using a carbon nanotube as a moveable gate for a CNTFET [146].

Similar devices with non-suspended, static CNT-gates have been successfully fabricated [46]. Then a fixed negative V_{bg} was applied to electrostatically dope the semiconducting CNT with holes. A voltage applied to the metallic CNT locally induced a potential barrier in the channel, thus making it possible to control its conductance.

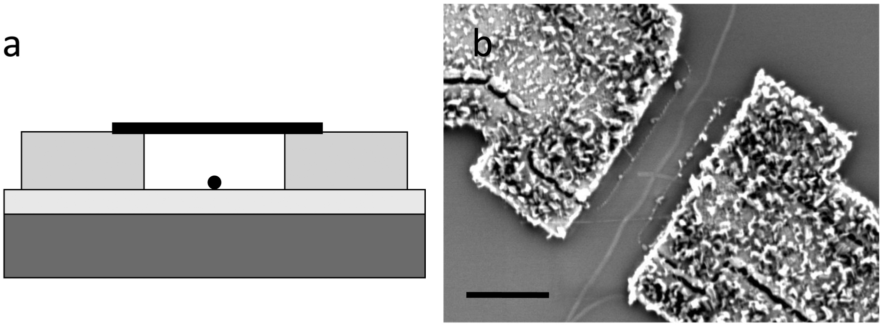

Figure 7.1: (a) Schematic image of a CNTFET with suspended CNT-gate. (b) SEM-image of a CNTFET with suspended CNT-gate.

For a CNTFET with moveable CNT-gate of μm-length the suspended height should be low, on the order of tens of nm, to have S below the thermal limit [146]. Then the scheme of fabrication used for suspending graphene, figure 6.1, where the gate-material is clamped followed by etching of the substrate does not work. Even though critical point drying is used, slack in the

CNT will make it fall down if the aspect-ratio between electrode height and separation is not sufficient [61].

An alternative is to make the suspending electrodes first, pattern catalyst on top and grow CNTs as the final step. Previously it has been shown that CNTs grown at the end of fabrication are very clean, thus having excellent electrical and mechanical properties, and can be suspended across trenches [65]. However the lack of control in length, direction and number of SWNTs during synthesis make successful fabrication very difficult and reproducibility even harder.

Attempts to fabricate a CNTFET with a suspended CNT-gate have been made. First SWNTs are grown and a suitable tube is located in SEM. Contact electrodes are patterned on the SWNT and suspending electrodes are made on both sides of it. Mo is used as electrode-material since it is compatible with conditions of synthesis. Catalyst material, alumina and iron, was patterned on top of the suspending electrodes and finally a second step of synthesis of SWNTs was done.

The sample shown in figure 7.1b displays both the possibilities and the limitations of the process. Suspending electrodes are formed with a semiconducting CNT remaining on the substrate in between. SWNTs, suspended from electrode to electrode, of μm-length can be grown. However there might also be other SWNTs grown which are not suspended but instead fall down onto the semiconducting CNT, thus short-circuiting the device.

Hence the method of fabrication works in principle. But it is time-consuming, with many steps and individual design around each semiconducting CNT, in addition to having very low yield. Despite optimization of electrode separation and area of catalyst no working device has been made yet.

7.3 Graphene gate

Graphene can be used as a moveable gate instead of metallic CNTs. Then the excellent mechanical properties are kept while the electronic properties are less sensitive to atomic structure. From a fabrication point-of-view graphene has the advantage of being easier to locate, due to its visibility in an optical microscope. Hence flakes of graphene can be located on one sample and then transferred onto another sample [147].

In Paper V fabrication and characterization of CNTFETs with moveable gates of graphene is described. Devices are made by transferring graphene onto a sample with semiconducting CNT and suspending electrodes. Electrical characterization was done and numerical simulations show that it is possible to improve the switching characteristics compared to a static gate. Here selected parts are presented. For a more complete description the reader is referred to Paper V.

7.3.1 Experimental methods

The device, which is pictured schematically in figure 7.2f, consists of a carbon nanotube-transistor gated by a silicon back-gate and a top-gate of suspended graphene. The graphene sheet is suspended by the height of its support electrodes and can be electrostatically actuated by applying a voltage difference between the graphene and the back-gate. A step-by-step-recipe is presented in appendix B for the interested reader.

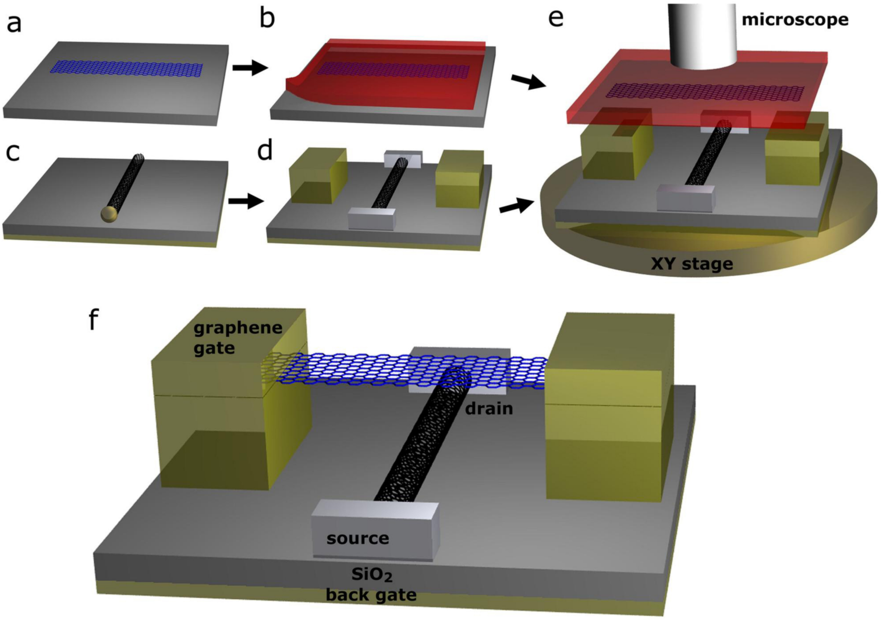

Figure 7.2: Schematic process for fabrication of CNTFET with suspended graphene gate. (a) Exfoliation of graphene. (b) Spin-coating of transfer resist-film on graphene. (c) CVD-synthesis of SWNT. (d) Patterning of electrodes without adding coating of SiN. (e) Transferring of graphene-film and alignment onto CNT-sample using optical microscope. (f) Clamping of graphene into final device.

The CNT-transistor is based on an individual single-walled nanotube. The SWNT, figure 7.2c, was synthesized by chemical vapor deposition at 900 °C and atmospheric pressure using methane as carbon precursor and a patterned thin film catalyst of 1 nm iron on 5 nm alumina deposited by electron-beam evaporation.

The SWNT was grown directly on a highly-doped silicon substrate oxidized in low-pressure-CVD to obtain a 300 nm thick thermal oxide, a thickness chosen to enhance contrast of the graphene sheet. The silicon substrate was used as back-gate both to modulate the conductance of the parts of the semiconducting CNT close to the contacts and to actuate the suspended graphene. The high level of doping made possible electrical measurements also at low temperatures.

The position of the SWNT was determined by scanning-electron microscopy, figure 7.3a. The design of the electrodes was made individually based on the position of each suitable SWNT, figure 7.3b. Suspending and side-electrodes were placed around a relatively straight segment of the CNT. Contact-electrodes were patterned a few microns away from support-electrodes.

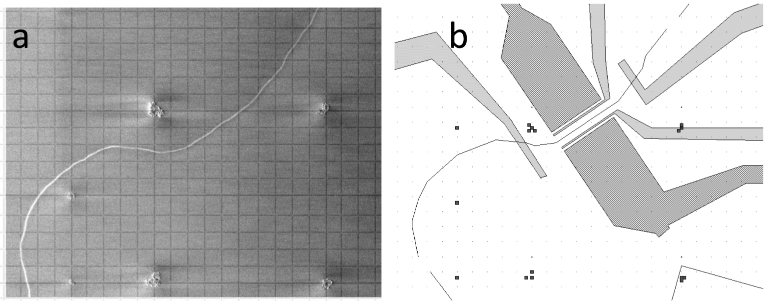

Figure 7.3: (a) SEM-image of SWNT overlaid with grid, which is aligned to Mo-marks, used for assistance when drawing position of CNT i CAD-file. (b) Design of electrodes in CAD-file. The fabricated device is shown in figure 7.4.

The side-electrodes could also be used for actuation of the suspended gate. By applying voltages of opposite polarity on them actuation, which is proportional to ΔV^2, can be achieved with a minimum change in potential in the CNT due to the symmetry of the design. However, in electrical measurements described below side-electrodes were not used.

Contact- and side-electrodes to the SWNT were defined by electron-beam lithography and lift-off after electron-beam deposition of 0.5 nm Ti and 25 nm Pd. A protective layer of 15 nm silicon nitride was deposited on top of the entire substrate using plasma-enhanced-CVD. To enable electrical measurements, openings in the layer of SiN were made on top of the contact pads by etching in a CF_4-plasma using a resist mask defined by EBL.

The pattern of the two electrodes that the sheet of graphene will be suspended between was defined by EBL with the SWNT in the middle of a 2 μm gap between the electrodes. After electron-beam evaporation of 5 nm Ti, 95 nm Au and 20 nm Pd, lift-off was used to transfer the pattern into the support electrodes, figure 7.2d.

On a typical chip around 4 devices were fabricated. Electrical characterization was made of the CNTFETs in a probe-station at room-temperature. On each chip the semiconducting CNT with lowest resistivity and highest on/off ratio was selected for further processing. It was also made sure that gating of the CNT from support electrodes was not efficient.

Graphene was transfer-printed onto a sample with CNTFET. From highly oriented pyrolytic graphite, graphene was exfoliated onto a bare silicon substrate with 300 nm oxide layer. A flake of graphene with suitable shape to be used as a suspended gate was selected in an optical microscope, figure 7.2a.

A thin film, 500 nm, of PMMA was spin-coated on the substrate, embedding the graphene-sheet from the top. The resist was baked at 180 °C. Immersion of the substrate into KOH released the resist film together with the embedded graphene, figure 7.2b.

The released thin film was transferred onto the substrate with the CNTFET, figure 7.2e. During transfer the selected sheet of graphene embedded in the resist film was aligned in an optical microscope to be positioned between the support electrodes. Then the resist film was brought into contact with the CNTFET-sample.

The transferred resist film could be used to pattern metal-clamps onto the part of graphene on top of the electrodes. The pattern of the clamps was defined by EBL and electron-beam evaporation of 0.5 nm Ti and 30 nm Pd. To keep the graphene suspended, critical-point-drying was used after lift-off, figure 7.2f.

The resulting device of a sheet of graphene suspended between electrodes above a CNT-transistor was inspected using an optical microscope, figure 7.4a, and atomic force microscope, figure 7.4b and c. Raman spectroscopy was made on selected samples to ensure that graphene was single-layered.

Electrical characterization of the devices was made in vacuum ($5 \cdot 10^{-6}$ mBar) in a cryogenic probe station at 100 K. A source-drain bias, V_{d}, was applied and either the voltage applied to the graphene gate, V_{gg}, or to the back-gate, V_{bg}, was swept while keeping the other gate at a fixed voltage.

7.3.2 Results and discussion

The results from fabrication of the CNTFETs show that the carbon nanotube and electrodes can be aligned to each other with less than 100 nm error using EBL. The error could probably be reduced further by automating the process of transferring the location of the nanotube from the SEM-image to the CAD-file used for designing the pattern and position of the electrodes.

Electrical characterization of the CNTFETs at room temperature shows that it is common to find devices with an on/off ratio of 10^3 or more and a minimum resistance of a few MΩs or less. Usually carbon nanotubes contacted by Pd electrodes display p-type behavior. After SiN-coating they are changed into n-type, either due to changes in contact work function or doping of the nanotubes [148].

The transfer printing method was shown to be able to suspend graphene between electrodes on top of a sample. In combination with critical point drying graphene could be suspended between electrodes of 2.5 μm separation and 120 nm height, hence an aspect-ratio of more than 20.

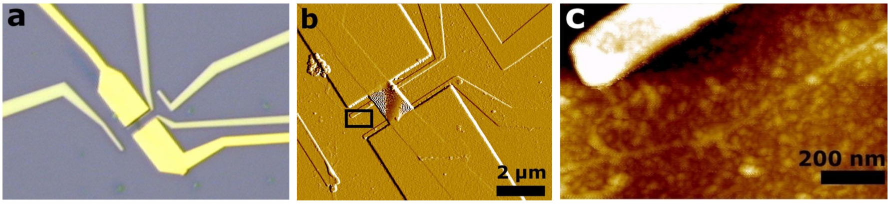

Figure 7.4: (a) Image from optical microscope of the device designed in figure 7.3b. (b) AFM-image of the same device. (c) AFM-image of the area inside black box in (b) where the CNT is seen.

The use of a CNTFET-substrate with 300 nm silicon oxide made it possible to study the transferred graphene in an optical microscope, figure 7.4a. It was observed that the color of suspended graphene was different from that of graphene lying on the substrate, hence the optical microscope could be used to study if graphene was suspended after the final step of fabrication.

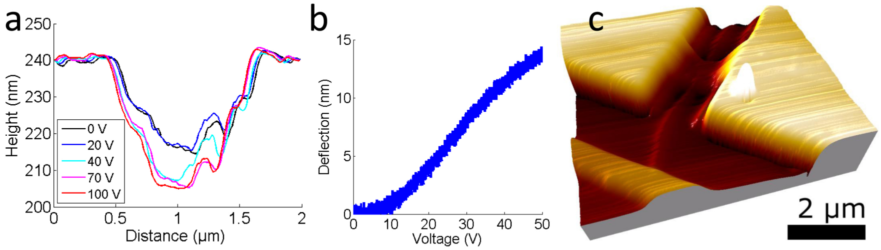

Figure 7.5: Profiles from AFM-images at different ΔV (a) and measurements of deflection (b) of test sample with fewlayered graphene suspended between electrodes of 240 nm height. (b) AFM-image of CNTFET with graphene gate collapsed into the substrate after electrical characterization.

Test samples having only suspending electrodes but no CNTFETs were made to study electrostatic actuation of transferred graphene. The profiles obtained in AFM along the beam of few-layered graphene, figure 7.5a, show that the graphene adheres to the edges of the electrodes and thus becomes U-shaped. This is similar to the observations in Chapter 6 that adhesion to electrodes gave upwards buckling. In that case the electrodes were on top of the graphene, here they are below.

Measurements of deflection, figure 7.5b, reveal that for V_{bg} lower than roughly 20 V the deflection is proportional to ${V_{\mathrm{bg}}}^2$, as expected from equation 3.1. For higher voltages, non-linearities become significant, hence the weaker dependance on V_{bg} [149].

It can be noted that the deflection observed here is relatively small compared to the distance between the graphene gate and the CNT. However deflection scales with the cube of the beam length. The suspended part of the beam in figure 7.5a was less than 1 μm and the beams used in this work for gating CNTFETs are typically 2 μm long. In addition the larger height of the electrode also reduce deflection at a given V_{bg} compared to the CNTFET-devices used in this work.

An example of sufficient deflection for graphene gates on the CNTFET-devices is shown in figure 7.5c. During electrical characterization a notable difference was observed between sweeps being done at maximum $\Delta V = |V_{\mathrm{gg}} - V_{\mathrm{bg}}| = 21$ V and $\Delta V = 22$ V. Studying the device afterwards it was found that the graphene gate had been pulled in to the surface of the substrate.

Similar to singly-clamped beams being pulled in when deflected more than 30 % of the initial distance, as observed for varactors in Chapter 4, also doubly-clamped beams are expected to pull-in at roughly the same amount of relative deflection [149]. For the device shown in figure 7.5c graphene was pulled in around $\Delta V = 21$ V, indicating that relatively low voltages are required for deflecting the graphene gate a substantial distance. Note that pull-in is expected when the beam is deflected by 30 % of the effective initial distance to the back-gate. Having 300 nm gate-oxide, this means that graphene can be deflected 70 % of the air-gap for a suspended height of 120 nm.

The graphene in the device shown in figure 7.5c remained stuck also after reducing the actuation voltage. This irreversibility indicates that care has to be taken during electrical characterization not to exceed the critical ΔV where the suspended gate gets pulled into the surface.

The contour map of I_{d} when sweeping V_{gg} and V_{bg} respectively for a SiN-coated device is shown in figure 7.6a. When both V_{gg} and V_{bg} were kept at sufficiently high positive voltages the entire CNT was n-doped and showed high conductance.

However, if V_{bg} is too low, conductance is suppressed in the parts of the CNT close to the contacts. Similarly, if V_{gg} is too low, a potential barrier is induced for the electrons in the CNT segment below the suspended graphene, hence giving a low I_{d}. It can be noted that both gates can be used to turn the device into the off-state, irrespective of the other gate.

Single sweeps of V_{gg} and V_{bg} while keeping the other gate at 10 V, figure 7.6b, show an inverse subthreshold slope of 286 mV/decade and 317 mV/decade respectively.

For a device without coating and with a few-layered graphene gate the contour map, figure 7.7a, shows ambipolar behaviour. When both gates are sufficiently positive electrons can pass through the CNT. If V_{gg} is lowered enough a potential barrier is formed beneath the gate and limits the current.

However, if V_{bg} is sufficiently low, the Schottky barriers are lowered and holes can pass into the CNT. From this setting, increasing V_{gg} will again induce a potential barrier in the middle segment of the CNT, thus limiting the current.

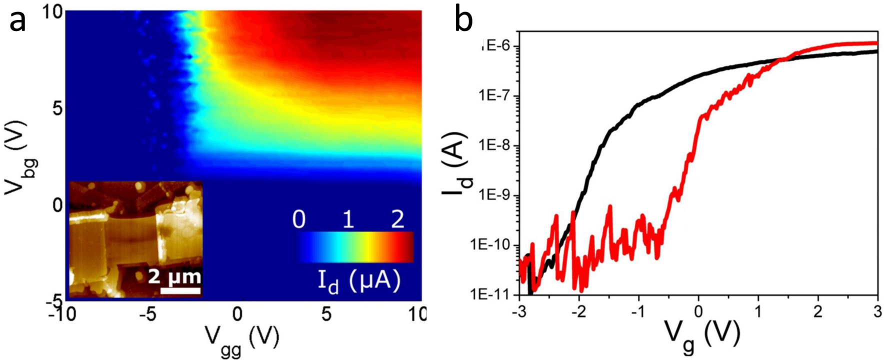

Figure 7.6: Electrical characterization of CNTFET with SiN-coating. (a) Contour map of I_d for $V_\mathrm{d} = 100$ mV at 100 K. (b) Single sweeps of V_gg (red) and V_bg (black) for $V_\mathrm{d} = 500$ mV at 100 K while keeping the other gate at 10 V.

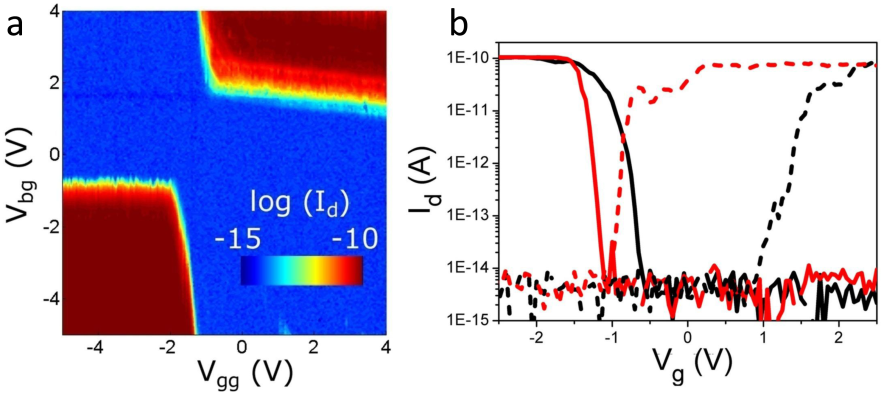

Figure 7.7: Electrical characterization of CNTFET without SiN-coating. (a) Contour map of I_d for $V_\mathrm{d} = 100$ mV at 100 K. (b) Single sweeps of V_gg (red) and V_bg (black) for $V_\mathrm{d} = 500$ mV at 100 K while keeping the gate not being swept at either 5 V (solid lines) or -4 V (dashed lines).

Single sweeps of V_gg and V_bg in the n-type branch give S of 53 mV/decade respectively 130 mV/decade. In the p-type branch both sweeps exhibit S of 66 mV/decade.

Comparing the devices, the SiN-coated CNTFET exhibits higher S. Possibly this could be due to charge traps present in the deposited nitride [150], contributing to parasitic capacitances included in C_tot in equation 7.2.

The non-coated device too has higher S than the ideal value of 20 mV/decade at 100 K. This is partly due to the relatively large air gap to the graphene gate, since the two gates placed on opposite sides of the CNT compete for control of the potential in the channel. But also charge traps on the substrate or at the interface between silicon and oxide could increase S.

Unfortunately it is not straightforward to confirm the improvement in the subthreshold slope due to actuation of the suspended gate in our measurements. It can be argued for an effect due to movement of graphene that S is lower when sweeping V_{gg} despite the effective distance, taking the dielectric medium into account, being larger. However V_{gg} only gates the middle part of the CNT while V_{bg} gates the whole CNT and the Schottky barriers at the contacts, making direct comparisons difficult.

In addition, the higher than ideal values of S indicate that charge traps have a large impact on switching behaviour in our devices. Also here differences can be expected between back-gate with oxide and graphene gate with deposited nitride and adsorbents in the gate dielectric.

To quantify the effect on S from deflection of graphene, numerical simulations of a p-type device at a temperature of 300 K were carried out. The deflection of graphene used in the simulations was obtained from measurements of deflection on a single-layered beam of 2 μm length fabricated in a way similar to the doubly-clamped beams in Chapter 6. The beam exhibited deflection similar to 7.5b, i.e. without snap-through buckling, with 37 nm deflection for $\Delta V = 10$ V.

Ignoring the effects from parasitic capacitances, for the design of the device used in measurements in figure 7.6 it was found that a deflection of 20 nm gave an improvement in S of 22 %, compared to a static device with graphene gate positioned at that maximum deflection. To reduce S below the thermal limit a deflection of 80 % was needed. However, such a large deflection can not be achieved since graphene is pulled-in at 70 % deflection.

Simulations show further that in order to be able to reduce S below the thermal limit while avoiding pull-in, the initial suspended height of the graphene gate has to be reduced to 20 nm. If the parasitic capacitances are taken into account the initial height must be reduced to 3 nm to beat the thermal limit. Even if parasitic capacitances can be lowered, e.g. by removing charge traps, it is experimentally very challenging to realize suspended graphene gates of the needed heights.

7.4 Curved graphene gate

To obtain a low inverse subthreshold slope for a CNTFET with suspended gate it is desirable to have a gate with large deflection for a small shift in ΔV. In Chapter 6 it was shown that curved beams have that property close to the critical voltage. Possibly a CNTFET with a moveable curved gate, schematically shown in figure 7.8a, could improve S beyond the thermal limit.

A proposed scheme for fabrication of such a device could be to make the

CNTFET on a silicon substrate, to be used as back-gate. The gate insulator could be 250 nm thermal oxide with 20 nm silicon nitride deposited by low-pressure CVD (LPCVD) on top. Fabrication of the CNTFET is made as described previously, except for patterning of the suspending electrodes.

In this case, the separation between CNT and graphene is determined by the thickness of a SiN-coating, which is deposited in plasma-enhanced CVD (PECVD). Graphene is transferred on top of the CNT and SiN-coating. The flake of graphene and the clamping electrodes are patterned similar to described in Chapter 6, including thermal cycling.

Silicon nitride deposited in PECVD is of lower quality than SiN deposited by LPCVD. As a consequence, etching in BOE will remove PECVD-SiN while leaving LPCVD-SiN unaffected, thus suspending the graphene gate while leaving CNTFET and its insulator to the back-gate. Being clamped by electrodes from the top, the thermal cycling will cause graphene to curve away from the CNTFET.

The back-gate actuates the curved graphene gate and controls the conductivity of the parts of the CNT close to the source- and drain-contacts. The graphene gate is used to control the conductivity of the middle part of the CNT. When deflected, the curved graphene gate will snap-through from upwards to downwards buckling, shown by full respectively striped line in figure 7.8a, at the critical ΔV. Hence separation, thus also coupling, between the CNT and the graphene will change significantly for a small shift in gate-voltage.

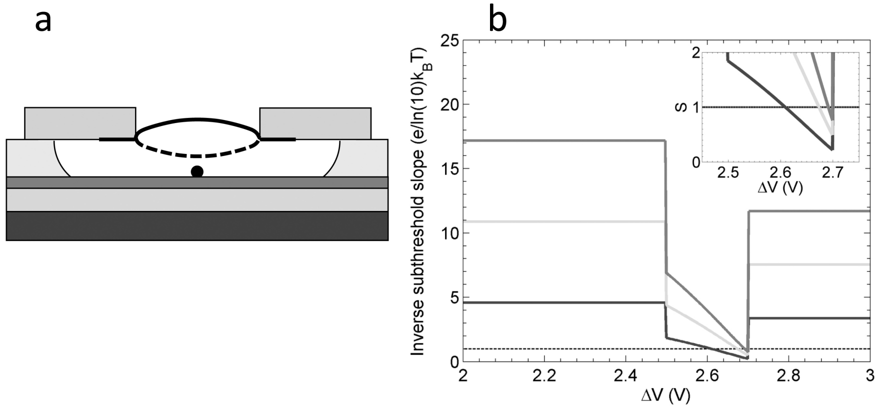

Figure 7.8: (a) Schematic image of a cross-section of a CNTFET with curved graphene gate. (b) Numerical simulations of S for a CNTFET with curved graphene gate. Top curve assumes parasitic capacitances of similar value to the CNTFET in figure 7.7, middle curve assumes half that value and bottom curve assumes no parasitic capacitance.

Numerical simulations of a p-type device with curved gate at a temperature of 300 K have been done. The thickness the PECVD-SiN was set to 40 nm. Having thinner nitride would improve coupling to the graphene gate, but also make it more difficult to fabricate suspended graphene.

Similar to the buckled beam in figure 6.6, the height of the central part of the curved graphene gate was considered to be 65 nm above the bottom of the clamping electrodes at $\Delta V = 0$ V. The deflection was approximated by being zero up to $\Delta V = 2.5$ V, then increasing linearly to 89 nm at $\Delta V = 2.7$ V and in a static position of downwards buckling for higher ΔV.

The inverse subthreshold slope when sweeping V_{gg} was calculated at different ΔV. For each value of ΔV it was assumed that CNTFET was operating at the optimal working point, i.e. the point of largest subthreshold slope. Since both V_{gg} and V_{bg} can be varied individually, that should in principle be possible to achieve.

Simulations, shown in figure 7.8b, were done with parasitic capacitances, C_{p}, of the same value as observed for the CNTFET in figure 7.7, with C_{p} being half that value and with C_{p}=0. The inverse subthreshold slopes are normalized to the thermal limit of 60 mV/decade at room temperature, striped line in figure 7.8b.

For $\Delta V < 2.5$ V the device is static and S is significantly higher than unity, in agreement with equation 7.1 when C_{g} is much lower than C_{tot}. For 2.5 V$< \Delta V < 2.7$ V the graphene gate is deflected. S is then lowered, since movement makes the second term in the denominator in equation 7.2 non-zero. For $\Delta V > 2.7$ V the device is again static. S is lower than for upwards buckling, since the reduced separation to the CNT improves coupling to the graphene gate.

During deflection, not only movement but also the reduction in gate distance improve S. The lowest value of S is found close to completion of the buckling snapthrough. Including parasitic capacitances similar to experimental observations, S down to 80 % of the thermal limit could be obtained. If parasitic capacitances are disregarded, inverse subthreshold slopes as low as 20 % of the thermal limit are predicted.

The simulations show the possibility to improve S by including a moving gate. By combining electrostatic and mechanical gating, a value of S lower than the thermal limit can be obtained. Such CNTFETs are within reach for experimental realization if a curved graphene gate is used.

7.5 Conclusions

Fabrication of CNTFETs with suspended graphene gates has been accomplished. Electrical characterization has confirmed that the graphene gate can control the conductance of the carbon nanotube channel. Inverse subthreshold slopes down to 53 mV per decade have been measured at 100 K.

Simulations have shown that deflection of the graphene improves the transfer characteristics of the CNTFET, compared to using a static gate. However an improved design has to be found to improve S beyond the thermal limit. It is not sufficient to just reduce the height of the suspended graphene in order to fabricate such a device, due to the large parasitic capacitances that are present and the fabrication challenges. Instead, the use of a curved graphene gate has been proposed.

Although the influence on the inverse subthreshold slope from deflection of the graphene gate could not be inferred directly from electrical measurements the devices proposed here could in principle be used for monitoring movement of the suspended graphene. Since a CNTFET switches by moving only a small amount of charge [46], it is suitable for use in electrical read-out of the motion of a graphene resonator.

Chapter 8

Conclusions

Carbon nanotubes and graphene are known to have remarkable properties, motivating fundamental research on the materials. Due to those properties, many applications from carbon nanotubes and graphene have been envisioned. In this work the synthesis of carbon nanotubes was studied to improve control of their structure, which influences their properties. The partial pressure of acetylene was shown to limit the addition rate of carbon to carbon nanotubes. This observation was used to explain their growth-rate, time of growth and number of walls.

Studies of the kinetics of synthesis of VANTAs on macroscopic scale is an important method to understand the basic mechanisms and microscopic processes of CNT growth. The observations in this thesis implies that the microstructure of the nanotubes could be determined during the initial part of the synthesis. Future studies with varying conditions during synthesis would be interesting. Initially, for example, high partial pressure of acetylene and temperature can be used to nucleate CNTs with many walls. Thereafter, gas composition or temperature could be changed to optimize conditions for growth of long CNTs.

It was shown that the alignment of pillars of arrays of nanotubes was improved by increasing their density. In future studies, it would be interesting to lithographically pattern each catalyst nanoparticle individually. Then their density and size-distribution could be controlled and varied systematically. Synthesis of carbon nanotubes from such arrays of nanoparticles might provide further insights into the collective effects on alignment, growth-rate and sudden termination.

In addition, such a designed array of nanoparticles possibly can be used to tailor properties of VANTAs for different applications. For electrical interconnects, high density of nanotubes could be achieved to have high conductivity. For electromechanical devices with low actuation voltage, low-density arrays of nanotubes can be made to have low effective Young's modulus.

The exceptional electrical and mechanical properties of carbon nanotubes and graphene was utilized in different nanoelectromechanical systems. Measurements from fabricated devices were compared to models and numerical simulations, to determine the electrical and mechanical properties of the devices and the materials themselves.

VANTAs were observed to move as single units during electrostatical actuated and used that to fabricate a varactor. Deflection of the VANTAs was measured and compared to simulation to determine an effective Young's modulus of 6 ± 4 MPa. The low value implies that VANTAs could be used in future applications where large deflections at low voltages are desired.

In this work controllably fabricated curved beams of graphene were made. They were shown to give snapthrough buckling upon electrostatic actuation. The bending rigidity of 35^{+20}_{-15} eV for bilayered graphene was determined, by comparing measurements of the snapthrough deflection to an existing model.

The experimentally obtained value of the bending rigidity will be useful in simulations of the mechanical properties of devices from bilayered graphene. Further it puts limit when developing models for the mechanical interaction between the layers in few-layered graphene. In addition, the buckled beams of graphene are interesting for devices requiring beams with large and sudden deflection.

The electrical properties of carbon nanotubes were combined with the mechanical properties of graphene, by fabricating CNTFETs with moveable graphene gates. The suspended graphene gate could control the conductivity of the CNTFET. Results from our simulations describe how a subthreshold slope beyond the thermal limit can be obtained by improving the geometry of the device, for example by including a curved graphene gate.

In this work, materials with partly unknown properties, such as the effective Young's modulus of VANTAs and the bending rigidity of graphene, have been used. Hence experimental measurements were carried out first. Afterwards, simulations were used to determine those properties, which could not be obtained directly from experiments.

Fabrication of NEMS has been found to give some deviations from the ideal systems typically simulated, e.g. the non-perfect vertical alignment of nanotube arrays in varactors, the contamination on beams of graphene and parasitic capacitances in CNTFETs. Future experiments should be aimed to understand and reduce those effects.

In general, the interplay between experiments and simulations will continue to be important in development of NEMS. Experimentalists need to be aware of the limits of simulations and simulations need to include the limits of experiments. However, results from experiments can be expected to be unexpected. Occasionally, keeping eyes and minds open, the unexpected results lead to new discoveries.

Acknowledgements

Looking back at the past years I have spent at the University of Gothenburg I feel gratitude to many people for sharing their knowledge and experiences of carbon nanostructures, science and life.

Goo-Hwan, you shared your passion for carbon nanotube synthesis and set a good example for the importance of hard work, constant evaluation of the work and patience. Johannes, you taught me the electronic uses of carbon nanotubes and opened the door to graphene. Also you dragged me along into daunting challenges both in the lab and on the slopes, showing me that by really trying, more than you believe can be accomplished.

Andreas, you display an inspiringly broad interest and knowledge in physics in general and nanoelectromechanics in particular. Not only did you give meaning to the devices I created but you also made me believe in the collaboration between experimentalists and theoreticians. If all second supervisors were like you there would not be any need for main supervisors.

Still I have had two. Eleanor, thank you for continued belief in me despite lack of determination for extended periods of time. I have always felt the liberty to be able to walk my own path and when coming into dark passages you have always been able to light my way. Mats, I am grateful for your supervision the last year. Your calm and experience have always been a comfort, all the way back to my first Burns-night.

During those years I always felt at home on the eight floor in Forskar-huset, thank you all friendly colleagues. Special thanks to Dag, Johan and Erik for doing your best to keep up the social activities. That is true also for Erika, who deserves a mention for being my Queen of MatLab while bringing me along, Anton and Gustav, for your passion in science and running.

If the group of Atomic Physics has felt like home, the group of Condensed Matter Physics has felt like a second home, thank you all for filling my visits with discussions of all subjects from quantum physics to family life. Daniel, you taught me the importance of not only scratching on the surface of my two-dimensional devices but to explore them in depth. Jari, thank you for support, discussions and motivation to practice for Göteborgsvarvet.

Most of the practice has been innebandy. Thank you colleagues, friends and teammates, whenever having problems at work or at home the games with you have boosted me with confidence to handle them. If I still could not solve my problems Bea, Rosie or Johanna could. Thank you, for saving my time.

SangWook, thank you for having me as a guest in your group and an even bigger thanks to all members of your group for taking good care of me and letting me know the Korean lifestyle. Special thank to Hoyeol for sharing your thoughts on graphene and life with me. I am also thankful to my Japanese friends, especially Yas, Yoki and Motoshi, for letting me know your thoughts and attitudes at work and at home.

Johan, Oleg and Andrei, thank you for the exchange of competencies. Although our collaboration has been close I would have preferred to have my research group closer. But you know I couldn't leave my cleanroom.

Being at home is my sensation also when entering the cleanroom. I am grateful to everyone who has made it possible to turn that special environment into my zone of comfort. Special mention to Bengt, Mats, Piotr and Henrik for providing experiences and Kaija for providing materials. Thanks Hossein and Linda for introducing me to the art of working in a cleanroom.

Despite not being ideal for getting new friends, I have gained a few during my hours in the suit. Niclas, thank you for sharing your knowledge in and samples of graphene together with an admirable energy and curiosity. Joachim, thanks for letting me transfer my experiences from the cleanroom and reminding me that the student should excel his master. But also for reminding me of the importance of continuing to challenge yourself.

From the cleanroom the step is never far to Niklas. Thank you for believing that everything can be solved and showing that usually it is by looking at the problems from different angles. Life is not all about nano, thank you my friends for reminding me. Daniel, thanks for perspectives, scripts and music.

Then the step is not far to home and family. Caroline, I might have doubted your support for spending nights in the lab. I might have doubted your eagerness for doing measurements whole evenings. I might have doubted your excitedness for writing down results over week-ends. But I have never doubted your love for me and for what I wanted to do.

Signe, thanks for motivation to complete my studies. Mamma, thank you for showing how much one can accomplish with the right attitude. Thomas, thanks for encouraging curiosity and problem-solving. Pappa, I am grateful for you inspiring me to follow my heart in love and in life. You still do.

Syrenvägen, Laholm
October 2011

Appendix A

The standard recipe for flow-synthesis of vertically aligned carbon nanotube arrays using furnace TCVD-system at University of Gothenburg:

- Load the substrates with catalyst into the quartz-tube on the quartz-plate. Place the substrates in the middle of the furnace, with the beam of the laser in the middle of the quartz-substrate. Align the beam of the laser to the holes in furnace by measuring and maximizing the intensity of the beam.

- Seal the tube and pump it down to roughly 0.1 mBar using rotary vane pump. Open the gas-valve to insert argon to a pressure of 100 mBar to dilute the residual gases. Pump down the tube to roughly 0.1 mBar again. Insert 900 sccm argon and 100 sccm hydrogen. When atmospheric pressure is reached open the exhaust-valve.

- Start heating the furnace to the process-temperature of 700 °C, which is reached in roughly 25 min. Anneal at 700 °C for 9 min. After 45 s further, while the gas-composition is changed to 500 sccm argon and 500 sccm hydrogen, the gas-inlet to the quartz-tube is closed and gas-inlet directly to exhaust is opened. The gas-valve to the acetylene is opened and is allowed to stabilize at the set flow-rate for 15 s.

- Close the gas-valve directly to the exhaust and open the valve to the quartz-tube. At the same time start measuring the intensity of the transmitted laser-light using the computer with LabView. Monitor the synthesis on the screen of the computer until the intensity of the transmitted light is below the sensitivity of the photodetector. Allow the synthesis to continue for the desired time of processing, 60 min to reach the terminal length even for flow-rates as low as 1 sccm.

- Close the gas-valve to the acetylene and change gas-composition back to 900 sccm argon and 100 sccm. Turn off the furnace and allow the furnace to cool down. When the temperature is below 150 °C the samples, with

CNTs grown, can be removed from the quartz-tube and are ready for characterization or further processing.

- In burst synthesis annealing is done for 15 min. Then gas-line to acetylene is opened with a set flow-rate of 3 sccm, resulting in an initial burst of acetylene before the flow-rate is stabilized, and both argon and hydrogen is changed to a flow-rate of 500 sccm each. The standard time of synthesis is 15 min.

- In synthesis of single-walled nanotubes the same processing-steps as in burst-synthesis are used. The differences are that the process-gases are methane 900 sccm and hydrogen 100 sccm during synthesis and the temperature of the furnace is 900 °C during annealing and synthesis.

Appendix B

Described below is the recipe used for fabrication of devices of CNTFETs with suspended graphene gates, which are described in Chapter 7 and Paper V. The recipe was used in the cleanroom-facilities at MC2 in Chalmers. Hence some of the steps refer to the use of equipment and processes specific to that cleanroom. However I believe that all processes could be transferred to any cleanroom with similar equipment.

Mo-marks

Start with a highly doped silicon wafer.
Etch oxide in BOE and rinse with DI and spin-drier
Clean wafer in RCA1 and RCA2.
Oxidize 28 min at 1050 °C in Centrotherm Furnace using program ”woxvari”
Wollam ellipsometer gives an oxide thickness of 304 nm
Spin UV5-0.8 5000 rpm 1 min, bake on hotplate 130 °C for 3 min
Etch back-side, to contact back-gate, in BOE for 6 min and rinse with DI and spin-drier
Remove resist in warm Remover 1165. Rinse with acetone, DI and spin-drier.
Run program ”Strip01minA” in Batchtop
Spin LOR3A 4000 rpm 1 min, bake on hotplate 180 °C for 5 min
Spin UV5-0.8 4000 rpm 1 min, bake on hotplate 130 °C for 1 min 30 s
Expose magazine-file at 10 nA in 30 min
Post-exposure bake on hotplate 130 °C for 1 min 30 s
Develop in MF24-A for 50 s, rinse in milli-Q and in quick-dump rinser
Inspect pattern and its undercut in optical microscopy
Run program ”Ash30s” in Batchtop
Deposit 10 nm Ti (1.5 Å/s) and 90 nm Mo (1.5 Å/s) using AVAC evaporator
Lift-off in Remover 1165, rinse in Remover 1165, acetone and IPA

Dicing

Spin UV5-0.8 5000 rpm 1 min, bake on hotplate 130 °C for 1 min 30 s
Dice from frontside on the position of the dicing-marks

Half-cut from back-side into 9*9 mm2 chips
Remove blue-tape and resist in acetone, rinse in acetone and IPA.

Catalyst

Run program ”Strip01minA” in Batchtop
Spin LOR3A 5000 rpm 1 min, bake on hotplate 180 °C for 5 min
Spin UV5-0.8 5000 rpm 1 min, bake on hotplate 130 °C for 1 min 30 s
Expose magazine-file at 10 nA in 20 min
Post-exposure bake on hotplate 130 °C for 1 min 30 s
Develop in MF24-A for 50 s, rinse in milli-Q and in quick-dump rinser
Inspect pattern and its undercut in optical microscopy
Run program ”Ash30s” in Batchtop
Deposit 10 nm Al2O3 (1.2 Å/s) and 1 nm Fe (0.6 Å/s) using AVAC
Lift-off in Remover 1165, rinse in Remover 1165, acetone and IPA

SWNT synthesis

Load wafer into CVD-system, pump out CVD-tube and purge gas-lines twice
Heat to 900 °C in 500 sccm Ar and 300 sccm H2 at atmospheric pressure
Anneal at 900 °C in 500 sccm Ar and 300 sccm H2 for 5 min
Grow at 900 °C in 500 sccm CH4 and 300 sccm H2 for 5 min
Let cool in 500 sccm Ar and 300 sccm H2

Pattern design

Obtain SEM-images of CNTs at 1 kV
Combine SEM-images and image of grid into overlaid images
Use overlaid images to draw position of CNT in L-Edit
Design the electrodes around the CNT by using standard design and moving it into the right position for each device

Side-electrodes

Spin Copolymer EL4 3000 rpm 1 min, bake in oven at 170 °C for 20 min (possibly oven is needed due to stress-induced curvature in wafer)
Spin ZEP A2 3000 rpm 1 min, bake in oven at 170 °C for 20 min
Expose magazine-file at 1 nA in 30 min
Develop in hexylacetate 1 min, develop in MIBK:IPA 1:2, rinse in IPA
Inspect pattern and its undercut in optical microscopy
Deposit 0.5 nm Ti (1.0 Å/s) and 25 nm Pd (2.0 Å/s) in Balzer evaporator
Lift-off in Remover 1165, rinse in Remover 1165, acetone and IPA

SiN-deposition and etching

Deposit SiN using program ”JS HFSIN” for 1 min and 33 s, nominally giving 15 nm SiN
Spin UV5-0.8 5000 rpm 1 min, bake on hot-plate at 130 °C for 12 min
Expose magazine-file ”CSG3SIN.mgn” at 10 nA in 15 min

Post-exposure bake in oven 130 °C for 12 min
Develop in MF24-A for 50 s, rinse in milli-Q and in quick-dump rinser
Inspect pattern in optical microscopy
Run program ”ash30s” in Batchtop
Etch SiN for 45 s in Batchtop using program ”NOARCF4”
Run program ”STR02B” in Batchtop, removes all resist.
Strip in Remover 1165, rinse in Remover 1165, acetone and IPA
Etch-depth in SiN and SiO was measured to be 30 nm

Graphene-electrodes
Spin LOR3A 5000 rpm 1 min, bake on hotplate 180 °C for 5 min
Spin UV5-0.8 5000 rpm 1 min, bake on hotplate 130 °C for 1 min 30 s
Expose magazine-file at 10 nA in 1 h
Post-exposure bake on hotplate 130 °C for 1 min 30 s
Develop in MF24-A for 50 s, rinse in milli-Q and in quick-dump rinser
Inspect pattern and its undercut in optical microscopy
Deposit 5 nm Ti (1.0 Å/s), 95 nm Au (6.0 Å/s) and 20 Pd (2.0 Å/s) in Balzer evaporator
Lift-off in Remover 1165, rinse in Remover 1165, acetone and IPA
Electrical characterization of the CNTFETs at room temperature

Graphene exfoliation
Take piece of tape with HOPG-sample on top
Apply tape on HOPG, press gently and remove to get sample T1
Inspect visually with backlight. Look for large and light-grey flakes.
If no well-shaped flakes are found then throw away sample T1 and restart.
If sample looks good then keep it for further processing.
If graphene looks too dark, apply tape and press gently. Remove to get T2.
Inspect T1 and T2 visually and continue.
Take a good tape-sample, TX, with grapheme facing up and put the Si-substrate with 300 nm oxide on TX with frontside facing down towards TX.
Put tape on the back-side of the Si-substrate and press/scratch with taped glass-slide from back-side 15 times
Look for green areas on front-side of substrate and note their position.
Remove the substrate from the tape.
Inspect substrate in optical microscope and find a suitable flake to transfer.

Graphene-film preparation
Spin PMMA 950k C4 at 4500 rpm 45s giving roughly 500 nm thickness.
Bake on hotplate 180 °C for 2 min (to keep film flexible enough).
Find position of the good flake in microscope and note rough position.
Cut film-holder from 2*2 cm^2 thermal tape into T-shape with hole.
Place film-holder on right position on substrate with film, press holder into good contact.

Mix KOH 4M (11.2g KOH+50 ml DI) in Teflon beakers
Heat KOH with hot-plate set at 240 °C (in practice giving 60 to 80 °C)
Put substrate with film-holder into KOH for 7 min or until film is removed from substrate (sometimes mechanical assistance).
Rinse film thoroughly in DI and remove excess DI using paper-tissue and carefully blow dry in nitrogen.

Graphene transfer

Fasten film-holder in transfer-translator (rebuilt probe-holder) and find position and orientation of the flake to transfer.
Raise film-holder and put CNTFET-sample on microscopy-stage into focus (at 50X magnification-lens).
Find the electrode-gap to be bridged by graphene. Rotate the sample to align the gap to the flake and avoid short-circuiting of other flakes.
Lower sample and put film-holder into focus.
Add small drop of DI onto sample (5 μL) to improve contact.
Raise sample to put it into contact with film-holder.
Adjust flake-position using transfer-translator and confirm correct position.
Remove transfer-translator while keeping film-holder stuck to sample.
Confirm maintained correct positioning of the flake in optical microscope.
Let sample and film-holder dry completely for 15-30 min.
Remove film-holder from sample while keeping the desired part of film left on sample.
Confirm maintained correct positioning of the flake in optical microscope.

Clamping-electrodes

Expose magazine-file at 1000 μC/cm^2
Develop in MIBK:IPA 1:2 for 60 s, rinse in IPA
Inspect pattern in optical microscopy
Deposit 0.5 nm Ti (0.7 Å/s) and 30 Pd (2.0 Å/s) in AVAC evaporator, cover edges with foil in order to not connect Pd-area with back-side.
Lift-off in acetone and CPD from acetone to get suspended graphene.
Inspect device optically and in AFM for suspended graphene
Electrical characterization at 100 K

Bibliography

[1] A.K. Geim and K.S. Novoselov. The rise of graphene. *Nature materials*, 6(3):183–191, 2007.

[2] Phaedon Avouris, Zhihong Chen, and Vasili Perebeinos. Carbon-based electronics. *Nature nanotechnology*, 2:605–615, Oct 2007.

[3] H. W. Kroto, J. R. Heath, S. C. O'Brien, R. F. Curl, and R. E. Smalley. C_{60}: Buckminsterfullerene. *Nature*, 318:162–163, Nov 1985.

[4] K. S. Novoselov, A. K. Geim, S. V. Morozov, D. Jiang, Y. Zhang, S. V. Dubonos, I. V. Grigorieva, and A. A. Firsov. Electric field effect in atomically thin carbon films. *Science*, 306(5696):666–669, 2004.

[5] Sumio Iijima. Helical microtubules of graphitic carbon. *Nature*, 354:56–58, Nov 1991.

[6] P. R. Wallace. The band theory of graphite. *Phys. Rev.*, 71:622–634, May 1947.

[7] L. Jiao, L. Zhang, X. Wang, G. Diankov, and H. Dai. Narrow graphene nanoribbons from carbon nanotubes. *Nature*, 458(7240):877–880, 2009.

[8] T. Hayashi, Y.A. Kim, T. Matoba, M. Esaka, K. Nishimura, T. Tsukada, M. Endo, and M.S. Dresselhaus. Smallest freestanding single-walled carbon nanotube. *Nano letters*, 3(7):887–889, 2003.

[9] X. Zhao, Y. Liu, S. Inoue, T. Suzuki, RO Jones, and Y. Ando. Smallest carbon nanotube is 3 Å in diameter. *Physical review letters*, 92(12):125502, 2004.

[10] X. Wang, Q. Li, J. Xie, Z. Jin, J. Wang, Y. Li, K. Jiang, and S. Fan. Fabrication of ultralong and electrically uniform single-walled carbon nanotubes on clean substrates. *Nano Letters*, 9(9):3137–3141, 2009.

[11] R. Al-Jishi and G. Dresselhaus. Lattice-dynamical model for graphite. *Physical Review B*, 26:4514–4522, 1982.

[12] A.K. Geim. Graphene: status and prospects. *Science*, 324(5934):1530, 2009.

[13] N. D. Mermin. Crystalline order in two dimensions. *Phys. Rev.*, 176:250–254, Dec 1968.

[14] C.H. Lui, L. Liu, K.F. Mak, G.W. Flynn, and T.F. Heinz. Ultraflat graphene. *Nature*, 462(7271):339–341, 2009.

[15] J.C. Meyer, AK Geim, MI Katsnelson, KS Novoselov, TJ Booth, and S. Roth. The structure of suspended graphene sheets. *Nature*, 446(7131):60–63, 2007.

[16] C. Lee, X. Wei, J.W. Kysar, and J. Hone. Measurement of the elastic properties and intrinsic strength of monolayer graphene. *Science*, 321(5887):385, 2008.

[17] M.F. Yu, O. Lourie, M.J. Dyer, K. Moloni, T.F. Kelly, and R.S. Ruoff. Strength and breaking mechanism of multiwalled carbon nanotubes under tensile load. *Science*, 287(5453):637, 2000.

[18] B. Partoens and F. M. Peeters. From graphene to graphite: Electronic structure around the K point. *Phys. Rev. B*, 74:075404, Aug 2006.

[19] C. T. White, D. H. Robertson, and J. W. Mintmire. Helical and rotational symmetries of nanoscale graphitic tubules. *Phys. Rev. B*, 47(9):5485–5488, Mar 1993.

[20] M.Y. Han, B. Özyilmaz, Y. Zhang, and P. Kim. Energy band-gap engineering of graphene nanoribbons. *Physical Review Letters*, 98(20):206805, 2007.

[21] Gilbert D. Nessim. Properties, synthesis, and growth mechanisms of carbon nanotubes with special focus on thermal chemical vapor deposition. *Nanoscale*, 2(8):1306–1323, 2010.

[22] T. Belin and F. Epron. Characterization methods of carbon nanotubes: a review. *Materials Science and Engineering B*, 119(2):105–118, 2005.

[23] B. Ziaie, A. Baldi, and M.Z. Atashbar. Introduction to micro-/nanofabrication. *Springer Handbook of Nanotechnology*, pages 231–269, 2010.

[24] Sumio Iijima and Toshinari Ichihashi. Single-shell carbon nanotubes of 1-nm diameter. *Nature*, 363:603–605, Jun 1993.

[25] Andreas Thess, Roland Lee, Pavel Nikolaev, Hongjie Dai, Pierre Petit, Jerome Robert, Chunhui Xu, Young Hee Lee, Seong Gon Kim, Andrew G. Rinzler, Daniel T. Colbert, Gustavo E. Scuseria, David Tomanek, John E. Fischer, and Richard E. Smalley. Crystalline ropes of metallic carbon nanotubes. *Science*, 273(5274):483–487, 1996.

[26] K.S. Kim, Y. Zhao, H. Jang, S.Y. Lee, J.M. Kim, K.S. Kim, J.H. Ahn, P. Kim, J.Y. Choi, and B.H. Hong. Large-scale pattern growth of graphene films for stretchable transparent electrodes. *Nature*, 457(7230):706–710, 2009.

[27] X. Li, W. Cai, J. An, S. Kim, J. Nah, D. Yang, R. Piner, A. Velamakanni, I. Jung, E. Tutuc, et al. Large-area synthesis of high-quality and uniform graphene films on copper foils. *Science*, 324(5932):1312, 2009.

[28] L. Jiao, B. Fan, X. Xian, Z. Wu, J. Zhang, and Z. Liu. Creation of nanostructures with poly (methyl methacrylate)-mediated nanotransfer printing. *Journal of the American Chemical Society*, 130(38):12612–12613, 2008.

[29] K.V. Emtsev, A. Bostwick, K. Horn, J. Jobst, G.L. Kellogg, L. Ley, J.L. McChesney, T. Ohta, S.A. Reshanov, J. Röhrl, et al. Towards wafer-size graphene layers by atmospheric pressure graphitization of silicon carbide. *Nature materials*, 8(3):203–207, 2009.

[30] Y. Hernandez, V. Nicolosi, M. Lotya, F.M. Blighe, Z. Sun, S. De, IT McGovern, B. Holland, M. Byrne, Y.K. Gun'Ko, et al. High-yield production of graphene by liquid-phase exfoliation of graphite. *Nature Nanotechnology*, 3(9):563–568, 2008.

[31] P. Blake, EW Hill, A.H.C. Neto, KS Novoselov, D. Jiang, R. Yang, TJ Booth, and AK Geim. Making graphene visible. *Applied Physics Letters*, 91:063124, 2007.

[32] Kazu Suenaga, Hideaki Wakabayashi, Masanori Koshino, Yuta Sato, Koki Urita, and Sumio Iijima. Imaging active topological defects in carbon nanotubes. *Nat Nano*, 2:358–360, Jun 2007.

[33] Kazutomo Suenaga Ayako Hashimoto Kouki Urita Kenji Hata Sumio Iijima Hongwei Zhu. Atomic-resolution imaging of the nucleation points of single-walled carbon nanotubes. *Small*, 1:1180–1183, 2005.

[34] M. S. Dresselhaus, G. Dresselhaus, A. Jorio, A. G. Souza Filho, and R. Saito. Raman spectroscopy on isolated single wall carbon nanotubes. *Carbon*, 40(12):2043 – 2061, 2002.

[35] A. Jorio, R. Saito, J. H. Hafner, C. M. Lieber, M. Hunter, T. McClure, G. Dresselhaus, and M. S. Dresselhaus. Structural (n,m) determination of isolated single-wall carbon nanotubes by resonant raman scattering. *Phys. Rev. Lett.*, 86(6):1118–1121, Feb 2001.

[36] AC Ferrari, JC Meyer, V. Scardaci, C. Casiraghi, M. Lazzeri, F. Mauri, S. Piscanec, D. Jiang, KS Novoselov, S. Roth, et al. Raman spectrum of graphene and graphene layers. *Physical Review Letters*, 97(18):187401, 2006.

[37] TMG Mohiuddin, A. Lombardo, RR Nair, A. Bonetti, G. Savini, R. Jalil, N. Bonini, DM Basko, C. Galiotis, N. Marzari, et al. Uniaxial strain in graphene by raman spectroscopy: G peak splitting, grüneisen parameters, and sample orientation. *Physical Review B*, 79(20):205433, 2009.

[38] R.H. Baughman, A.A. Zakhidov, and W.A. De Heer. Carbon nanotubes–the route toward applications. *Science*, 297(5582):787, 2002.

[39] S. Bae, H. Kim, Y. Lee, X. Xu, J.S. Park, Y. Zheng, J. Balakrishnan, T. Lei, H.R. Kim, Y.I. Song, et al. Roll-to-roll production of 30-inch graphene films for transparent electrodes. *Nature nanotechnology*, 5(8):574–578, 2010.

[40] F. Bonaccorso, Z. Sun, T. Hasan, and AC Ferrari. Graphene photonics and optoelectronics. *Nature Photonics*, 4(9):611–622, 2010.

[41] M.D. Stoller, S. Park, Y. Zhu, J. An, and R.S. Ruoff. Graphene-based ultracapacitors. *Nano letters*, 8(10):3498–3502, 2008.

[42] P. Avouris. Graphene: Electronic and photonic properties and devices. *Nano letters*, 2010.

[43] C. Chen, S. Rosenblatt, K.I. Bolotin, W. Kalb, P. Kim, I. Kymissis, H.L. Stormer, T.F. Heinz, and J. Hone. Performance of monolayer graphene nanomechanical resonators with electrical readout. *Nature nanotechnology*, 4(12):861–867, 2009.

[44] R. Chau, S. Datta, M. Doczy, B. Doyle, B. Jin, J. Kavalieros, A. Majumdar, M. Metz, and M. Radosavljevic. Benchmarking nanotechnology for high-performance and low-power logic transistor applications. *Nanotechnology, IEEE Transactions on*, 4(2):153–158, 2005.

[45] F. Kreupl, A.P. Graham, GS Duesberg, W. Steinhögl, M. Liebau, E. Unger, and W. Hönlein. Carbon nanotubes in interconnect applications. *Microelectronic Engineering*, 64(1):399–408, 2002.

[46] J. Svensson, A.A. Sourab, Y. Tarakanov, D.S. Lee, S.J. Park, S.J. Baek, Y.W. Park, and E.E.B. Campbell. The dependence of the Schottky barrier height on carbon nanotube diameter for Pd-carbon nanotube contacts. *Nanotechnology*, 20:175204, 2009.

[47] A. Javey, J. Guo, Q. Wang, M. Lundstrom, H. Dai, et al. Ballistic carbon nanotube field-effect transistors. *Nature*, 424(6949):654–657, 2003.

[48] T. Dürkop, SA Getty, E. Cobas, and MS Fuhrer. Extraordinary mobility in semiconducting carbon nanotubes. *Nano Letters*, 4(1):35–39, 2004.

[49] A. Javey, H. Kim, M. Brink, Q. Wang, A. Ural, J. Guo, P. McIntyre, P. McEuen, M. Lundstrom, H. Dai, et al. High-kappa dielectrics for advanced carbon-nanotube transistors and logic gates. *Nature Materials*, 1(4):241–246, 2002.

[50] KL Ekinci, XMH Huang, and ML Roukes. Ultrasensitive nanoelectromechanical mass detection. *Applied Physics Letters*, 84(22):4469–4471, 2004.

[51] A.D. O'Connell, M. Hofmeinz, M. Ansmann, R.C. Bialczak, M. Lenander, E. Lucero, M. Neeley, D. Sank, H. Wang, M. Weides, et al. Quantum ground state and single-phonon control of a mechanical resonator. *Nature*, 464(7289):697–703, 2010.

[52] J.S. Bunch, A.M. van der Zande, S.S. Verbridge, I.W. Frank, D.M. Tanenbaum, J.M. Parpia, H.G. Craighead, and P.L. McEuen. Electromechanical resonators from graphene sheets. *Science*, 315(5811):490, 2007.

[53] K.I. Bolotin, KJ Sikes, Z. Jiang, M. Klima, G. Fudenberg, J. Hone, P. Kim, and HL Stormer. Ultrahigh electron mobility in suspended graphene. *Solid State Communications*, 146(9-10):351–355, 2008.

[54] A.M. Zande, R.A. Barton, J.S. Alden, C.S. Ruiz-Vargas, W.S. Whitney, P.H.Q. Pham, J. Park, J.M. Parpia, H.G. Craighead, and P.L. McEuen. Large-scale arrays of single-layer graphene resonators. *Nano letters*, 2010.

[55] V. Sazonova, Y. Yaish, H. Üstünel, D. Roundy, T.A. Arias, and P.L. McEuen. A tunable carbon nanotube electromechanical oscillator. *Nature*, 431(7006):284–287, 2004.

[56] P. Bøggild, T.M. Hansen, C. Tanasa, and F. Grey. Fabrication and actuation of customized nanotweezers with a 25 nm gap. *Nanotechnology*, 12:331, 2001.

[57] R. Lefevre, MF Goffman, V. Derycke, C. Miko, L. Forró, JP Bourgoin, and P. Hesto. Scaling law in carbon nanotube electromechanical devices. *Physical review letters*, 95(18):185504, 2005.

[58] J.S. Bunch, S.S. Verbridge, J.S. Alden, A.M. Van Der Zande, J.M. Parpia, H.G. Craighead, and P.L. McEuen. Impermeable atomic membranes from graphene sheets. *nano letters*, 8(8):2458–2462, 2008.

[59] D. García-Sánchez, A. San Paulo, M.J. Esplandiú, F. Perez-Murano, L. Forró, A. Aguasca, and A. Bachtold. Mechanical detection of carbon nanotube resonator vibrations. *Physical review letters*, 99(8):85501, 2007.

[60] D. García-Sánchez, AM Van Der Zande, A.S. Paulo, B. Lassagne, PL McEuen, and A. Bachtold. Imaging mechanical vibrations in suspended graphene sheets. *Nano letters*, 8(5):1399–1403, 2008.

[61] B. Witkamp, M. Poot, and H.S.J. Van Der Zant. Bending-mode vibration of a suspended nanotube resonator. *Nano letters*, 6(12):2904–2908, 2006.

[62] J. Atalaya, A. Isacsson, and J.M. Kinaret. Continuum elastic modeling of graphene resonators. *Nano letters*, 8(12):4196–4200, 2008.

[63] K.C. Schwab and M.L. Roukes. Putting mechanics into quantum mechanics. *Physics Today*, 58(7):36–42, 2005.

[64] AK Hüttel, M. Poot, B. Witkamp, and HSJ van der Zant. Nanoelectromechanics of suspended carbon nanotubes. *New Journal of Physics*, 10:095003, 2008.

[65] G.A. Steele, A.K. Hüttel, B. Witkamp, M. Poot, H.B. Meerwaldt, L.P. Kouwenhoven, and H.S.J. van der Zant. Strong coupling between single-electron tunneling and nanomechanical motion. *Science*, 325(5944):1103, 2009.

[66] W. Bao, G. Liu, Z. Zhao, H. Zhang, D. Yan, A. Deshpande, B. LeRoy, and C.N. Lau. Lithography-free fabrication of high quality substrate-supported and freestanding graphene devices. *Nano Research*, 3(2):98–102, 2010.

[67] A. Eichler, J. Moser, J. Chaste, M. Zdrojek, I. Wilson-Rae, and A. Bachtold. Nonlinear damping in mechanical resonators made from carbon nanotubes and graphene. *Nature Nanotechnology*, 6(6):339–342, 2011.

[68] A.K. Huttel, G.A. Steele, B. Witkamp, M. Poot, L.P. Kouwenhoven, and H.S.J. van der Zant. Carbon nanotubes as ultrahigh quality factor mechanical resonators. *Nano letters*, 9(7):2547–2552, 2009.

[69] H.Y. Chiu, P. Hung, H.W.C. Postma, and M. Bockrath. Atomic-scale mass sensing using carbon nanotube resonators. *Nano letters*, 8(12):4342–4346, 2008.

[70] J. Atalaya, J.M. Kinaret, and A. Isacsson. Nanomechanical mass measurement using nonlinear response of a graphene membrane. *EPL (Europhysics Letters)*, 91:48001, 2010.

[71] Feng Ding, Peter Larsson, J. Andreas Larsson, Rajeev Ahuja, Haiming Duan, Arne Rosen, and Kim Bolton. The importance of strong carbon-metal adhesion for catalytic nucleation of single-walled carbon nanotubes. *Nano Letters*, 8(2):463–468, 2008.

[72] R. S. Wagner and W. C. Ellis. Vapor-liquid-solid mechanism of single crystal growth. *Applied Physics Letters*, 4(5):89–90, 1964.

[73] Yahachi Saito, Mitsumasa Okuda, Masato Tomita, and Takayoshi Hayashi. Extrusion of single-wall carbon nanotubes via formation of small particles condensed near an arc evaporation source. *Chemical Physics Letters*, 236(4-5):419–426, 1995.

[74] Robert Seidel, Georg S. Duesberg, Eugen Unger, Andrew P. Graham, Maik Liebau, and Franz Kreupl. Chemical vapor deposition growth of single-walled carbon nanotubes at 600 °C and a simple growth model. *The Journal of Physical Chemistry B*, 108(6):1888–1893, 2004.

[75] P.B. Amama, C.L. Pint, L. McJilton, S.M. Kim, E.A. Stach, P.T. Murray, R.H. Hauge, and B. Maruyama. Role of water in super growth of single-walled carbon nanotube carpets. *Nano letters*, 9(1):44–49, 2008.

[76] E. Einarsson, Y. Murakami, M. Kadowaki, and S. Maruyama. Growth dynamics of vertically aligned single-walled carbon nanotubes from in situ measurements. *Carbon*, 46(6):923–930, 2008.

[77] A.A. Puretzky, G. Eres, C.M. Rouleau, I.N. Ivanov, and D.B. Geohegan. Real-time imaging of vertically aligned carbon nanotube array growth kinetics. *Nanotechnology*, 19:055605, 2008.

[78] P. Vinten, P. Marshall, J. Lefebvre, and P. Finnie. Distinct termination morphologies for vertically aligned carbon nanotube forests. *Nanotechnology*, 21:035603, 2010.

[79] K. Hasegawa and S. Noda. Millimeter-tall single-walled carbon nanotubes rapidly grown with and without water. *ACS nano*, 2011.

[80] F. Ding, P. Larsson, J.A. Larsson, R. Ahuja, H. Duan, A. Rosén, and K. Bolton. The importance of strong carbon-metal adhesion for catalytic nucleation of single-walled carbon nanotubes. *Nano letters*, 8(2):463–468, 2008.

[81] Daisuke Takagi, Yoshikazu Homma, Hiroki Hibino, Satoru Suzuki, and Yoshihiro Kobayashi. Single-walled carbon nanotube growth from highly activated metal nanoparticles. *Nano Letters*, 6(12):2642–2645, 2006.

[82] Yiming Li, Woong Kim, Yuegang Zhang, Marco Rolandi, Dunwei Wang, and Hongjie Dai. Growth of single-walled carbon nanotubes from discrete catalytic nanoparticles of various sizes. *The Journal of Physical Chemistry B*, 105(46):11424–11431, 2001.

[83] YY Wei, G. Eres, VI Merkulov, and DH Lowndes. Effect of catalyst film thickness on carbon nanotube growth by selective area chemical vapor deposition. *Applied Physics Letters*, 78:1394, 2001.

[84] Jing Kong, Hyongsok T. Soh, Alan M. Cassell, Calvin F. Quate, and Hongjie Dai. Synthesis of individual single-walled carbon nanotubes on patterned silicon wafers. *Nature*, 395:878–881, Oct 1998.

[85] S. C. Lyu, B. C. Liu, S. H. Lee, C. Y. Park, H. K. Kang, C. W. Yang, and C. J. Lee. Large-scale synthesis of high-quality single-walled carbon nanotubes by catalytic decomposition of ethylene. *The Journal of Physical Chemistry B*, 108(5):1613–1616, 2004.

[86] A.M. Cassell, J.A. Raymakers, J. Kong, and H. Dai. Large scale CVD synthesis of single-walled carbon nanotubes. *The Journal of Physical Chemistry B*, 103(31):6484–6492, 1999.

[87] MS Kabir, R.E. Morjan, OA Nerushev, P. Lundgren, S. Bengtsson, P. Enokson, and E.E.B. Campbell. Plasma-enhanced chemical vapour deposition growth of carbon nanotubes on different metal underlayers. *Nanotechnology*, 16:458, 2005.

[88] Shaoming Huang, Mike Woodson, Richard Smalley, and Jie Liu. Growth mechanism of oriented long single walled carbon nanotubes using fast-heating chemical vapor deposition process. *Nano Letters*, 4(6):1025–1028, 2004.

[89] Huaping Liu, Guo-An Cheng, Ruiting Zheng, Yong Zhao, and Changlin Liang. Effects of the restructuring of Fe catalyst films on chemical vapor deposition of carbon nanotubes. *Surface and Coatings Technology*, 202(14):3157–3163, 2008.

[90] M. Cantoro, S. Hofmann, S. Pisana, C. Ducati, A. Parvez, A. C. Ferrari, and J. Robertson. Effects of pre-treatment and plasma enhancement on chemical vapor deposition of carbon nanotubes from ultra-thin catalyst films. *Diamond and Related Materials*, 15(4-8):1029–1035, 2006.

[91] A. A. Puretzky, D. B. Geohegan, S. Jesse, I. N. Ivanov, and G. Eres. In situ measurements and modeling of carbon nanotube array growth kinetics during chemical vapor deposition. *Applied Physics A: Materials Science & Processing*, 81:223–240, Jul 2005. 10.1007/s00339-005-3256-7.

[92] Anastasios John Hart and Alexander H. Slocum. Rapid growth and flow-mediated nucleation of millimeter-scale aligned carbon nanotube structures from a thin-film catalyst. *The Journal of Physical Chemistry B*, 110(16):8250–8257, 2006.

[93] R. F. Wood, S. Pannala, J. C. Wells, A. A. Puretzky, and D. B. Geohegan. Simple model of the interrelation between single- and multiwall carbon nanotube growth rates for the cvd process. *Physical Review B (Condensed Matter and Materials Physics)*, 75(23):235446, 2007.

[94] Jing Kong, Alan M. Cassell, and Hongjie Dai. Chemical vapor deposition of methane for single-walled carbon nanotubes. *Chemical Physics Letters*, 292(4-6):567–574, 1998.

[95] Gyula Eres, Anika A. Kinkhabwala, Hongtao Cui, David B. Geohegan, Alexandar A. Puretzky, and Douglas H. Lowndes. Molecular beam-controlled nucleation and growth of vertically aligned single-wall carbon nanotube arrays. *The Journal of Physical Chemistry B*, 109(35):16684–16694, 2005.

[96] Kenji Hata, Don N. Futaba, Kohei Mizuno, Tatsunori Namai, Motoo Yumura, and Sumio Iijima. Water-assisted highly efficient synthesis of impurity-free single-walled carbon nanotubes. *Science*, 306(5700):1362–1364, 2004.

[97] Shigeo Maruyama, Erik Einarsson, Yoichi Murakami, and Tadao Edamura. Growth process of vertically aligned single-walled carbon nanotubes. *Chemical Physics Letters*, 403(4-6):320–323, 2005.

[98] J.J. Jackson, A.A. Puretzky, K.L. More, C.M. Rouleau, G. Eres, and D.B. Geohegan. Pulsed growth of vertically aligned nanotube arrays with variable density. *ACS nano*, 2010.

[99] Zu-Po Yang, Lijie Ci, James A. Bur, Shawn-Yu Lin, and Pulickel M. Ajayan. Experimental observation of an extremely dark material made by a low-density nanotube array. *Nano Letters*, 8(2):446–451, 2008.

[100] E.R. Meshot, M. Bedewy, K.M. Lyons, A.R. Woll, K.A. Juggernauth, S. Tawfick, and A.J. Hart. Measuring the lengthening kinetics of aligned nanostructures by spatiotemporal correlation of height and orientation. *Nanoscale*, 2010.

[101] S. Dittmer, J. Ek-Weis, OA Nerushev, and EEB Campbell. Growth of aligned mwnt arrays using a micrometer scale local-heater at low ambient temperature. *Journal of Nanoscience and Nanotechnology*, 10(6):4015–4022, 2010.

[102] D.S. Engstrøm, N.L. Rupesinghe, K.B.K. Teo, W.I. Milne, and P. Bøgild. Vertically aligned CNT growth on a microfabricated silicon heater with integrated temperature control-determination of the activation energy from a continuous thermal gradient. *Journal of Micromechanics and Microengineering*, 21:015004, 2011.

[103] D.B. Geohegan, A.A. Puretzky, J.J. Jackson, C.M. Rouleau, G. Eres, and K.L. More. Flux-dependent growth kinetics and diameter selectivity in single-wall carbon nanotube arrays. *ACS nano*, 2011.

[104] K. Liu, K. Jiang, C. Feng, Z. Chen, and S. Fan. A growth mark method for studying growth mechanism of carbon nanotube arrays. *Carbon*, 43(14):2850–2856, 2005.

[105] K. Hasegawa and S. Noda. Moderating carbon supply and suppressing ostwald ripening of catalyst particles to produce 4.5-mm-tall single-walled carbon nanotube forests. *Carbon*, 2011.

[106] K. Bolton, F. Ding, and A. Rosén. Atomistic simulations of catalyzed carbon nanotube growth. *Journal of nanoscience and nanotechnology*, 6(5):1211–1224, 2006.

[107] M.A. Cullinan and M.L. Culpepper. Control of carbon nanotube geometry via tunable process parameters. *Applied Physics Letters*, 93:103106, 2008.

[108] C. Hedlund, H. O. Blom, and S. Berg. Microloading effect in reactive ion etching. *The 40th National Symposium of the American Vacuum Society*, 12(4):1962–1965, 1994.

[109] Eric W. Wong, Paul E. Sheehan, and Charles M. Lieber. Nanobeam Mechanics: Elasticity, Strength, and Toughness of Nanorods and Nanotubes. *Science*, 277(5334):1971–1975, 1997.

[110] Sander J. Tans, Alwin R. M. Verschueren, and Cees Dekker. Room-temperature transistor based on a single carbon nanotube. *Nature*, 393(6680):49–52, 1998.

[111] Thomas Rueckes, Kyoungha Kim, Ernesto Joselevich, Greg Y. Tseng, Chin-Li Cheung, and Charles M. Lieber. Carbon Nanotube-Based Nonvolatile Random Access Memory for Molecular Computing. *Science*, 289(5476):94–97, 2000.

[112] Anders Eriksson, SangWook Lee, Abdelrahim A. Sourab, Andreas Isacsson, Risto Kaunisto, Jari M. Kinaret, and Eleanor E. B. Campbell. Direct transmission detection of tunable mechanical resonance in an individual carbon nanofiber relay. *Nano Letters*, 8(4):1224–1228, 2008.

[113] D. Dragoman and M. Dragoman. Variable capacitance mechanisms in carbon nanotubes. *Journal of Applied Physics*, 101(3):036111, 2007.

[114] C. H. Ke, N. Pugno, B. Peng, and H. D. Espinosa. Experiments and modeling of carbon nanotube-based nems devices. *Journal of the Mechanics and Physics of Solids*, 53(6):1314–1333, 2005.

[115] JE Jang, SN Cha, Y. Choi, G.A.J. Amaratunga, DJ Kang, DG Hasko, JE Jung, and JM Kim. Nanoelectromechanical switches with vertically aligned carbon nanotubes. *Applied Physics Letters*, 87(16):163114–163114, 2005.

[116] J.E. Jang, S.N. Cha, Y.J. Choi, D.J. Kang, T.P. Butler, D.G. Hasko, J.E. Jung, J.M. Kim, and G.A.J. Amaratunga. Nanoscale memory cell based on a nanoelectromechanical switched capacitor. *Nature nanotechnology*, 3(1):26–30, 2007.

[117] Philip Kim and Charles M. Lieber. Nanotube Nanotweezers. *Science*, 286(5447):2148–2150, 1999.

[118] Aravind Vijayaraghavan, Sabine Blatt, Christoph Marquardt, Simone Dehm, Raghav Wahi, Frank Hennrich, and Ralph Krupke. Imaging electronic structure of carbon nanotubes by voltage-contrast scanning electron microscopy. *Nano Research*, 1(4):321–332, 2008.

[119] BG Demczyk, YM Wang, J. Cumings, M. Hetman, W. Han, A. Zettl, and RO Ritchie. Direct mechanical measurement of the tensile strength and elastic modulus of multiwalled carbon nanotubes. *Materials Science and Engineering: A*, 334(1):173–178, 2002.

[120] A. Cao, P.L. Dickrell, W.G. Sawyer, M.N. Ghasemi-Nejhad, and P.M. Ajayan. Super-compressible foamlike carbon nanotube films. *Science*, 310(5752):1307, 2005.

[121] A. Arun, H.L. Poche, T. Idda, D. Acquaviva, M.F.B. Badia, P. Pantigny, P. Salet, and A.M. Ionescu. Tunable mems capacitors using vertical carbon nanotube arrays grown on metal lines. *Nanotechnology*, 22:025203, 2011.

[122] A. Fasolino, JH Los, and MI Katsnelson. Intrinsic ripples in graphene. *Nature Materials*, 6(11):858–861, 2007.

[123] W. Bao, F. Miao, Z. Chen, H. Zhang, W. Jang, C. Dames, and C.N. Lau. Controlled ripple texturing of suspended graphene and ultrathin graphite membranes. *Nature nanotechnology*, 4(9):562–566, 2009.

[124] V. Singh, S. Sengupta, H.S. Solanki, R. Dhall, A. Allain, S. Dhara, P. Pant, and M.M. Deshmukh. Probing thermal expansion of graphene and modal dispersion at low-temperature using graphene nanoelectromechanical systems resonators. *Nanotechnology*, 21:165204, 2010.

[125] M. Poot and H.S.J. Van Der Zant. Nanomechanical properties of few-layer graphene membranes. *Applied Physics Letters*, 92(6):063111–063111, 2008.

[126] Q. Lu, M. Arroyo, and R. Huang. Elastic bending modulus of monolayer graphene. *Journal of Physics D: Applied Physics*, 42:102002, 2009.

[127] K.N. Kudin, G.E. Scuseria, and B.I. Yakobson. C_2F, BN, and C nanoshell elasticity from ab initio computations. *Physical Review B*, 64(23):235406, 2001.

[128] R. Nicklow, N. Wakabayashi, and HG Smith. Lattice dynamics of pyrolytic graphite. *Physical Review B*, 5(12):4951, 1972.

[129] KV Zakharchenko, JH Los, MI Katsnelson, and A. Fasolino. Atomistic simulations of structural and thermodynamic properties of bilayer graphene. *Physical Review B*, 81(23):235439, 2010.

[130] P. Koskinen and O.O. Kit. Approximate modeling of spherical membranes. *Physical Review B*, 82(23):235420, 2010.

[131] C.C. Chen, W. Bao, J. Theiss, C. Dames, C.N. Lau, and S.B. Cronin. Raman spectroscopy of ripple formation in suspended graphene. *Nano letters*, 9(12):4172–4176, 2009.

[132] S. Shivaraman, R.A. Barton, X. Yu, J. Alden, L. Herman, MVS Chandrashekhar, J. Park, P.L. McEuen, J.M. Parpia, H.G. Craighead, et al. Free-standing epitaxial graphene. *Nano letters*, 9(9):3100–3105, 2009.

[133] CL Wong, M. Annamalai, ZQ Wang, and M. Palaniapan. Characterization of nanomechanical graphene drum structures. *Journal of Micromechanics and Microengineering*, 20:115029, 2010.

[134] LM Malard, MA Pimenta, G. Dresselhaus, and MS Dresselhaus. Raman spectroscopy in graphene. *Physics Reports*, 473(5-6):51–87, 2009.

[135] N. Mounet and N. Marzari. First-principles determination of the structural, vibrational and thermodynamic properties of diamond, graphite, and derivatives. *Physical Review B*, 71(20):205214, 2005.

[136] H. Watanabe, N. Yamada, and M. Okaji. Linear thermal expansion coefficient of silicon from 293 to 1000 k. *International journal of thermophysics*, 25(1):221–236, 2004.

[137] P. Sutter, J.T. Sadowski, and E. Sutter. Graphene on Pt (111): Growth and substrate interaction. *Physical Review B*, 80(24):245411, 2009.

[138] E. Cerda and L. Mahadevan. Geometry and physics of wrinkling. *Physical review letters*, 90(7):74302, 2003.

[139] J. Moser, A. Barreiro, and A. Bachtold. Current-induced cleaning of graphene. *Applied Physics Letters*, 91(16):163513–163513, 2007.

[140] A. San Paulo and R. García. Tip-surface forces, amplitude, and energy dissipation in amplitude-modulation (tapping mode) force microscopy. *Physical Review B*, 64(19):193411, 2001.

[141] A.V. Pogorelov. *Bendings of surfaces and stability of shells*, volume 72. Amer Mathematical Society, 1988.

[142] Y. Zhang, Y. Wang, Z. Li, Y. Huang, and D. Li. Snap-through and pull-in instabilities of an arch-shaped beam under an electrostatic loading. *Microelectromechanical Systems, Journal of*, 16(3):684–693, 2007.

[143] S. Krylov and N. Dick. Dynamic stability of electrostatically actuated initially curved shallow micro beams. *Continuum Mechanics and Thermodynamics*, 22(6):445–468, 2010.

[144] D. Roodenburg, JW Spronck, HSJ Van der Zant, and WJ Venstra. Buckling beam micromechanical memory with on-chip readout. *Applied Physics Letters*, 94(18):183501–183501, 2009.

[145] N. Abele, R. Fritschi, K. Boucart, F. Casset, P. Ancey, and AM Ionescu. Suspended-gate mosfet: bringing new mems functionality into solid-state mos transistor. In *Electron Devices Meeting, 2005. IEDM Technical Digest. IEEE International*, pages 479–481. IEEE, 2005.

[146] Y.A. Tarakanov and J.M. Kinaret. A carbon nanotube field effect transistor with a suspended nanotube gate. *Nano letters*, 7(8):2291–2294, 2007.

[147] A. Reina, H. Son, L. Jiao, B. Fan, M.S. Dresselhaus, Z.F. Liu, and J. Kong. Transferring and identification of single-and few-layer graphene on arbitrary substrates. *The Journal of Physical Chemistry C*, 112(46):17741–17744, 2008.

[148] N. Peng, Q. Zhang, O.K. Tan, and N. Marzari. Study of gaseous interactions in carbon nanotube field-effect transistors through selective Si_3N_4 passivation. *Nanotechnology*, 19:465201, 2008.

[149] H.D. Espinosa and N. Pugno. Numerical analysis of nanotube based nems devices-part ii: Role of finite kinematics, stretching and charge concentrations. *Journal of applied mechanics*, 72(5):726–731, 2005.

[150] S. Li, Z. Yu, and P.J. Burke. Silicon nitride gate dielectric for top-gated carbon nanotube field effect transistors. *Journal of Vacuum Science & Technology B: Microelectronics and Nanometer Structures*, 22(6):3112–3114, 2004.